الجـــمـــهوريـــــة الجـــــزائريـــــة الـديمقـــراطيـــة الـشعبيـــــة
People's Democratic republic of Algeria
وزارة التـعـلـيـــم الـعـالـي و الـبحـث الـعـلـــمـي
Ministry of Higher Education and Scientific Research
جـــامـعـــــة عبد الحميـــد بن باديـــس – مستغانـــم
Abdelhamid Ibn Badis University – Mostaganem
كليـــــة الـعـلـــــوم و الـتكنولـــوجـــيـا
Faculty of Sciences and Technology
قسم هندسة الطرائق
Department of Process Engineering

N° ORDER:
D
.....
GP/2026

THESIS

Submitted for the

DOCTORATE DEGREE (Third Cycle)

In Process Engineering

Specialization: **Materials Process Engineering**

By:

LAHOUALI DIT YAHYAOUI AMINA

Structural And Electrochemical Study of a Heterocyclic Material

Defended on: **. . . /…../ 2026**

Before the jury composed of:

Mme. ATTOUTI Salima	President	Professor	University of Mostaganem
M. Boukabcha Nourdine	Examiner	Professor	University of Chlef
M. Megrouss Youcef	Examiner	Professor	University of Chlef
Mme. Boubegra Naima	Examiner	MCA	University of Mostaganem
M. Chouaih Abdelkader	Supervisor	Professor	University of Mostaganem
M. Saidj Merzouk	Co-supervisor	MCA	University of Mostaganem
M. Benderdouche Noureddine	Invited Professor	Professor	University of Mostaganem

ACADEMIC YEAR: 2025/2026

Acknowledgements

This thesis is the result of a long academic journey carried out with great motivation, dedication, and perseverance. I would first like to express my deepest gratitude to Almighty Allah for granting me the strength, health, and patience throughout the completion of this work.

This work was carried out at the Laboratory of Technology and Properties of Solids (LTPS), Department of Process Engineering, Faculty of Science and Technology, Abdelhamid Ibn Badis University of Mostaganem, under the supervision of Professor CHOUAIH Abdelkader, Dean of the Faculty of Science and Technology, and with the guidance of Mr. SAIDJ Merzouk, Associate Professor (Class A).

First of all, I would like to express my sincere and deepest gratitude to Professor CHOUAIH Abdelkader for the honor he bestowed upon me by accepting to supervise this thesis. I am particularly grateful for the trust he placed in me, for his valuable advice, availability, continuous support, and for all the scientific knowledge he enabled me to acquire throughout these years of research. His experience, scientific rigor, and human qualities have been a true source of inspiration for me.

I would also like to express my sincere thanks to Mr. SAIDJ Merzouk, Associate Professor (Class A) and co-supervisor of this thesis, for his precious help, availability, constant encouragement, and continuous guidance throughout this research work.

My profound gratitude goes to Professor ATTOUTI Salima for the honor of accepting to chair the jury of this thesis.

I would also like to warmly thank Professor BOUKABCHA Nourdine, Professor MEGROUSS Youcef, and Mrs. BOUBEGRA Naïma, Associate Professor (Class A), for accepting to examine this work and to be members of the thesis committee.

My sincere and deepest thanks are especially addressed to Professor BENDERDOUCHE Noureddine. I will forever remain grateful to him for the precious opportunity he offered me to pursue doctoral studies, without which this journey would never have been possible.

Beyond his immense scientific knowledge and outstanding academic experience, he has always shown great kindness, generosity, and invaluable support. His human qualities, professionalism, scientific rigor, and passion for research have been a true source of inspiration throughout my academic journey.

He will undoubtedly remain a role model in my professional and scientific career. Please accept my deepest gratitude and highest respect.

I am also grateful to our collaborators from the Laboratory of Materials Chemistry of Constantine, Faculty of Exact Sciences, Frères Mentouri Constantine 1 University, Constantine 25000, Algeria, for carrying out the electrochemistry part of the organic material on which this thesis is based.

Special thanks to all members of the LTPS laboratory, especially Dr. Nourhouda Belkafouf and Professor DJAFRI Ahmed, for their invaluable help and support during the preparation of this thesis.

I would also like to sincerely thank the entire team of the "Atomic and Molecular Physics" laboratory at the Department of Physics, Sakarya University – Turkey, especially Professor Yusuf ATALAY and Dr. Omer TAMER, for allowing me to complete two short-term training internships that contributed significantly to this thesis.

I would also like to express my sincere gratitude to Professor Marilena CARBONE and Professor Lorenzo GONTRANI from the University of Rome Tor Vergata for warmly welcoming me into their laboratory during my research internship.

Finally, I would like to express my deepest and most heartfelt gratitude to my parents and my brothers, to whom I owe so much. Their unwavering support has been a fundamental pillar throughout my academic journey. Their constant encouragement, patience, sacrifices, and unconditional love gave me the strength to persevere during difficult times and to celebrate every achievement. May Allah bless them abundantly with good health, a long life, and all the happiness they truly deserve. Thank you from the bottom of my heart for everything you have done and continue to do for me. I will forever remain deeply grateful to you.

In the name of Allah,

the Most Gracious, the Most Merciful.

All praise and thanks are due to Allah for granting me the strength, patience, knowledge, and perseverance to complete this thesis. Without His mercy and guidance, this achievement would not have been possible.

I dedicate this work with deep love and gratitude to my beloved parents, ***Aissa*** and ***Kheira***, whose endless sacrifices, sincere prayers, unconditional love, and constant support have illuminated my path throughout my life. May Allah bless them, protect them, and reward them with the highest levels of Jannah for everything they have done for me.

To my dear brothers, ***Mohamed and Abdelkader***, thank you for your encouragement, support, and kindness during every stage of this journey. May Allah keep us united in love and faith.

To my precious friends: ***Fatima, Wafa, Khadidja, Aya, Lakhder, Ali, Khayra, Latifa***, and ***Assia***, thank you for your sincere friendship, support, and the beautiful moments we shared. May Allah bless you all and grant you success and happiness in this life and the Hereafter.

A special prayer and dedication go to my beloved grandfather, grant him ***Al-Firdaws Al-A'la***. Though he is no longer with us, his memory and prayers remain forever in my heart.

Finally, I dedicate this humble work to everyone who supported me directly or indirectly. May Allah reward you all abundantly.

Alhamdulillah for everything.



Table Of Contents



Table of Contents

	Nomenclature	**i**
	List of Figures	**iii**
	List of Tables	**iv**
	General Introduction	**1**
	Chapter I: Fundamentals of Schiff Bases and Their Technological Applications	
I.1	Introduction	6
I.2	Schiff's base definition	6
I.3	General structure of a Schiff base	7
I.4	Classification of Schiff base ligands	8
I.4.1	Monodentate Schiff base	8
I.4.2	Bidentate Schiff base	9
I.4.3	Tridentate Schiff base	9
I.4.4	Tetradentate Schiff base	10
I.5	Different synthetic basic Schiff complexes	11
I.6	Structural and Electronic Characteristics	12
I.6.1	Azomethine Group (–C=N–)	12
I.6.2	π-Conjugation and Charge Transfer	12
I.7	Biological Applications of Schiff Bases	12
I.7.1	Antibacterial and Antifungal Activities	13
I.7.2	Antioxidant and Anticancer Activities	13
I.7.3	Schiff Bases and Metal Complexes in Biological Systems	13
I.8	Nonlinear Optical (NLO) Properties	14
I.8.1	Fundamental Concepts of NLO Properties	14
I.8.2	Structure–Property Relationship in NLO Behavior	14
I.8.3	Schiff Bases as Promising NLO Materials	15
I.9	Applications of Heterocyclic Materials in Photovoltaics	15
I.9.1	Principles of Organic Photovoltaic (OPV) Devices	15
I.9.2	Role of Heterocyclic Donors and Acceptors	16
I.9.3	Heterocyclic Hydrazone Schiff Base Systems as Organic Sensitizers for DSSCs	16
I.9.4	Electrochemical Gap and Photovoltaic Efficiency	17
I.9.5	Recent Advances in Photovoltaic Materials	17

I.10	Conclusion	18
Bibliographical references		18

Chapter II: Structural Analysis and Multipolar Electron Density Investigation

II.2	Introduction	21
II.3	X-ray diffraction	21
II.3.1	Principle of experimentation	22
II.3.2	X-ray production	22
II.3.3	X-ray-matter interaction	23
II.3.3.1	Diffraction and wave propagation	23
II.3.3.2	Elastic and inelastic scattering	25
II.3.3.3	Atomic diffusion factor	25
II.3.3.4	Structure factor	26
II.3.3.5	Inelastic scattering and absorption	27
II.4	Intensity correction	28
II.4.1	Absorption effects and geometric correction	28
II.4.2	Absorption correction	28
II.4.3	Lorentz and polarization factors	29
II.4.3.1	Lorentz factor	29
II.4.3.2	Polarization correction	29
II.4.3.3	Debye–Waller factor	30
II.5	Single crystal XRD	30
II.5.1	Principle of monocrystal XRD	30
II.5.2	Crystal parameters and systems	31
II.5.3	Miller indices and interplanar distance	31
II.6	Data recording and processing	31
II.6.1	Reciprocal space representation	31
II.6.2	Integration of intensities	32
II.6.3	Phase problem	32
II.6.3.1	Patterson method	33
II.6.3.2	Direct methods	33
II.6.3.3	Anomalous diffraction	33
II.6.4	Fourier synthesis	33
II.7	Structure refinement	34

II.7.1	Least squares refinement	34
II.7.2	Reliability factors	34
II.7.3	Multipolar refinement	35
II.7.3.1	Independent Atom Model	35
II.7.3.2	Difference Fourier method	36
II.7.3.3	Hansen–Coppens model	36
II.7.3.4	MoPro software strategy	37
II.7.3.5	Topological properties	38
II.7.3.6	Electron density gradient	38
II.7.3.7	Critical points	39
II.7.3.8	Laplacian of electron density	40
II.7.3.9	Bond ellipticity	40
II.7.3.10	Energy density at BCP	41
II.8	Conclusion	42
Bibliographical references		42

Chapter III: Quantum Chemical Methods and DFT Approaches in Molecular Modeling

III.1	Introduction	44
III.2	Quantum mechanics foundations	44
III.2.1	Wave function	46
III.2.2	Hamiltonian formulation	46
III.3	Schrödinger equation	47
III.4	Born–Oppenheimer approximation	48
III.5	Hartree–Fock method	49
III.5.1	Orbital approximation	49
III.5.2	Slater determinants	50
III.5.3	LCAO approximation	50
III.5.4	Roothaan formulation	51
III.5.5	Beyond Hartree–Fock	52
III.6	Density Functional Theory	52
III.6.1	LDA	54
III.6.2	GGA	55
III.6.3	Hybrid functions	55
III.7	Basis functions	56

III.7.1	Quantum chemistry functions	56
III.7.1.1	STO	56
III.7.1.2	GTO	57
III.7.1.3	Split-valence functions	58
Bibliographical references		60

Chapter IV: Structural, Electron Density and Quantum Chemical Investigations of FHP

IV.1	Introduction	62
IV.2	Structural characterization and electron density analysis	63
IV.2.1	Synthesis and structure of FHP	63
IV.2.2	Geometry optimization	66
IV.2.3	Electron density and AIM analysis	69
IV.2.3.1	Experimental electron density	70
IV.2.4	QTAIM bonding interactions	72
IV.3	Electronic and intermolecular properties	76
IV.3.1	Frontier orbitals and reactivity	76
IV.3.2	MEP and Hirshfeld surface	77
IV.3.2.1	Molecular electrostatic potential	78
IV.3.2.2	Fingerprint plots	79
IV.3.3	RDG and NCI analysis	82
IV.3.4	ELF and LOL analysis	84
Bibliographic references		88

Chapter V: Nonlinear Optical (NLO) Properties

V.1	Introduction	92
V.2	Fundamentals of nonlinear optics	93
V.2.1	Electromagnetism in materials	93
V.2.2	Polarization	93
V.2.3	Emission processes	93
V.2.4	Linear vs nonlinear optics	94
V.3	Basics of NLO	94
V.3.1	Light sources and lasers	94
V.3.2	NLO materials properties	94
V.4	Methodology	95

V.5	Results and discussion	96
V.5.1	Molecular structure	96
V.5.2	NLO properties	97
V.5.3	Static NLO	97
V.5.4	Dynamic NLO	98
V.5.5	Anisotropy	99
V.6	Conclusion	100
Bibliographic references		100

Chapter VI: Electrochemical Methods and Photovoltaic Application

VI.1	Introduction	102
VI.2	Electrochemical analysis	103
VI.3	Cyclic voltammetry	104
VI.4	HOMO–LUMO determination	106
VI.5	Electrochemical behavior	107
VI.6	Photovoltaic properties	107
VI.7	PV parameter calculation	108
VI.8	Voc, FF, PCE evaluation	109
VI.9	Donor-dependent performance	110
VI.10	Energy level analysis	111
VI.11	Conclusion	113
Bibliographic references		113
General Introduction		116

Nomenclature

Nomenclature

The following table lists all abbreviations, acronyms, and symbols used throughout this thesis, organised alphabetically. The final column indicates the chapter(s) in which each term appears. "Gen." refers to the General Introduction and General Conclusion.

Abbreviation	Full Term	Chapter(s)
C=N	Carbon–Nitrogen double bond (azomethine bond)	I
D–π–A	Donor–π–Acceptor molecular architecture	I, V, Gen.
DNA	Deoxyribonucleic acid	I
DSSC	Dye-Sensitized Solar Cell	I, Gen.
FT-IR	Fourier-Transform Infrared Spectroscopy	I, IV
HOMO	Highest Occupied Molecular Orbital	I, IV, V, VI, Gen.
ICT	Intramolecular Charge Transfer	I, IV, V, VI, Gen.
LUMO	Lowest Unoccupied Molecular Orbital	I, IV, V, VI, Gen.
NLO	Nonlinear Optical	I, V, Gen.
NMR	Nuclear Magnetic Resonance	I, IV
OPV	Organic Photovoltaic	I, VI, Gen.
PCE	Power Conversion Efficiency	I, VI, Gen.
SHG	Second Harmonic Generation	I, V
TiO_2	Titanium dioxide (semiconductor photoanode)	I
UV-Vis	Ultraviolet–Visible Spectroscopy	I
ZnO	Zinc oxide (semiconductor photoanode)	I
BCP	Bond Critical Point	II, IV, Gen.
CCP	Cage Critical Point	II
DRX	Diffraction des Rayons X (French for X-ray Diffraction)	II
IAM	Independent Atom Model	II, IV
MoPro	Molecular Properties software (multipolar refinement)	II, IV, Gen.
NCP	Nuclear Critical Point	II
QTAIM	Quantum Theory of Atoms in Molecules	II, IV, Gen.
RCP	Ring Critical Point	II
SHELX	Crystal Structure Refinement Software (G.M. Sheldrick)	II
XRD	X-ray Diffraction	II, IV, Gen.
B3LYP	Becke, 3-Parameter, Lee–Yang–Parr hybrid functional	III, IV, V, VI, Gen.
DFT	Density Functional Theory	III, IV, V, VI, Gen.
GGA	Generalized Gradient Approximation	III
GTO	Gaussian-Type Orbital	III
HF	Hartree–Fock method	III
LCAO	Linear Combination of Atomic Orbitals	III
LDA	Local Density Approximation	III
LYP	Lee–Yang–Parr (correlation functional)	III
PW91	Perdew–Wang 1991 correlation functional	III
SCF	Self-Consistent Field	III
STO	Slater-Type Orbital	III
STO-3G	Slater-Type Orbital – 3 Gaussians basis set	III
VWN	Vosko–Wilk–Nusair correlation functional	III
AIM	Atoms in Molecules	IV, Gen.
CCDC	Cambridge Crystallographic Data Centre	IV
DMSO	Dimethyl Sulfoxide (solvent)	IV, V, Gen.
EA	Electron Affinity	IV, VI
ED	Electron Density	II, IV
ELF	Electron Localization Function	IV, Gen.
FHP	(E)-3-(1-(2-(9H-Fluoren-9-ylidene)hydrazineyl)ethylidene)-6-methyl-2H-pyran-2,4(3H)-dione	IV, V, VI, Gen.
FMO	Frontier Molecular Orbitals	IV, Gen.
GCRD	Global Chemical Reactivity Descriptors	IV

HSA	Hirshfeld Surface Analysis	IV, Gen.
IP	Ionization Potential	IV, VI
LOL	Localized Orbital Locator	IV, Gen.
MEP	Molecular Electrostatic Potential	IV, Gen.
$P2_1/c$	Monoclinic space group (crystallographic notation)	IV
PCM	Polarizable Continuum Model	IV, Gen.
RDG	Reduced Density Gradient	IV, Gen.
VMD	Visual Molecular Dynamics (visualization software)	IV
PNA	Para-Nitroaniline (NLO reference/benchmark compound)	V, Gen.
α	Linear polarizability	V, Gen.
β	First-order hyperpolarizability	V, Gen.
γ	Second-order hyperpolarizability	V, Gen.
μ	Dipole moment	V, Gen.
Δα	Anisotropy of polarizability	V
CV	Cyclic Voltammetry	VI
ECT	Charge Transfer Energy (photovoltaic parameter)	VI
ELL	Energy Level Lineup (photovoltaic parameter)	VI
FF	Fill Factor	VI, Gen.
IP	Ionization Potential	IV, VI
Jsc	Short-circuit current density	VI
MeCN	Acetonitrile (solvent; CH_3CN)	VI
SCE	Saturated Calomel Electrode	VI, Gen.
Voc	Open-Circuit Voltage	VI, Gen.
η	Chemical hardness	VI
χ	Electronegativity	VI
ω	Electrophilicity index	VI
TD-DFT	Time-Dependent Density Functional Theory (future work)	Perspectives

List of Figures

Table of Contents

Chapter I: Fundamentals of Schiff Bases and Their Technological Applications

Figure I.1.	General structure of a Schiff base.	7
Figure I.2.	Reaction forming a Schiff base.	8
Figure I.3.	Monodentate Schiff base.	8
Figure I.4.	NN bidentate Schiff base donors.	9
Figure I.5.	NO donor bidentate Schiff base.	9
Figure I.6.	Tridentate Schiff base (ONO donors).	9
Figure I.7.	Tridentate Schiff base.	10
Figure I.8.	Tetradentate Schiff base (NNOO donors).	10
Figure I.9.	Tetradentate Schiff base (NNNO donors).	10
Figure I.10.	Different synthetic Schiff base complexes.	11

Chapter II: Structural Analysis and Multipolar Electron Density Investigation

Figure II.1.	X-ray production.	23
Figure II.2.	Diffraction of X-rays – Bragg's law.	24
Figure II.3.	The diffusion factor as a function of $(\sin \theta)/\lambda$.	26
Figure II.4.	Structure factor as a function of atomic diffusion factors.	27

Chapter IV: Structural, Electron Density and Quantum Chemical Investigations of FHP

Figure IV.1.	Synthesis of pyran-2,4-dione derivative.	64
Figure IV.2.	Space group presentation $P2_1/c$ of the monoclinic system.	65
Figure IV.3.	Molecular structure of FHP.	67
Figure IV.4.	Perspective view of the crystal packing for FHP.	67
Figure IV.5.	Electron density maps for FHP, (a) 2D-ED with a contour of 0.05 $e \cdot Å^{-3}$, and (b) 3D-ED.	72
Figure IV.6.	Variation of the molecule's energy gap at B3LYP/6-311G(d,p) with solvent.	79
Figure IV.7.	Molecular electrostatic potential (MEP) map of FHP.	80
Figure IV.8.	Hirshfeld surface maps of FHP: dnorm, de, di, shape index and curvedness.	82
Figure IV.9.	Two-dimensional fingerprint plots of FHP and their decomposed contact contributions.	84
Figure IV.10.	The scatter diagram and gradient isosurfaces of FHP.	86
Figure IV.11.	ELF, color-filled and contour map of the title compound.	88
Figure IV.12.	LOL color-filled and contour maps for the title compound.	89

Chapter VI: Electrochemical Methods and Photovoltaic Application

Figure VI.1	CV recorded in MeCN/0.1 M Bu_4NPF_6 for oxidation (top) and reduction (bottom) [12.5×10^{-4} M], sweep rate: 100 mV/s, working electrode: platinum disk, diameter 1 mm.	104
Figure VI.2	HOMO and LUMO of FHP and with different donors.	112
Figure VI.3	HOMO and LUMO of FHP and anthracene.	112



List of Tables



Table of Tables

Table II.1	Classification of critical points in QTAIM analysis	39
Table II.2	Topological criteria for interaction types	41
Table IV.1	Crystal structure refinement details of the synthesized compound.	65
Table IV.2	Selected DFT/XRD bond angles and bond lengths.	68
Table IV.3	Topological properties of the electron density of FHP.	73
Table IV.4	Topological parameters of intermolecular hydrogen-bond interactions	76
Table IV.5	HOMO-LUMO gap and GCRD calculated values of FHP by DFT/B3LYP.	79
Table V.1	The static/dynamic polarizability, anisotropy of polarizability, first-order hyperpolarizability, and second-order hyperpolarizability for FHP obtained by B3LYP/6-311G(d.p) level of theory.	99
Table VI.1	Calculated values of open circuit voltage (V_{oc}), Fill Factor (FF) and Energy Conversion Efficiency (PCE) for the studied molecule, with various donors.	112



General Introduction

The design and investigation of organic functional materials with extended π-conjugated frameworks has become a central theme in contemporary materials chemistry. Among the wide diversity of organic scaffolds explored in this field, Schiff bases and their hydrazone analogues occupy a privileged position owing to their ease of synthesis, remarkable structural tunability, and rich physicochemical versatility [1-2]. First described by Hugo Schiff in 1864, these azomethine-containing compounds are formed by the condensation of primary amines with carbonyl compounds, producing a characteristic -C=N- linkage that serves as the electronic backbone of the entire molecular architecture [3].

The azomethine bridge, combined with extended aromatic and heteroaromatic ring systems, gives rise to efficient π-electron delocalization and intramolecular charge transfer (ICT) between electron-donor and electron-acceptor fragments. These electronic features are directly responsible for the remarkable biological, optical, and electrochemical properties documented for this class of compounds, and have motivated an exponentially growing body of research at the interface of organic synthesis, theoretical chemistry, crystallography, and device physics [4-6].

Among the broad landscape of organic optoelectronic materials, donor-π-acceptor (D-π-A) molecular architectures have attracted particular attention due to their strong nonlinear optical (NLO) responses, favorable frontier orbital alignment, and suitability for photovoltaic applications [7]. Heterocyclic Schiff base hydrazone derivatives, which combine a rigid conjugated framework with multiple heteroatoms, represent an especially promising subclass for these applications. The coexistence of tunable HOMO-LUMO energy levels, pronounced polarizability, and structural flexibility makes them attractive candidates for optoelectronic technologies such as nonlinear optical devices, dye-sensitized solar cells (DSSCs), and organic photovoltaics (OPVs) [8-9].

The compound at the center of this thesis, (E)-3-(1-(2-(9H-fluoren-9-ylidene)hydrazineyl)ethylidene)-6-methyl-2H-pyran-2,4(3H)-dione (hereafter FHP), is a zwitterionic hydrazone Schiff base that embodies all of these structural and electronic attributes. Its molecular framework integrates an electron-rich fluorenyl moiety connected through a hydrazone bridge to an electron-withdrawing pyran-dione fragment, creating a well-defined D-π-A architecture. This combination promotes efficient intramolecular charge transfer, strong π-conjugation, and the stabilization of a zwitterionic keto-hydrazone form via intramolecular N-H···O hydrogen bonding, features that make FHP particularly suited to a multidisciplinary

investigation encompassing crystallography, quantum chemistry, nonlinear optics, and photovoltaics.

The principal objective of this thesis is to establish a rigorous and comprehensive structure-property relationship for the hydrazone Schiff base derivative FHP through the synergistic combination of advanced experimental techniques and state-of-the-art computational methods. Specifically, the work pursues the following interconnected goals:

- To synthesize FHP and determine its crystal structure by single-crystal X-ray diffraction at high resolution, and to characterize the experimental electron density distribution by multipolar refinement based on the Hansen-Coppens formalism.
- To apply the Quantum Theory of Atoms in Molecules (QTAIM) to characterize all covalent bonds, polar interactions, and non-covalent contacts present in the crystalline state, providing a physically rigorous description of chemical bonding at the electron density level.
- To investigate the electronic structure, frontier molecular orbitals, molecular electrostatic potential, non-covalent interaction landscape, electron localization function, and global reactivity descriptors of FHP by means of density functional theory (DFT) calculations at the B3LYP/6-311G(d,p) level.
- To evaluate the static and dynamic nonlinear optical (NLO) properties of FHP, including dipole moment, linear polarizability, first-order hyperpolarizability (β), and second-order hyperpolarizability (γ), in both gas-phase and solvated conditions, and to benchmark these against established NLO chromophores.
- To characterize the electrochemical behavior of FHP by cyclic voltammetry and to experimentally determine the HOMO and LUMO energy levels, which are then correlated with theoretical DFT values to assess the reliability of the computational approach.
- To evaluate the photovoltaic potential of FHP as an acceptor material in organic solar-cell architectures by calculating open-circuit voltage (Voc), fill factor (FF), and power conversion efficiency (PCE) for donor/FHP interfaces involving anthracene, tetracene, and pentacene.

The thesis is organized into six chapters, each addressing a distinct but interrelated aspect of the investigation of FHP:

Chapter I provides a comprehensive literature review covering the definition, classification, and synthesis of Schiff bases and hydrazone derivatives, their structural and electronic characteristics, biological activities, and documented roles in NLO and photovoltaic applications. This chapter establishes the theoretical framework and scientific motivation underlying the experimental and computational work presented in the subsequent chapters **[10-12]**.

Chapter II describes the experimental and theoretical techniques used for structural characterization. The principles of X-ray diffraction, data collection and processing, intensity correction procedures, and the mathematical formalism of multipolar refinement according to the Hansen-Coppens model are presented. The chapter also introduces the topological tools provided by QTAIM for analyzing electron density distributions, including bond critical points, Laplacian maps, ellipticity, and energy density descriptors **[13-15]**.

Chapter III presents the theoretical foundations of the quantum chemical methods employed in this work. The chapter covers the Schrödinger equation, the Born-Oppenheimer approximation, the Hartree-Fock method, and density functional theory (DFT), with particular attention to the B3LYP hybrid functional and the basis sets used in the calculations. The relevance of each approximation to the study of conjugated organic molecules is discussed **[16-18]**.

Chapter IV reports the structural characterization and quantum chemical investigation of FHP. The synthesis and crystal structure are described, followed by the experimental electron density analysis via multipolar refinement using MoPro and the QTAIM topological analysis of all bonding interactions. The chapter further presents the DFT-computed frontier molecular orbitals, global reactivity descriptors, molecular electrostatic potential, Hirshfeld surface analysis, reduced density gradient, electron localization function, and localized orbital locator **[19-21]**.

Chapter V is devoted to the nonlinear optical properties of FHP. Following an introduction to the fundamentals of nonlinear optics and the methodology employed, the static and dynamic NLO parameters—dipole moment, polarizability, first-order hyperpolarizability (β), and second-order hyperpolarizability (γ)—are reported for both gas-phase and DMSO-solvated conditions. The results are compared with benchmark values for established organic chromophores such as para-nitroaniline (PNA), confirming the promising NLO activity of FHP **[22-24]**.

Chapter VI examines the electrochemical properties and photovoltaic applications of FHP. Cyclic voltammetry measurements are used to determine the experimental HOMO and LUMO energy levels, which are compared with DFT-computed values. The photovoltaic performance of FHP as an acceptor is then evaluated theoretically by calculating Voc, FF, and PCE for interfaces with anthracene, tetracene, and pentacene donors. The obtained results confirm the potential of FHP for organic photovoltaic applications [25-27].

References

[1] Schiff, H. Mittheilungen aus dem Universitätslaboratorium in Pisa: Eine neue Reihe organischer Basen. Justus Liebigs Annalen der Chemie 1864, 131, 118-119.

[2] Dhar, D. N.; Taploo, C. L. Schiff bases and their applications. Journal of Scientific and Industrial Research 1982, 41, 501-506.

[3] Patai, S. The Chemistry of the Carbon-Nitrogen Double Bond; Wiley: London, 1970.

[4] Kumar, S.; Dhar, D. N.; Saxena, P. N. Applications of metal complexes of Schiff bases. Journal of Scientific & Industrial Research 2009, 68, 181-187.

[5] Cozzi, P. G. Metal-Schiff base complexes in catalysis: practical aspects. Chemical Society Reviews 2004, 33, 410-421. https://doi.org/10.1039/B307987H

[6] Keri, R. S.; Patil, S. A.; Budagumpi, S.; Nagaraja, B. M. Schiff base motifs in drug discovery. European Journal of Medicinal Chemistry 2015, 89, 207-251. https://doi.org/10.1016/j.ejmech.2014.10.027

[7] Kanis, D. R.; Ratner, M. A.; Marks, T. J. Design and construction of molecular assemblies with large second-order optical nonlinearities. Chemical Reviews 1994, 94, 195-242. https://doi.org/10.1021/cr00025a007

[8] Hagfeldt, A.; Boschloo, G.; Sun, L.; Kloo, L.; Pettersson, H. Dye-sensitized solar cells. Chemical Reviews 2010, 110, 6595-6663. https://doi.org/10.1021/cr900356p

[9] O'Regan, B.; Grätzel, M. A low-cost, high-efficiency solar cell based on dye-sensitized colloidal TiO_2 films. Nature 1991, 353, 737-740. https://doi.org/10.1038/353737a0

[10] Boyd, R. W. Nonlinear Optics, 3rd ed.; Academic Press: New York, 2008. ISBN 978-0-12-369470-6.

[11] Prasad, P. N.; Williams, D. J. Introduction to Nonlinear Optical Effects in Molecules and Polymers; Wiley: New York, 1991. ISBN 978-0-471-51562-2.

[12] Beaujuge, P. M.; Fréchet, J. M. J. Molecular design and ordering effects in π-functional materials for transistors and solar cells. Journal of the American Chemical Society 2011, 133, 20009-20029. https://doi.org/10.1021/ja2073643

[13] Bader, R. F. W. Atoms in Molecules: A Quantum Theory; Oxford University Press: Oxford, 1990. ISBN 978-0-19-855865-1.

[14] Espinosa, E.; Molins, E.; Lecomte, C. Hydrogen bond strengths revealed by topological analyses of experimentally observed electron densities. Chemical Physics Letters 1998, 285, 170-173. https://doi.org/10.1016/S0009-2614(98)00036-0

[15] Coppens, P. X-Ray Charge Densities and Chemical Bonding; Oxford University Press: New York, 1997. ISBN 978-0-19-509731-2.

[16] Hohenberg, P.; Kohn, W. Inhomogeneous electron gas. Physical Review 1964, 136, B864-B871. https://doi.org/10.1103/PhysRev.136.B864

[17] Kohn, W.; Sham, L. J. Self-consistent equations including exchange and correlation effects. Physical Review 1965, 140, A1133-A1138. https://doi.org/10.1103/PhysRev.140.A1133

[18] Becke, A. D. Density-functional thermochemistry. III. The role of exact exchange. Journal of Chemical Physics 1993, 98, 5648-5652. https://doi.org/10.1063/1.464913

[19] Guerraoui, A.; Djedouani, A.; Jeanneau, E.; Boumaza, A.; Alsalme, A.; Zarrouk, A.; Salih, K. S. M.; Warad, I. Crystal structure and spectroscopic study of (E)-3-(1-(2-(9H-fluoren-9-

ylidene)hydrazineyl)ethylidene)-6-methyl-2H-pyran-2,4(3H)-dione. Journal of Molecular Structure 2020, 1220, 128728. https://doi.org/10.1016/j.molstruc.2020.128728

[20] Hansen, N. K.; Coppens, P. Testing aspherical atom refinements on small-molecule data sets. Acta Crystallographica Section A 1978, 34, 909-921. https://doi.org/10.1107/S0567739478001886

[21] Datta, A.; Pati, S. K. Charge transfer in organic materials for nonlinear optics. Chemical Society Reviews 2006, 35, 1305-1323. https://doi.org/10.1039/B605478G

[22] Coe, B. J. Switchable nonlinear optical metallosystems. Chemical Reviews 2004, 104, 3577-3610. https://doi.org/10.1021/cr030039d

[23] Lahouali Dit Yahyaoui, A. et al. DFT-based investigation of structural, optoelectronic and molecular docking analysis of thiosemicarbazone derivatives. Next Materials 2026, 10, 101391. https://doi.org/10.1016/j.nxmate.2025.101391

[24] Yesodha, S. K.; Sadashiva Pillai, C. K.; Tsutsumi, N. Stable polymeric materials for nonlinear optics. Progress in Polymer Science 2004, 29, 45-74. https://doi.org/10.1016/j.progpolymsci.2003.08.006

[25] Bard, A. J.; Faulkner, L. R. Electrochemical Methods: Fundamentals and Applications, 2nd ed.; Wiley: New York, 2001. ISBN 978-0-471-04372-0.

[26] Scharber, M. C.; Mühlbacher, D.; Koppe, M.; Denk, P.; Waldauf, C.; Heeger, A. J.; Brabec, C. J. Design rules for donors in bulk-heterojunction solar cells. Advanced Materials 2006, 18, 789-794. https://doi.org/10.1002/adma.200501717

[27] Elgrishi, N.; Rountree, K. J.; McCarthy, B. D.; Rountree, E. S.; Eisenhart, T. T.; Dempsey, J. L. A practical beginner's guide to cyclic voltammetry. Journal of Chemical Education 2018, 95, 197-206. https://doi.org/10.1021/acs.jchemed.7b00361

CHAPITRE I

Fundamentals of Schiff Bases and Their Technological Applications

I.1 Introduction....6
I.2 Schiff's base definition....6
I.3 General structure of a Schiff base....7
I.4 Classification of Schiff base ligands....8
I.4.1 Monodentate Schiff base....8
I.4.2 Bidentate Schiff base....9
I.4.3 Tridentate Schiff base....9
I.4.4 Tetradentate Schiff base....10
I.5 Different synthetic basic Schiff complexes....11
I.6 Structural and Electronic Characteristics....12
I.6.1 Azomethine Group (–C=N–)....12
I.6.2 The π-Conjugation and Charge Transfer....12
I.7 Biological Applications of Schiff Bases....12
I.7.1 Antibacterial and Antifungal Activities....13
I.7.2 Antioxidant and Anticancer Activities....13
I.7.3 Schiff Bases and Metal Complexes in Biological Systems....13
I.8 Nonlinear Optical (NLO) Properties....14
I.8.1 Fundamental Concepts of NLO Properties....14
I.8.2 Structure–Property Relationship in NLO Behavior....14
I.8.3 Schiff Bases as Promising NLO Materials....15
I.9 Applications of Heterocyclic Materials in Photovoltaics....15
I.9.1 Principles of Organic Photovoltaic (OPV) Devices....15
I.9.2 Role of Heterocyclic Donors and Acceptors....16
I.9.3 Heterocyclic Hydrazone Schiff Base Systems as Organic Sensitizers for DSSCs....16
I.9.4 Electrochemical Gap and Photovoltaic Efficiency....17
I.9.5 Recent Advances in Heterocyclic Photovoltaic Materials....17
I.10 Conclusion....18
Bibliographical references....18

I.1 Introduction

The achievements of contemporary treatments stem from comprehensive research conducted in the areas of synthesis, analysis, and regulation of pharmaceutical products. Schiff bases, named after their developer Hugo Schiff, represent a significant class of organic compounds. The interest in these compounds is largely attributable to their straightforward preparation method, typically achieved in a single step, alongside their high yields. Additionally, Schiff bases exhibit remarkable thermal and photonic stability as well as considerable coordination capability, both in solution and in solid form. The physicochemical properties of these systems vary significantly, and they are utilized in multiple areas of chemistry, including catalysis, liquid-liquid extraction, and corrosion, where they function as inhibitors. The biological activity of Schiff bases has been the subject of extensive research in recent decades, with studies demonstrating their antibacterial, anti-inflammatory, antioxidant, and anticancer properties.

I.2 Schiff's base definition

A Schiff base is a compound formed through the condensation reaction of a primary amine with a ketone or aldehyde. This reaction results in the establishment of a carbon-nitrogen double bond (C=N), where the nitrogen atom is typically attached to an aryl (aromatic) or alkyl (aliphatic) group. In a broader context, Schiff bases can be represented by the general formula R1R2C=NR3, where R1 and R2 are organic groups that can vary in structure and size. The term "Schiff base" is often used interchangeably with "azomethine." However, some researchers restrict this definition to secondary aldimines, a subset of azomethines in which the imine carbon is connected to only one hydrogen atom. Thus, secondary aldimines typically conform to the general formula RCH=NR', where R and R' denote different organic groups **[1]**.

One notable characteristic of Schiff bases is the stability provided by the carbon chain attached to the nitrogen atom, which classifies them as a type of imine. When Schiff bases are derived specifically from aniline, where the nitrogen's substituent (R3) is a phenyl group or a phenyl group that has been substituted with other functional groups, these compounds are referred to as "anilines." The unique structural features of Schiff bases make them significant in various chemical reactions and applications, including their roles in organic synthesis and coordination chemistry **[2]**.

I.3 General structure of a Schiff base

A Schiff base is a type of organic compound that is formed from the reaction between an amine and a carbonyl compound, typically an aldehyde or a ketone. The general structure of a Schiff base features a central imine functional group, characterized by a nitrogen atom double-bonded to a carbon atom. This carbon atom is also bonded to a substituent, which can be a hydrogen atom or an alkyl or aryl group derived from the carbonyl compound. The overall molecular structure can vary widely depending on the specific reactants used, but the essential characteristic is the presence of the C=N bond. Schiff bases are notable for their role in various chemical and biological processes, as well as their applications in catalysis and material sciences.

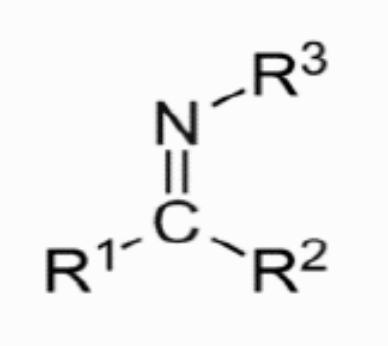


Figure I.1. General structure of a Schiff base.

I. 3. 1. Reaction mechanism of formation

The synthesis of Schiff bases is a notable chemical reaction often influenced by the presence of water molecules. This inclusion can result in a reversible reaction, known as hydrolysis, where the Schiff base can revert to its original components. Typically, this reaction is conducted in an alcoholic medium, which provides an appropriate environment for the reactants. In some instances, it may also take place under reflux conditions, where the mixture is heated to boiling and the vapors are condensed back into the reaction vessel, ensuring a sustained reaction temperature and promoting the formation of the desired products [3].

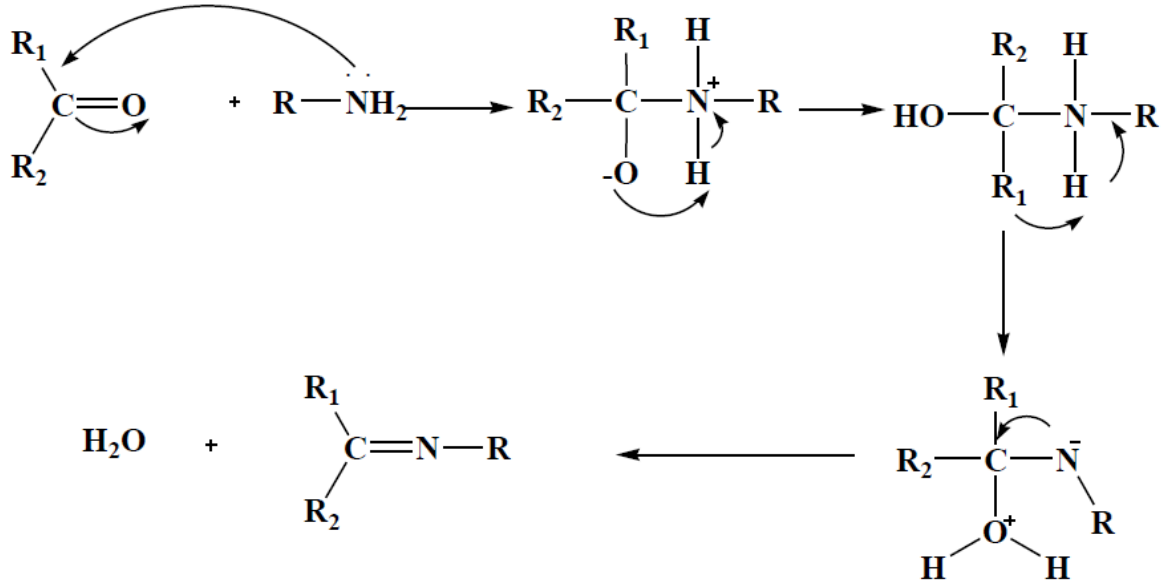


Figure I.2. Reaction forming a Schiff base.

I.4 Classification of Schiff base ligands

At the foundation of numerous coordination sites, ligands known as Schiff bases can be categorized based on a variety of structural types:

I.4.1 Monodentate Schiff base

In this context, we are discussing a molecule that features a single binding site for a metal atom. This molecule is capable of transferring a non-bonding electron pair, or doublet, to the central metal atom, thereby forming a bond. This principle can be demonstrated through the example of methylamine reacting with benzaldehyde, followed by a dehydration process. This reaction showcases the interaction between the molecule and the metal in a clear manner [4].

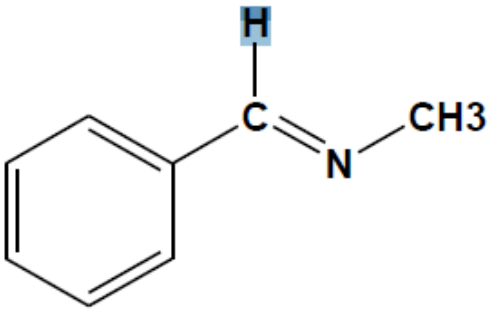


Figure I.3. Monodentate Schiff base.

I.4.2 Bidentate Schiff base

Schiff bases can exist in various structural forms, each exhibiting unique characteristics and properties.

a) Type NN donors:

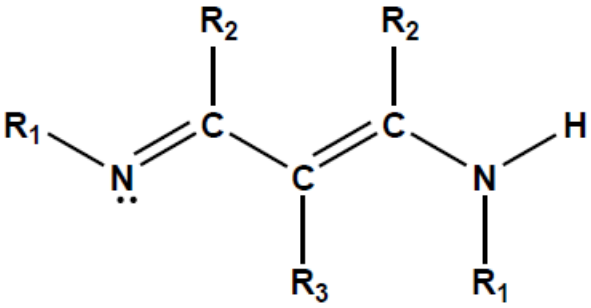


Figure I.4. NN bidentate Schiff base donors.

b) Type NO donors:

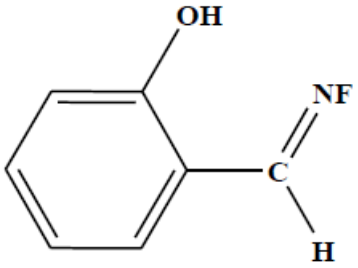


Figure I.5. NO donor bidentate Schiff base.

I.4.3 Tridentate Schiff base

The use of tridentate ligands in coordination chemistry is essential for stabilizing transition metals and donor elements. By coordinating through three donor atoms, these ligands form ring structures that enhance stability through the chelate effect, which reduces entropy during complexation. This stabilization prevents undesirable oxidation or reduction reactions and is valuable in applications such as catalysis, biological systems, and material science [5].

a) ONO donor type:

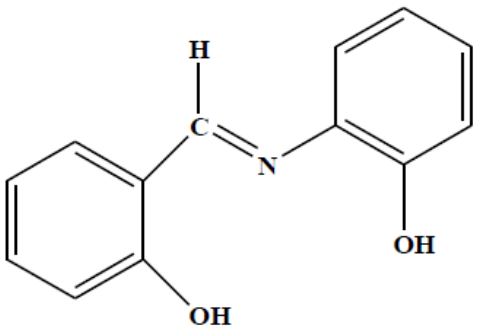


Figure I.6. Tridentate Schiff base (ONO donors)

b) NON-donor type:

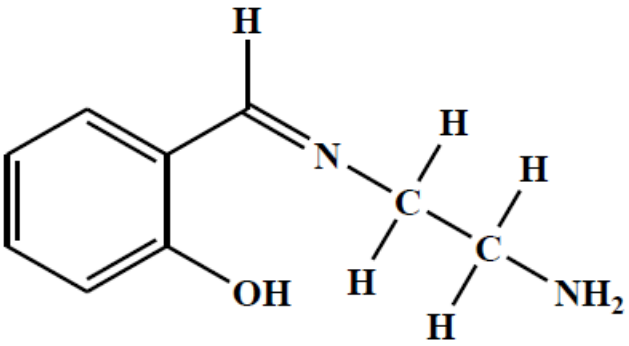


Figure I.7. Tridentate Schiff base

I.4.4 Tetradentate Schiff base

Tetradentate Schiff bases are extensively researched for the formation of metal complexes due to their strong chelating ability. The resulting complexes benefit from stabilization provided by the specific configurations of these ligands, making them highly effective in coordination chemistry [6].

a) Type NNOO donors:

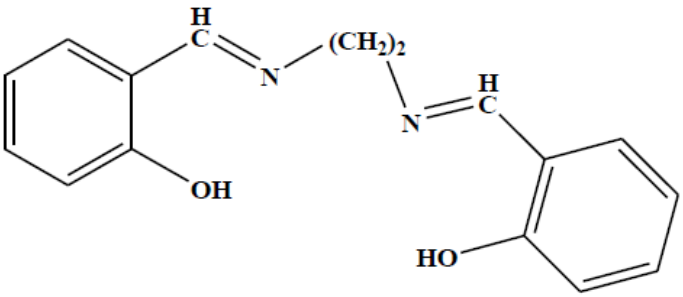


Figure I.8. Tetradentate Schiff base (NNOO donors)

b) Type NNNO donors:

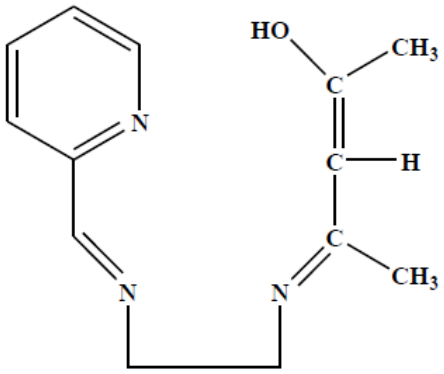


Figure I.9. Tetradentate Schiff base (NNNO donors)

I.5 Different synthetic basic Schiff complexes

Schiff bases are typically synthesized through a condensation reaction involving a primary amine and an aldehyde or ketone. This process results in the formation of an azomethine (–C=N–) functional group, accompanied by the elimination of a water molecule. The resulting ligands frequently feature additional donor sites, such as phenolic oxygen atoms, which significantly enhance their chelating capacity. The scheme presented illustrates that the Schiff base ligand initially exists in its neutral form (Y = H) and has the capacity to undergo deprotonation under specific conditions. The subsequent interaction with various metal precursors, including metal alkoxides [M(OR)n], metal amides [M(NR2)n], metal halides (MXn), or metal acetates [M(OAc)n], results in the formation of stable metal–Schiff base complexes. Coordination predominantly occurs through the azomethine nitrogen atoms and phenolate oxygen atoms, leading to the formation of chelated structures characterized by varying coordination numbers and geometries [7]. The introduction of substituents such as R, R1, and R2 (which may consist of alkyl or aryl groups) facilitates the precise modulation of both steric and electronic properties. Auxiliary ligands (denoted as X = OR, NR2, R, OAc, Cl, Br) serve to complete the coordination sphere surrounding the metal ion. This synthetic versatility allows for the development of an extensive array of Schiff base complexes with customized structural and electronic attributes, thereby rendering them suitable for investigations related to biological interactions and nonlinear optical (NLO) applications.

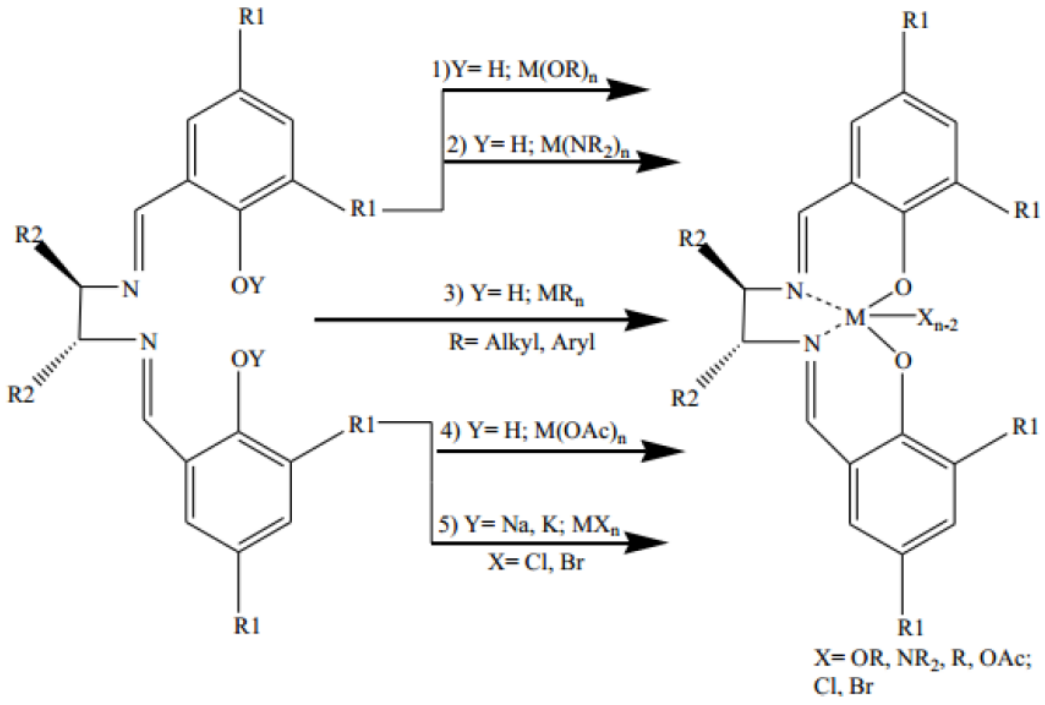


Figure I.10. Different synthetic Schiff base complexes

I.6 Structural and Electronic Characteristics

I.6.1 Azomethine Group (–C=N–)

The azomethine group (–C=N–) is a crucial structural element that characterizes Schiff bases and significantly influences their physicochemical properties. This functional group is created during the condensation reaction between a primary amine and either an aldehyde or a ketone, contributing to the rigidity and planar nature of the molecule. The nitrogen atom in the azomethine linkage holds a lone pair of electrons, allowing Schiff bases to serve as effective ligands by coordinating with metal ions, as well as engaging in hydrogen bonding and electrostatic interactions with biological macromolecules. As a result, the –C=N– group is vital in molecular docking studies, as it enhances the binding affinity to enzyme active sites or receptor cavities. Furthermore, the azomethine bond promotes electron delocalization throughout the molecular framework, which is key for optimizing electronic transitions and optical responses in Schiff base systems **[7–9]**.

I.6.2 The π-Conjugation and Charge Transfer

π-Conjugation is a key electronic feature of Schiff bases, especially those with aromatic or heterocyclic rings linked by the azomethine bridge. When π-conjugation is extended, it facilitates the efficient delocalization of electrons throughout the molecular framework, thereby promoting intramolecular charge transfer (ICT) between electron-donating and electron-accepting groups. This charge transfer mechanism plays an essential role in enhancing nonlinear optical (NLO) properties, such as polarizability and hyperpolarizability. Schiff bases designed with donor–π–acceptor (D–π–A) structures typically show smaller HOMO–LUMO energy gaps, elevated dipole moments, and improved optical responses. These electronic characteristics not only bolster strong NLO performance but also affect molecular reactivity and interactions within biological systems **[10–14]**.

I.7 Biological Applications of Schiff Bases

Schiff bases have garnered significant interest in the field of medicinal chemistry due to their diverse biological activities. The biological efficacy of these compounds is primarily attributed to the presence of the azomethine (–C=N–) functional group, the conjugated aromatic systems, and the potential for structural modification through various substituents. Recent experimental studies, complemented by molecular docking analyses, have elucidated the interaction mechanisms of Schiff bases with biological targets, thereby validating their prospective role as bioactive agents.

I.7.1 Antibacterial and Antifungal Activities

Numerous Schiff bases demonstrate significant antibacterial and antifungal activities against a wide array of Gram-positive and Gram-negative bacteria, as well as pathogenic fungi. The antimicrobial efficacy is frequently linked to the presence of the azomethine linkage, which has the capacity to disrupt microbial cell wall synthesis and modulate enzyme activity. Schiff bases are thought to penetrate microbial cell membranes more effectively due to their lipophilic characteristics, resulting in the disruption of essential cellular processes. Furthermore, molecular docking studies have indicated strong binding affinities of Schiff bases to key microbial enzymes, thereby corroborating their inhibitory potential. In various instances, the coordination of Schiff bases with metal ions has been shown to enhance their antimicrobial activity in comparison to the uncoordinated ligands **[15–16]**.

I.7.2 Antioxidant and Anticancer Activities

Schiff bases have been documented to exhibit significant antioxidant properties primarily attributed to their capability to scavenge free radicals and stabilize reactive oxygen species through the mechanism of electron delocalization. The incorporation of aromatic rings and electron-donating substituents enhances their efficiency in radical scavenging. Furthermore, various Schiff base derivatives have demonstrated promising anticancer activity by interacting with DNA, inhibiting specific enzyme systems, or inducing apoptosis in neoplastic cells. Molecular docking studies indicate that Schiff bases can bind effectively to cancer-related targets, including kinases and DNA-associated enzymes, thereby providing a theoretical foundation for their cytotoxic effects. These characteristics underscore the potential of Schiff bases as lead compounds in the design of anticancer therapeutics **[17–20]**.

I.7.3 Schiff Bases and Metal Complexes in Biological Systems

The biological activity of Schiff bases is often significantly enhanced upon coordination with metal ions. Schiff base metal complexes demonstrate improved stability, lipophilicity, and bioavailability, which contribute to more pronounced biological responses. Metal ions such as Cu(II), Ni(II), Zn(II), and Co(II) are integral to biological systems, and their complexes with Schiff bases exhibit effective interactions with biomolecules, including proteins and nucleic acids. These complexes frequently display superior antimicrobial, antioxidant, and anticancer activities compared to their uncoordinated counterparts. Docking studies further substantiate

the increased binding affinity of metal complexes toward biological targets, highlighting their significance in the fields of medicinal and bioinorganic chemistry [21–23].

I.8 Nonlinear Optical (NLO) Properties

Nonlinear optical (NLO) materials have garnered significant attention due to their critical role in contemporary photonics and optoelectronic technologies. Organic compounds, particularly Schiff bases, are regarded as promising candidates for NLO applications owing to their inherent structural flexibility, pronounced π-electron delocalization, and adjustable electronic properties. Furthermore, the presence of azomethine linkages and donor–acceptor substituents is instrumental in augmenting their nonlinear optical responses.

I.8.1 Fundamental Concepts of NLO Properties

Nonlinear optical properties emerge when the polarization of a molecule exhibits a nonlinear response to an applied electromagnetic field. Under conditions of low light intensity, the induced polarization is directly proportional to the electric field, reflecting linear optical behavior. Conversely, at elevated light intensities, the significance of higher-order terms increases, resulting in nonlinear effects. These phenomena are characterized by molecular parameters, including linear polarizability (α), first hyperpolarizability (β), and second hyperpolarizability (γ). The first hyperpolarizability is linked to second-order nonlinear optical (NLO) phenomena, such as second harmonic generation, whereas the second hyperpolarizability governs third-order processes, which encompass optical limiting and the Kerr effect. These parameters exhibit considerable sensitivity to the molecular structure, electronic distribution, and mechanisms of charge transfer [24–27].

I.8.2 Structure–Property Relationship in NLO Behavior

The nonlinear optical (NLO) response of a molecule is significantly influenced by its structural and electronic characteristics. Schiff bases that incorporate extended π-conjugation systems and donor–π–acceptor (D–π–A) architectures typically demonstrate enhanced NLO properties, which can be attributed to effective intramolecular charge transfer (ICT). The azomethine (–C=N–) group serves as a potent conjugation bridge, promoting electron delocalization between electron-donating and electron-withdrawing moieties. Several factors, including molecular planarity, conjugation length, substituent effects, and dipole moment, play a crucial role in determining the magnitude of hyperpolarizability values. A diminished HOMO–LUMO energy gap is frequently associated with more pronounced NLO responses,

rendering Schiff bases particularly advantageous for structure–property optimization through both theoretical and experimental methodologies [27–29].

I.8.3 Schiff Bases as Promising NLO Materials

Schiff bases are regarded as promising organic materials for nonlinear optics (NLO) due to their ease of synthesis, chemical stability, and structural tunability. Through the strategic modification of substituents and conjugation pathways, it is possible to systematically enhance their optical properties. Both experimental measurements and density functional theory (DFT) calculations have established that Schiff bases, along with their metal complexes, exhibit considerable second- and third-order NLO responses. Furthermore, the coordination with metal ions can enhance NLO performance through metal–ligand charge transfer and an increase in molecular polarizability. These attributes render Schiff bases particularly attractive candidates for applications in optical switching, frequency conversion, optical limiting, and other photonic devices [30–32].

I.9 Applications of Heterocyclic Materials in Photovoltaics

I.9.1 Principles of Organic Photovoltaic (OPV) Devices

Organic photovoltaic (OPV) devices are a class of solar cells that convert solar radiation into electrical energy through the photoactive behavior of organic semiconducting materials. In contrast to conventional inorganic silicon-based photovoltaics, OPVs utilize π-conjugated polymers or small organic molecules as electron donor and electron acceptor components, offering significant advantages such as lightweight structure, mechanical flexibility, low-temperature processing, and cost-effective large-area fabrication [33]. The operational principle of OPV devices is based on several sequential photophysical processes. Initially, incident photons are absorbed by the donor material, generating tightly bound electron–hole pairs known as excitons due to the low dielectric constant of organic semiconductors. These excitons then diffuse toward the donor/acceptor interface, where sufficient energetic offset between the highest occupied molecular orbital (HOMO) and the lowest unoccupied molecular orbital (LUMO) levels facilitates exciton dissociation into free charge carriers. Subsequently, electrons are transported through the acceptor phase while holes migrate through the donor phase toward their respective electrodes, resulting in current generation in the external circuit [34]. The efficiency of this process strongly depends on factors such as charge carrier mobility, nanoscale morphology of the active layer, interfacial engineering, and minimization of recombination losses. Among the various OPV architectures, bulk heterojunction structures have been widely

adopted because they provide an enlarged donor–acceptor interfacial area, thereby enhancing exciton separation and charge collection. Despite current limitations related to long-term stability and moderate power conversion efficiency compared with inorganic counterparts, OPV technology remains highly attractive for next-generation renewable energy applications due to its tunable optoelectronic properties and compatibility with flexible electronic systems [35].

I.9.2 Role of Heterocyclic Donors and Acceptors

The efficiency of organic photovoltaic materials is largely influenced by the donor and acceptor units present in their molecular structure. In this regard, heterocyclic Schiff base compounds have attracted considerable attention because of their extended π-conjugation, structural rigidity, and tunable electronic properties. The presence of heteroatoms such as nitrogen, sulfur, and oxygen within heterocyclic rings enhances electron delocalization and promotes intramolecular charge transfer [36]. In such systems, electron-rich heterocyclic fragments generally serve as donor moieties, whereas electron-deficient groups, particularly the azomethine (–CH=N–) linkage, can exhibit acceptor behavior by facilitating electron withdrawal. This donor–acceptor interaction improves light absorption, lowers the energy band gap, and enhances charge separation and transport [37]. Moreover, the Schiff base bridge serves as an effective conjugated pathway between the heterocyclic units, thereby modulating the HOMO and LUMO energy levels. Therefore, heterocyclic donor–acceptor molecules represent promising building blocks for the development of efficient organic photovoltaic materials due to their favorable optoelectronic characteristics and molecular adaptability.

I.9.3 Heterocyclic Hydrazone Schiff Base Systems as Organic Sensitizers for DSSCs

Hydrazone-based heterocyclic Schiff base molecules have attracted increasing attention in dye-sensitized solar cells (DSSCs) due to their favorable structural and electronic properties. These systems contain a conjugated hydrazone (–NH–N=CH–) linkage within a heterocyclic framework, which enhances π-electron delocalization and promotes efficient intramolecular charge transfer. The hydrazone Schiff base moiety acts as an extended conjugation bridge facilitating electron migration between electron-donating and electron-accepting units. This donor–π–acceptor architecture improves light harvesting efficiency and supports rapid charge separation, which is essential for effective electron injection into semiconductor materials such as TiO_2. Furthermore, the presence of multiple heteroatoms increases molecular polarity and provides potential anchoring sites for surface interaction, enhancing charge transport and adsorption stability. Consequently, heterocyclic hydrazone Schiff base molecules represent

promising candidates for the design of efficient and tunable organic sensitizers in DSSC applications [38–40].

I.9.4 Electrochemical Gap and Photovoltaic Efficiency

The electrochemical energy gap (E_{gap}), defined as the energy difference between the HOMO and LUMO levels, is a key parameter governing the photovoltaic performance of organic semiconductor materials. In heterocyclic Schiff base hydrazone molecules, extended π-conjugation and donor–acceptor interactions play an important role in tuning this gap by stabilizing frontier molecular orbitals. A reduced electrochemical gap generally enhances visible light absorption and facilitates efficient exciton generation under solar irradiation. Moreover, the relative alignment of HOMO and LUMO energy levels with respect to the redox potential of the electrolyte and the conduction band of wide-bandgap semiconductor photoanodes (such as TiO_2 or ZnO) is crucial for effective charge injection and dye regeneration. When the LUMO level is higher than the conduction band of the semiconductor, electron injection becomes energetically favorable, while an adequately low HOMO level ensures efficient regeneration by the electrolyte. Therefore, molecular design strategies aimed at tuning the electrochemical gap—through structural modification of heterocyclic systems and hydrazone linkages—are essential for optimizing light harvesting, minimizing recombination losses, and improving the overall power conversion efficiency of dye-sensitized solar cells [41–43].

I.9.5 Recent Advances in Heterocyclic Photovoltaic Materials

In recent years, heterocyclic compounds have emerged as a central class of materials in the development of high-performance photovoltaic devices due to their structural versatility, strong π-conjugation, and tunable electronic properties. Significant progress has been achieved in designing heterocyclic donor–acceptor systems incorporating moieties such as thiophene, pyridine, pyranone, and triazole, which allow fine control over the HOMO–LUMO energy levels and optical absorption properties [44]. In particular, heterocyclic Schiff base derivatives, including hydrazone-based systems, have gained increasing attention owing to their facile synthesis, structural adaptability, and efficient intramolecular charge transfer characteristics. These features contribute to enhanced light harvesting, improved charge separation, and reduced recombination losses in both dye-sensitized solar cells (DSSCs) and organic photovoltaic (OPV) devices [45]. Recent molecular engineering strategies focus on optimizing donor–π–acceptor architectures, extending conjugation length, and introducing electron-

withdrawing or electron-donating substituents to enhance photovoltaic performance. Additionally, advances in computational chemistry and density functional theory (DFT) studies have facilitated the prediction and rational design of heterocyclic materials with tailored optoelectronic properties [46]. As a result, heterocyclic photovoltaic materials are now considered promising candidates for next-generation, low-cost, and flexible solar energy technologies.

I.10 Conclusion

This chapter provides a comprehensive overview of Schiff bases, focusing on their structural features, biological significance, nonlinear optical (NLO) properties, and photovoltaic relevance. It highlights the importance of the azomethine (–CH=N–) group and extended π-conjugation in facilitating intramolecular charge transfer, molecular interactions, and electronic delocalization. In addition, the biological potential of Schiff bases is explored and supported by molecular docking studies, emphasizing their interaction with biological targets. The relationship between molecular structure and NLO behavior is also discussed, showing how electronic distribution and conjugation influence optical response. Furthermore, Schiff base systems are recognized as promising candidates in organic photovoltaic applications due to their tunable HOMO–LUMO energy levels, strong light absorption, and efficient donor–acceptor characteristics, which enhance charge separation and transport in solar energy conversion systems. This discussion provides a solid theoretical foundation for the subsequent investigation of molecular docking, nonlinear optical properties, and photovoltaic behavior of the studied Schiff base systems.

Bibliographical references

[1] S. Ali, N. Kasoju, A. Luthra, A. Singh, H. Sharanabasava, A. Sahu, U. Bora, *Food Res. Inter.,* **2008**, *41*, 1-15.
[2] T. Akiyama, M. Sanada, K. Fuchibe, *Synlett*, **2003**, *17*, 1463.
[3] V. Bankovitch, G. Carrier, C. Gagnon, L. Normandin, G. Kennedy, J. Zayed, *Sci. Total Environ.*, **2003**, 185-193.
[4] V. Barda, J. Varquez, F. Lopez, R. Santillan, N. Farfan, *J. Org. Metal. Chem.*, **2005**, *23*, 690.
[5] Y. Belokon, B. Green, N. Ikonikkov, M. North, T. Pansons, *Tetrahedron*, **2001**, *57*, 71-779.
[6] W. Bielinski, *Rev. Méd. Suisse*, **2006**, *2*, 74.
[7] K. Bouhadjra, *Mémoire de Magister*, Université Mouloud Mammeri, Tizi-Ouzou, Algérie, **2011**.
[8] Schiff, H. *Mittheilungen aus dem Universitätslaboratorium in Pisa: Eine neue Reihe organischer Basen*. **Justus Liebigs Annalen der Chemie**, 1864, **131**, 118–119.
[9] Patai, S. *The Chemistry of the Carbon–Nitrogen Double Bond*; Wiley: London, 1970.
[10] Dhar, D. N.; Taploo, C. L. *Schiff bases and their applications*. **Journal of Scientific and Industrial Research**, 1982, **41**, 501–506.
[11] Prasad, P. N.; Williams, D. J. *Introduction to Nonlinear Optical Effects in Molecules and Polymers*; Wiley: New York, 1991.

[12] Datta, A.; Pati, S. K. *Charge transfer and nonlinear optical properties*. **Chemical Society Reviews**, 2006, **35**, 1305–1323.
[13] Abdel-Kader, N. S.; El-Ansary, A. L. *Electronic structure and NLO properties of Schiff bases*. **Spectrochimica Acta Part A**, 2014, **118**, 1–7.
[14] Fukui, K. *Role of frontier orbitals in chemical reactions*. **Science**, 1982, **218**, 747–754.
[15] Dhar, D. N.; Taploo, C. L. *Schiff bases and their applications*. **Journal of Scientific and Industrial Research**, 1982, **41**, 501–506.
[16] Kumar, S.; Dhar, D. N.; Saxena, P. N. *Applications of metal complexes of Schiff bases*. **Journal of Scientific & Industrial Research**, 2009, **68**, 181–187.
[17] Singh, K.; Barwa, M. S.; Tyagi, P. *Synthesis and biological studies of Schiff base metal complexes*. **European Journal of Medicinal Chemistry**, 2006, **41**, 147–153.
[18] Chohan, Z. H.; Supuran, C. T. *Antioxidant and anticancer Schiff base compounds*. **Journal of Enzyme Inhibition and Medicinal Chemistry**, 2008, **23**, 240–251.
[19] Keri, R. S.; Patil, S. A.; Budagumpi, S.; Nagaraja, B. M. *Schiff base motifs in drug discovery*. **European Journal of Medicinal Chemistry**, 2015, **89**, 207–251.
[20] Abdel-Rahman, L. H.; et al. *Schiff bases as anticancer agents*. **Spectrochimica Acta Part A**, 2013, **111**, 266–276.
[21] Tweedy, B. G. *Plant extracts with metal chelates*. **Phytopathology**, 1964, **55**, 910–914.
[22] Cozzi, P. G. *Metal–Schiff base complexes in medicinal chemistry*. **Chemical Society Reviews**, 2004, **33**, 410–421.
[23] Prasad, P. N.; Williams, D. J. *Introduction to Nonlinear Optical Effects in Molecules and Polymers*; Wiley, 1991.
[24] Boyd, R. W. *Nonlinear Optics*; Academic Press: New York, 2008.
[25] Prasad, P. N.; Williams, D. J. *Introduction to Nonlinear Optical Effects in Molecules and Polymers*; Wiley: New York, 1991.
[26] Zyss, J. *Nonlinear Optical Properties of Organic Molecules and Crystals*; Academic Press, 1987.
[27] Datta, A.; Pati, S. K. *Charge transfer and nonlinear optical properties*. **Chemical Society Reviews**, 2006, **35**, 1305–1323.
[28] Kanis, D. R.; Ratner, M. A.; Marks, T. J. *Design and construction of molecular assemblies with large NLO responses*. **Chemical Reviews**, 1994, **94**, 195–242.
[29] Fukui, K. *Role of frontier orbitals in chemical reactions*. **Science**, 1982, **218**, 747–754.
[30] Coe, B. J. *Switchable nonlinear optical metallosystems*. **Chemical Reviews**, 2004, **104**, 3577–3610.
[31] Abdel-Kader, N. S.; et al. *DFT investigation of NLO properties of Schiff bases*. **Spectrochimica Acta Part A**, 2014, **118**, 1–7.
[32] Yesodha, S. K.; Sadashiva Pillai, C. K.; Tsutsumi, N. *Stable polymeric materials for nonlinear optics*. **Progress in Polymer Science**, 2004, **29**, 45–74.
[33] Arbouch, I., Karzazi, Y., & Hammouti, B. (2014). *Organic photovoltaic cells: Operating principles, recent developments and current challenges – Review*. Physical and Chemical News, 72, 73–84.
[34] Yu, J., Zheng, Y., & Huang, J. (2014). *Towards high performance organic photovoltaic cells: A review of recent development in organic photovoltaics*. Polymers, 6(9), 2473–2509.
[35] Mazzio, K. A., & Luscombe, C. K. (2015). *The future of organic photovoltaics*. Chemical Society Reviews, 44, 78–90
[36] Kumari, N., et al. (2014). *Review on Schiff bases and their metal complexes as organic photovoltaic materials*. Renewable and Sustainable Energy Reviews, 36, 220–227.
[37] Wan, X., et al. (2020). *Acceptor–donor–acceptor type molecules for high performance organic photovoltaics*. Chemical Society Reviews, 49, 2828–2842
[38] El-Ghamry, H. A., et al. (2016). Hydrazone Schiff base compounds: synthesis, characterization and applications in materials science. *Journal of Molecular Structure*, 1119, 1–10.
[39] Singh, K., et al. (2019). Hydrazone-based organic materials for optoelectronic applications. *Dyes and Pigments*, 162, 1–15.
[40] Roy, S., & Barik, A. K. (2021). Schiff base hydrazones: synthesis and photophysical applications. *Materials Chemistry Frontiers*, 5, 2345–2362.

[41] Hagfeldt, A., Boschloo, G., Sun, L., Kloo, L., & Pettersson, H. (2010). Dye-sensitized solar cells. *Chemical Reviews*, 110(11), 6595–6663.
[42] Yum, J. H., et al. (2012). Molecular engineering of organic sensitizers for dye-sensitized solar cells. *Energy & Environmental Science*, 5, 9942–9959.
[43] O'Regan, B., & Grätzel, M. (1991). A low-cost, high-efficiency solar cell based on dye-sensitized colloidal TiO_2 films. *Nature*, 353, 737–740.
[44] Li, G., Zhu, R., & Yang, Y. (2012). Polymer solar cells. *Nature Photonics*, 6, 153–161.
[45] Beaujuge, P. M., & Fréchet, J. M. J. (2011). Molecular design and ordering effects in π-functional materials for organic electronics. *Journal of the American Chemical Society*, 133, 20009–20029.
[46] Kundu, T., et al. (2020). Heterocyclic small molecules for organic solar cells: Recent advances and perspectives. *Materials Today Energy*, 18, 100509

CHAPTER II

Structural Analysis and Multipolar Electron Density Investigation

II.2 Introduction 21
II.3 X-ray diffraction 21
II.3.1 Principle of experimentation 22
II.3.2 X-ray production 22
II.3.3 X-ray-matter interaction 23
II.3.3.1 Analysis of Diffraction and Wave Propagation 23
II.3.3.2 Elastic and inelastic scattering 25
II.3.3.3 Atomic Diffusion Factor 25
II.3.3.4 Structure factor 26
II.3.3.5 Inelastic Scattering and Absorption 27
II.4 Intensity Correction 28
II.4.1 Absorption effects and geometric correction 28
II.4.2 Absorption correction 28
II.4.3 Correction for Lorentz and polarization factors 29
II.4.3.1 Lorentz factor 29
II.4.3.2 Polarization correction 29
II.4.3.3 Effect of temperature: the Debye-Waller factor 30
II.5 DRX of Single Crystals 30
II.5.1 Principle of monocrystal XRD 30
II.5.2 Crystal Parameters and Crystal Systems 31
II.5.3 Miller Indices and Interplanar Distance 31
II.6 II.5 Data Recording and Processing 31
II.6.1 Representation in Reciprocal Space 31
II.6.2 Methods for integrating intensities 32
II.6.3 Solving the Phase Problem 32
II.6.3.1 Patterson method 33

II.6.3.2 Direct Methods 33
II.6.3.3 Anomalous Diffraction 33
II.6.4 Fourier synthesis 33
II.7 Resolution and Structure Refinement 34
II.7.1 Refinement of crystal parameters using the least squares method 34
II.7.2 Reliability factors and convergence criteria 34
II.7.3 Multipolar Refinement 35
II.7.3.1 Independent Atom Model (IAM) 35
II.7.3.2 Difference Fourier Series Method 36
II.7.3.3 Multipolar Electron Density Model According to Hansen and Coppens 36
II.7.3.4 Refinement Strategy and Software (MoPro) 37
II.7.3.5 Derivation of Topological Properties from Multipolar Density 38
II.7.3.6 The Electron Density and Its Gradient Field 38
II.7.3.7 Critical Points: Definition and Classification 39
II.7.3.8 The Laplacian of the Electron Density 40
II.7.3.9 Bond Ellipticity and the π Character of Chemical Bonds 40
II.7.3.10 Energy Density Analysis at the Bond Critical Point 41
II.8 Conclusion 42
Bibliographical references 42

II.1 Introduction

In this chapter, we present an overview of the crystallographic and electron-density characterization of the synthesized materials using advanced X-ray diffraction techniques combined with multipolar refinement methods. Particular emphasis is placed on high-resolution X-ray diffraction analysis and experimental charge-density studies performed using the Hansen–Coppens multipolar formalism implemented in the MoPro Suite. These complementary approaches enable a detailed investigation of the molecular geometry, electron-density distribution, and intermolecular interactions within the crystalline structure, leading to a deeper understanding of the electronic and structural properties of the studied compounds. Single-crystal X-ray diffraction analysis provides accurate crystallographic parameters, including bond lengths, bond angles, atomic coordinates, and crystal symmetry, allowing precise determination of the three-dimensional arrangement of atoms within the crystal lattice. Beyond the conventional Independent Atom Model (IAM), multipolar refinement offers a more realistic description of the aspherical electron density around atoms by modeling deformation density contributions according to the Hansen–Coppens Multipole Model. This method enables the derivation of detailed topological properties of the electron density within the framework of Quantum Theory of Atoms in Molecules (QTAIM), providing valuable information about chemical bonding, charge transfer, electron delocalization, and weak intermolecular interactions in crystalline materials.

II.2 X-ray diffraction

X-ray diffraction is a highly effective technique for investigating molecular structures. Its development has established it as a leading method for structural determination in the field of chemistry. This technique can be applied to a variety of substances, including organic, inorganic, and organometallic compounds, as well as biological macromolecules such as proteins. In this technique, an X-ray beam is directed toward the sample, where it interacts with the electron density of the material, resulting in a diffraction pattern that reveals the internal atomic arrangement. This phenomenon, which originates from the interaction between matter and X-rays, serves as the basis for three-dimensional structural analysis. In this section, we begin by introducing the X-ray diffractometer used in our study. Next, we provide an overview of the key principles involved in data acquisition, as well as the processing and correction methods employed. The refined diffraction data are then utilized to solve and refine the crystal structure of the compound under investigation.

II.2.1 Principle of experimentation

When X-rays interact with a solid material, they encounter the electrons that orbit the atomic nuclei, resulting in a scattering effect. These scattered waves are emitted in a variety of directions, and their behavior is governed by the principles of wave interference. Depending on their relative phases and directions of propagation, the waves can combine in ways that either amplify or diminish their intensity [1]. Constructive interference occurs when the waves are in phase, leading to significant peaks in intensity that are detectable through experimentation. This phenomenon is particularly evident in crystalline solids, where atoms are arranged in a highly ordered, periodic structure [1]. Such a uniform arrangement dramatically enhances the chances of constructive interference, allowing researchers to capture clear and well-defined diffraction patterns. As a result, X-ray diffraction (XRD) spectra from crystalline materials tend to be straightforward to interpret.

Furthermore, an important relationship exists between the periodicity of the atomic lattice and the resulting diffraction angle. Materials with shorter atomic periodicities yield higher diffraction angles, while those with longer periodicities produce lower angles. This correlation is fundamental to the analysis of crystalline substances and aids scientists in deducing intricate details about their structural properties.

II.2.2 X-ray production

X-rays are generated when electrons are emitted from a tungsten filament that is heated to high temperatures. This process involves stripping electrons from the filament, which is subjected to an intense electric field, usually set at a voltage of 50 kV. The accelerated electrons then collide with a target material known as the anode, or anticathode, producing X-ray radiation as a result of the interaction.

Two of the most commonly used metals for X-ray tube anodes are copper (Cu) and molybdenum (Mo). Copper produces characteristic X-rays with a wavelength of approximately $\lambda = 1.54$ Å, while molybdenum emits X-rays with a shorter wavelength of about $\lambda = 0.709$ Å. These metals are selected based on their characteristic radiation energies, which are suitable for different applications in X-ray diffraction and imaging.

In addition to conventional X-ray tubes, synchrotrons serve as powerful sources of X-rays. A synchrotron accelerates charged particles, such as electrons, to nearly the speed of light and forces them to move in circular paths using magnetic fields. As the electrons change

direction, they emit extremely bright, highly collimated X-rays that can be tuned across a wide range of wavelengths—making synchrotron radiation invaluable for advanced research in materials science, biology, and chemistry.

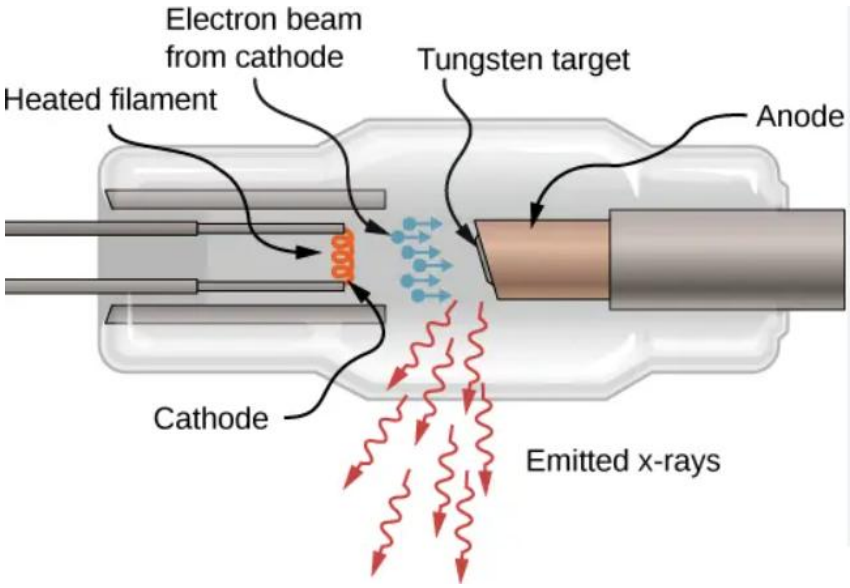


Figure II.1. X-ray production.

Charged particles in motion emit continuous electromagnetic radiation, known as synchrotron radiation, which spans a wide range of frequencies from far ultraviolet to X-rays. The intensity of synchrotron radiation significantly surpasses that of other radiation sources. This technique enables the revelation of fine details and the characterization of crystals with dimensions as small as tens of micrometers [2].

II.2.3 X-ray-matter interaction

II.2.3.1 Analysis of Diffraction and Wave Propagation

The journey toward the discovery of X-ray diffraction commenced with Wilhelm Röntgen's identification of X-rays in 1895. This innovative form of electromagnetic radiation, capable of penetrating various materials, was subsequently associated with the atomic structure of substances by Max von Laue. In 1912, von Laue proposed that crystals could diffract X-rays. The experiments conducted by Laue, along with Friedrich and Knipping, provided compelling evidence that crystals function as three-dimensional diffraction gratings, thereby substantiating the hypothesis of diffraction. The theoretical interpretation of this phenomenon was established by William and Lawrence Bragg, who formulated the Bragg Law.

$$n\lambda = 2dsin\theta \qquad \textbf{(Eq. II. 1)}$$

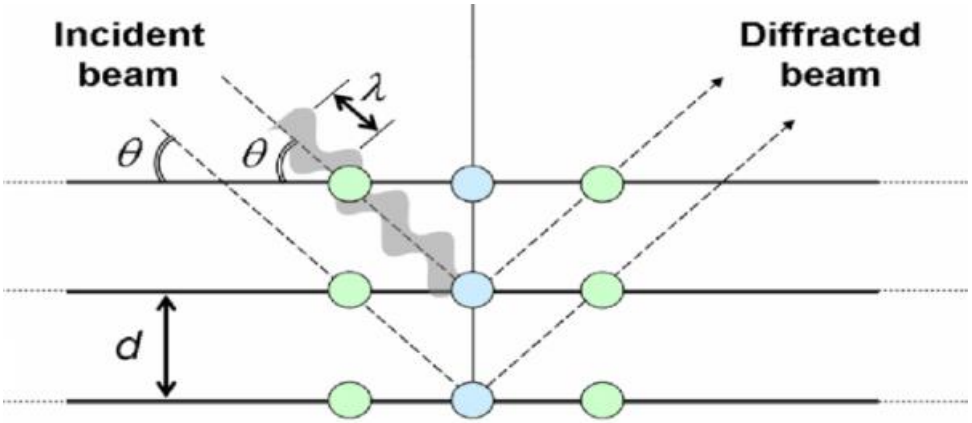


Figure II.2. Diffraction of X-rays- Bragg's law.

The relationship between the diffraction angle (θ), the wavelength (λ), and the interplanar spacing (d) within the crystal lattice is encapsulated in Bragg's Law, which serves as a foundational principle for X-ray crystallography. The introduction of the powder diffraction method by Debye and Scherrer in 1916 significantly facilitated the analysis of powdered samples, thus streamlining the structural investigation process. Over time, single-crystal diffraction emerged as the preferred technique for examining complex structures, particularly in the fields of protein crystallography and materials science [3].

The advent of synchrotron radiation sources in the 1970s represented a substantial advancement in the field, offering intense and coherent X-ray beams. Coupled with advancements in detector technology and analysis software, these innovations have enabled high-resolution structural determinations and the effective processing of extensive datasets [4].

X-ray diffraction occurs when a beam of X-rays interacts with the periodic arrangement of atoms within a crystalline material. As the incident X-rays encounter the electron clouds surrounding the atoms, they are scattered in various directions. Due to the orderly and repeating pattern of the atoms, the scattered waves can interfere with one another in specific directions. In some instances, this interference is constructive, resulting in intense spots or rings known as diffraction patterns. These patterns are informative, as they provide insights into the distances and orientations of the atomic planes within the crystal structure [5]. Through the analysis of these diffraction patterns, researchers can ascertain the internal structure of the material, including atomic positions, symmetry, and lattice parameters. Consequently, X-ray diffraction serves as a robust technique for visualizing the three-dimensional organization of atoms in solid materials. X-ray diffraction occurs when a beam of X-rays interacts with the periodic arrangement of atoms within a crystalline material. As the incident X-rays encounter the

electron clouds surrounding the atoms, they are scattered in various directions. Due to the orderly and repeating pattern of the atoms, the scattered waves can interfere with one another in specific directions. In some instances, this interference is constructive, resulting in intense spots or rings known as diffraction patterns. These patterns are informative, as they provide insights into the distances and orientations of the atomic planes within the crystal structure. Through the analysis of these diffraction patterns, researchers can ascertain the internal structure of the material, including atomic positions, symmetry, and lattice parameters. Consequently, X-ray diffraction serves as a robust technique for visualizing the three-dimensional organization of atoms in solid materials.

II.2.3.2 Elastic and inelastic scattering

When X-rays interact with a crystal, two types of interactions can occur: elastic scattering and inelastic scattering. In elastic scattering, the energy of the X-rays remains conserved, which facilitates the measurement of diffraction angles without loss of information. This process leads to the formation of diffraction patterns that are employed to determine crystal structures.

In contrast, inelastic scattering is considered undesirable in X-ray diffraction (XRD) as it compromises the integrity of the diffraction data by modifying the wavelength of the scattered X-rays.

II.2.3.3 Atomic Diffusion Factor

The intensity of X-rays scattered by each atom is determined by the distribution of its electron density. Each atom can be described by an atomic scattering factor $f_j(\theta)$, which is a function of the diffraction angle θ and the atomic number Z_j of atom j. This factor is given by:

$$\boldsymbol{f_j(\theta) = \sum_j Z_j e^{-\frac{B_j \sin^2 \theta}{\lambda^2}}} \qquad \textbf{(Eq. II. 2)}$$

Where Bj is the Debye-Waller factor, which takes into account the thermal vibrations of atoms, and λ is the wavelength of the beam.

The International Crystallography Tables provide valuable information by illustrating the atomic scattering factor, denoted as fj, in relation to the ratio of sinθ to λ. This relationship is crucial for understanding how atoms interact with X-rays during crystallographic studies.

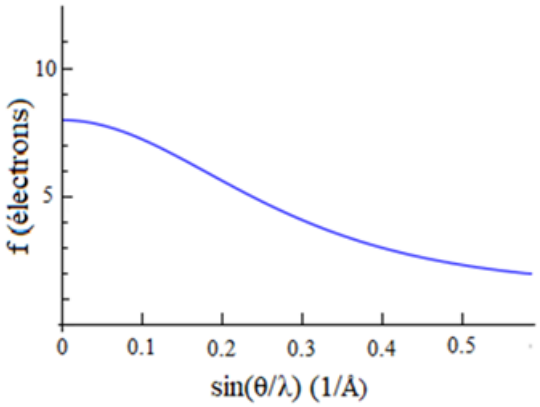


Figure II.3. The diffusion factor as a function of (sin θ)/λ.

II.2.3.4 Structure factor

The structure factor (F) is a crucial quantity in crystallography, representing a value that correlates with the amplitude of the electric field generated by electrons that are affected by an incoming X-ray beam. This factor is derived from the collective contributions of the amplitudes scattered by individual atoms (fj) within a crystal lattice, which is a function of the diffraction angle θ and the atomic number Zj of atom j. By summing these scattered amplitudes, the structure factor provides essential insights into the arrangement and behavior of atoms in the material, ultimately influencing the patterns observed in X-ray diffraction experiments. Its expression is as follows:

$$f_j(\theta) = \sum_j Z_j e^{-\frac{B_j \sin^2\theta}{\lambda^2}} \qquad \textbf{(Eq. II. 3)}$$

The structure factor (F) is influenced by the atomic scattering factor (f_i) and necessitates that the atoms be situated on lattice planes to ensure that their diffraction aligns with Bragg's law. Consequently, the structure factor F is also contingent upon the specific hkl planes, which is why it is indexed as F(hkl). The structure factor can therefore be written in terms of atomic coordinates as follows:

$$F(hkl) = \sum_{j=1}^{N} f_j e^{2\pi i(hx_j+ky_j+lz_j)} \qquad \textbf{(Eq. II. 4)}$$

Where:

N: is the number of atoms in the unit cell,

f_j: is the atomic diffusion factor of atom j,

(x_j,y_j,z_j): are the coordinates of the atoms in the crystal lattice,

h,k,l: are the Miller indices representing the crystal plane.

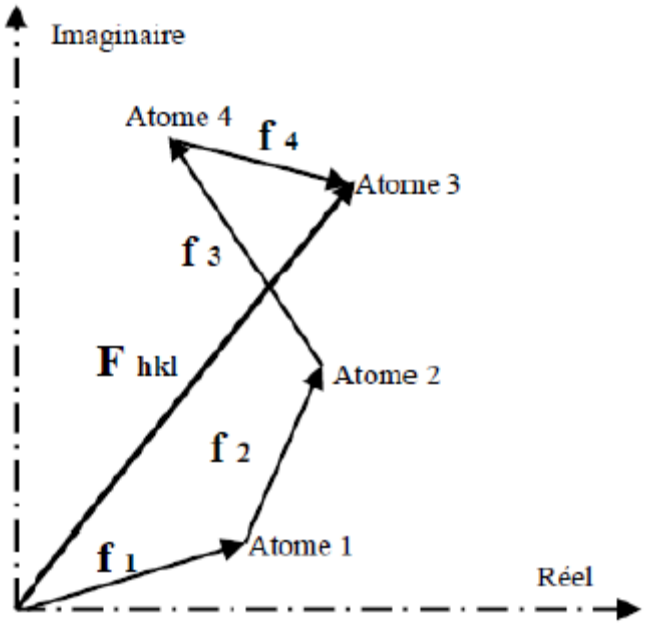


Figure II.4. Structure factor as a function of atomic diffusion factors.

II.2.3.5 Inelastic Scattering and Absorption

Inelastic scattering is a process where X-rays lose energy during their interaction with electrons present in a material. This phenomenon can disrupt the accuracy of diffraction data. To ensure precise results, it is crucial to correct for these inelastic scattering effects [6].

X-rays interact with materials not only through diffraction but also by being absorbed, a phenomenon that can be explained by Beer-Lambert's law. This law describes how the intensity of light decreases as it passes through a medium, providing insight into the absorption characteristics of different materials when exposed to X-rays, expressed by the following equation:

$$I = I_0 e^{-\mu x} \qquad \textbf{(Eq. II. 5)}$$

Where:

- I is the transmitted intensity,
- I_0 is the initial intensity,
- μ is the linear absorption coefficient,
- *x* is the thickness of the sample.

II.3 Intensity Correction

II.3.1 Absorption effects and geometric correction

The intensity of diffraction peaks can be influenced by various factors, one of which is the absorption of X-rays by the crystal. To ensure accurate measurements, absorption correction is essential, as it compensates for the reduction in intensity that occurs when the X-ray beam passes through the material. This correction is critical for obtaining reliable data in diffraction studies.

II.3.2 Absorption correction

The absorption of X-rays by a material is described by Beer-Lambert's law, which has been previously examined. However, in the context of X-ray diffraction (XRD), it is essential to implement more nuanced corrections to account for the different optical paths present within the crystal structure. In the case of single crystal X-ray diffraction, the application of an absorption correction is particularly critical, as it has a direct impact on the intensities of the diffracted beams. The fundamental relationship governing beam attenuation due to absorption can be adjusted for irregularly shaped crystals or when crystals are tilted. This adjustment entails the modification of Beer-Lambert's equation to accommodate geometric variations.

An enhanced version of this law, which considers the specific geometric structure of the crystal, can be expressed through the following integral:

$$I_{corr} = I_0 exp\left(-\mu \int_{trajet} ds\right) \qquad \textbf{(Eq. II. 6)}$$

Where:

- I_{corr} is the intensity corrected after absorption,
- μ is the linear absorption coefficient,
- d_s is an infinitesimal element of the optical path traveled in the crystal.

This correction is especially crucial for crystals with intricate shapes and should be conducted before any quantitative intensity analysis. Modern X-ray diffraction data processing software, such as «SHELX», now incorporates advanced algorithms that make it possible to carry out this correction both accurately and efficiently [7].

II.3.3 Correction for Lorentz and polarization factors

Lorentz and polarization corrections are necessary adjustments that address effects associated with the geometry of diffraction experiments [8].

II.3.3.1 Lorentz factor

The Lorentz factor is an important concept that explains how the probability of observing a specific reflection in a crystal is influenced by the alignment duration of the crystal planes with the incident beam. Specifically, when the crystal rotates at a slower speed, the likelihood of detecting a particular reflection increases. This relationship highlights the significance of both the alignment time and the total number of reflections that occur during the observation process. The Lorentz factor for single-crystal diffraction is written as follows:

$$L = \frac{1}{sin(2\theta)} \qquad (\mathbf{Eq.\ II.\ 7})$$

In this context, θ represents the diffraction angle. This factor diminishes the perceived intensity at elevated 2θ angles.

II.3.3.2 Polarization correction

X-rays generated by either an X-ray tube or a synchrotron exhibit partial polarization. This intrinsic property of the X-rays can significantly influence the intensity of the reflections recorded during experiments such as X-ray diffraction. As a result, it is essential to implement a polarization correction to account for these effects, especially when dealing with diffraction data collected at high angles, where polarization can have a pronounced impact on the intensity measurements. The process of polarization correction involves adjusting the recorded data to compensate for the differential effects of polarization across different scattering angles. The specific equation used for this correction is determined by two critical factors: the degree of polarization of the X-ray beam, which can vary based on the source and experimental setup, and the geometric configuration of the experiment itself, including sample orientation and detector positioning. Understanding these variables is crucial for obtaining accurate and reliable results in X-ray scattering experiments, and can be written as:

$$P = \frac{1+\cos^2(2\theta)}{2} \qquad (\mathbf{Eq.\ II.\ 8})$$

Thus, reflections at higher diffraction angles (2θ) undergo a greater correction to account for this polarization.

II.3.3.3 Effect of temperature: the Debye-Waller factor

The temperature factor, commonly referred to as the Debye-Waller factor, serves as a correction mechanism to accommodate the influence of thermal vibrations of atoms on diffraction intensities. At room temperature, atomic entities oscillate around their average positions within the crystal lattice. This behavior results in the scattering of X-rays, which subsequently diminishes the intensities of the diffracted beams.

The Debye-Waller factor is generally expressed by an exponential attenuation of the diffracted intensities according to the relationship:

$$I_{corr} = I_0 exp\left(-\frac{2\,B\,\sin^2\theta}{\lambda^2}\right) \qquad \textbf{(Eq. II. 9)}$$

Where:

- B is the Debye-Waller factor (or thermal factor),
- θ is the Bragg angle,
- λ is the wavelength of the X-rays.

This factor is instrumental in the refinement of structures exposed to high temperatures and is critical in the analysis of materials subjected to specific thermal conditions. Its significance lies in the ability to enhance material properties and performance in high-heat environments, which is essential for various applications. Furthermore, understanding this factor enables researchers and professionals to assess how thermal exposure influences material behavior, thereby contributing to advancements in fields such as aerospace, automotive, and energy.

II.4 DRX of Single Crystals

II.4.1 Principle of monocrystal XRD

In contrast to powder diffraction, which involves the orientation of crystals in multiple directions, single-crystal diffraction necessitates the precise orientation of the crystal. This meticulous alignment facilitates the collection of data on specific crystallographic planes, thereby yielding higher resolution and more comprehensive insights into the atomic structure.

The standard procedure for conducting a diffraction experiment on single crystals involves the rotation of the crystal within an X-ray beam to capture diffraction patterns at

various angles. Analyzing diffraction from single crystals is crucial for fully covering the three-dimensional reciprocal space.

Diffraction on single crystals adheres to Bragg's law; however, it necessitates a more comprehensive analysis of the diffracted intensities and diffraction angles to derive insights regarding the crystal parameters and atomic positions [3].

II.4.2 Crystal Parameters and Crystal Systems

Single crystals exhibit three-dimensional periodicity, and specific crystal parameters define their structure. The crystal lattice is defined by:

- The lengths of the edges (a, b, c).
- The angles between the edges (α, β, γ).

Crystal systems are classified into seven categories: cubic, tetragonal, orthorhombic, rhombohedral, hexagonal, monoclinic, and triclinic. Each system possesses distinct symmetries that affect the diffraction of X-rays.

II.4.3 Miller Indices and Interplanar Distance

Miller indices, denoted as (hkl), are utilized to represent crystallographic planes by indicating their orientation within the crystal lattice. Each index h, k, and l corresponds to the reciprocal of the points where the plane intersects the crystal axes a, b, and c, respectively. This system provides a standardized way to describe the geometry of crystal structures.

The interplanar distance dhkl between two parallel planes in a cubic crystal is given by:

$$d_{hkl} = \frac{a}{\sqrt{h^2 + k^2 + l^2}} \qquad \textbf{(Eq. II.10)}$$

In this context, "a" denotes the length of the crystal lattice. For other crystallographic systems, the corresponding formulae tend to be more intricate; however, they adhere to a similar fundamental principle.

II.5 II.5 Data Recording and Processing

II.5.1 Representation in Reciprocal Space

Reciprocal space is a mathematical representation that simplifies calculations in crystallography. It defines the positions of the diffraction spots observed during an XRD

experiment. In this space, each diffraction spot corresponds to a point that represents a set of crystallographic planes.

In reciprocal space, the diffraction vector Q associated with an hkl reflection is related to the real parameters by the following relationship:

$$|\boldsymbol{Q}| = \frac{\boldsymbol{2\pi}}{\boldsymbol{d_{hkl}}} \qquad (\textbf{Eq. II. 11})$$

This means that the closer the atomic planes are to each other, the longer the diffraction vectors are in reciprocal space.

II.5.2 Methods for integrating intensities

The process of intensity integration is a critical phase in crystallographic analysis, wherein the numerical values of the intensities corresponding to the diffracted beams are meticulously extracted from the observed diffraction spots. This operation plays a vital role in the overall analysis, as the accuracy of these intensity values is directly linked to the structure factors F(hkl). These structure factors encapsulate the essence of the crystal's atomic arrangement, representing the cumulative contributions of the waves that have been diffracted by each atom within the crystal lattice. The precise determination of these intensities is essential for accurately interpreting the structural characteristics of the material under study.

The integration of intensities can be performed using specialized software such as "XDS" or "SHELX," which analyzes diffraction images and calculates the intensities corresponding to each reflection **[9]**. The relationship between the intensity of a reflection and the structure factor is given by:

$$\boldsymbol{I(hkl) \propto |F(hkl)|^2} \qquad (\textbf{Eq. II. 12})$$

II.5.3 Solving the Phase Problem

In an X-ray diffraction (XRD) experiment, researchers focus primarily on measuring the intensities of the diffracted reflections that arise when X-rays interact with a crystalline sample. However, a significant challenge arises because the phases of these diffracted waves, which are essential for accurately reconstructing the electronic density of the crystal structure, remain elusive. This limitation is commonly known as the phase problem. To address this issue, scientists have developed a variety of techniques aimed at estimating the missing phases, allowing for a more complete understanding of the crystal's internal arrangement and properties. These advancements are crucial for advancing materials science and related fields.

II.5.3.1 Patterson method

Patterson's method involves calculating the Patterson function, which is derived from the Fourier transform of the measured intensities. This approach is essential in crystallography for resolving the positions of atoms within a crystal structure. This function is defined as follows:

$$P(u) = \sum_{hkl} |F(hkl)|^2 e^{2\pi i(hu_x + ku_y + lu_z)} \qquad \text{(Eq. II. 13)}$$

Where u is a displacement vector in real space, and F(hkl) is the structure factor associated with the Miller indices hkl.

The Patterson function provides a detailed representation of interatomic distances within a crystal structure, facilitating the estimation of the relative positions of heavy atoms. This methodology is particularly advantageous for resolving structures that include heavy atoms, such as those found in metallic entities.

II.5.3.2 Direct Methods

Direct methods rely on probabilistic calculations and the interrelationships between the amplitudes and phases of reflections. These techniques utilize triplet and quartet relationships among phases to estimate the missing phases in a given dataset. They are particularly effective for small molecules and straightforward structures, where sufficient data exists to apply these mathematical relationships appropriately **[9]**.

II.5.3.3 Anomalous Diffraction

Anomalous diffraction is a sophisticated technique that capitalizes on the variation in X-ray scattering as a function of wavelength, in conjunction with the specific properties of atoms within a crystal structure. By employing X-rays that are proximate to the absorption edges of certain elements, such as transition metals, it becomes feasible to retrieve information regarding missing phases. This methodology is particularly advantageous for analyzing biological macromolecules.

II.5.4 Fourier synthesis

After successfully recovering the phases through the previously mentioned methods, Fourier synthesis can then be employed to reconstruct the electron density within the crystal.

The electron density ρ(x,y,z) is obtained by the inverse Fourier transform of the structure factors F(hkl):

$$\boldsymbol{\rho(x,y,z) = \frac{1}{V}\sum_{hkl} F(hkl)e^{-2\pi i(hx+ky+lz)}} \qquad \textbf{(Eq. II. 14)}$$

The electron density is utilized to ascertain the atomic positions within the crystal lattice. By refining these positions to optimize the alignment between the empirical data and the theoretical model, one can derive an initial approximation of the crystal structure.

II.6 Resolution and Structure Refinement

Following the determination of an initial model of the atomic structure of a crystal based on the diffracted intensities, it is necessary to refine this model to ensure it accurately aligns with the experimental data.

II.6.1 Refinement of crystal parameters using the least squares method

Refinement is performed using the least squares method, which involves adjusting the model parameters to minimize the difference between the observed intensities I_{obs} (hkl) and the intensities calculated I_{calc} (hkl) from the model. This adjustment aims to minimize the following function:

$$\boldsymbol{S = \sum_{hkl} \omega(hkl)(|F_{obs}(hkl)| - |F_{calc}(hkl)|)^2} \qquad \textbf{(Eq. II. 15)}$$

Where ω(hkl) is a weighting factor, and F_{obs} (hkl) and F_{calc} (hkl) are the observed and calculated structure factors for the hkl reflections, respectively.

II.6.2 Reliability factors and convergence criteria

Reliability factors, often denoted as R (unweighted) and Rω (weighted), are used to measure the degree of fit between experimental data (measured intensities) and values calculated from the crystal model. They provide information on the quality of the crystal structure refinement.

The R factor is a measure of the overall quality of the fit between observed intensities and calculated intensities, but without taking into account the uncertainties associated with the data, and whose relationship is as follows:

$$R = \sqrt{\frac{\sum (|F_{obs}|^2 - |F_{calc}|^2)^2}{\sum (|F_{obs}|)^2}} \qquad \textbf{(Eq. II. 16)}$$

The Rω factor introduces a weighting for each observation, taking uncertainties into account. It is given by:

$$R_{\omega} = \sqrt{\frac{\sum \omega(|F_{obs}|^2 - |F_{calc}|^2)^2}{\sum \omega(|F_{obs}|)^2}} \qquad \textbf{(Eq. II. 17)}$$

Where ω is the weighting factor defined by:

$$\omega = \frac{1}{\sigma^2\left(F_{obs}{}^2\right) + a\rho^2 + b\rho} \qquad \textbf{(Eq. II. 18)}$$

σ represents the uncertainty on Fobs, and a and b are empirical constants adjusted to optimize the weighting based on the measured data.

An R and Rω close to 0 indicates a good fit, meaning that the model and the experimental data are in agreement. If R and Rω are greater than or equal to 1, this means that the differences between the calculated and observed intensities are significant. Therefore, the structural model does not correspond to the data with the expected accuracy [9].

II.6.3 Multipolar Refinement

II.6.3.1 Independent Atom Model (IAM)

The Independent Atom Model (IAM) represents the conventional starting point in crystallographic refinement of molecular structures obtained from X-ray diffraction experiments. In this approximation, each atom is considered as an isolated spherical entity whose electron density is assumed to be unaffected by chemical bonding or by the surrounding crystalline environment [10]. Consequently, the observed diffracted intensities are modeled as the sum of spherical atomic scattering factors according to the following expression:

$$F(\mathbf{H}) = \sum_j f_j(\mathbf{H}) \exp\left(2\pi i \mathbf{H} \cdot \mathbf{r}_j\right) \exp\left(-B_j s^2\right) \qquad \textbf{(Eq. II. 19)}$$

where $f_j(\mathrm{H})$is the atomic scattering factor of atom j, $\mathrm{r}_j$is its crystallographic position, $B_j$is the thermal displacement parameter, and $s = \sin\theta/\lambda$. This model generally provides reliable geometric information such as bond lengths, bond angles, and molecular conformation. However, IAM fails to describe the true experimental electron density because electrons involved in covalent bonds, lone pairs, and polarization effects do not possess spherical

symmetry [11]. Therefore, although IAM is indispensable as an initial refinement procedure, it remains insufficient for accurate charge density investigations.

II.6.3.2 Difference Fourier Series Method

To reveal the limitations of the spherical atom approximation, the Difference Fourier Series method is employed to calculate the residual electron density between the experimentally observed structure factors and those calculated from the IAM refinement. The residual density is expressed as:

$$\Delta\rho(\mathbf{r}) = \frac{1}{V}\sum_{\mathbf{H}} (|\, F_{obs}(\mathbf{H})\,| - |\, F_{calc}(\mathbf{H})\,|)\exp(i\phi_{calc})\exp(-2\pi i \boldsymbol{H}\cdot\boldsymbol{r}) \qquad \textbf{(Eq. II. 20)}$$

where V is the unit-cell volume, F_{obs} and F_{calc} are the observed and calculated structure factors, respectively, and ϕ_{calc} is the phase angle derived from the refined model [12]. This Fourier difference map highlights the regions where the spherical model does not adequately reproduce the experimental density. Positive residual peaks are usually found in covalent bond regions or near lone electron pairs, whereas negative residual regions indicate overestimation by the spherical approximation. Hence, this method acts as a diagnostic bridge between the classical IAM treatment and more advanced aspherical electron density modeling.

II.6.3.3 Multipolar Electron Density Model According to Hansen and Coppens

In order to overcome the intrinsic deficiencies of the Independent Atom Model, Hansen and Coppens proposed in 1978 a multipolar formalism capable of describing the aspherical distribution of atomic electron density with much greater realism **[13]**. In this theoretical framework, the electron density of each atom is partitioned into three principal components: a spherical core density, a spherical valence density, and an aspherical multipolar deformation density accounting for chemical bonding and charge redistribution.

The general Hansen–Coppens electron density expression is given by:

$$\boldsymbol{\rho}(\mathbf{r}) = \boldsymbol{\rho_{core}}(\boldsymbol{r}) + \boldsymbol{P_{val}}\boldsymbol{\kappa}^3\boldsymbol{\rho_{val}}(\boldsymbol{\kappa r}) + \sum_{l=0}^{l_{max}} \boldsymbol{\kappa'}^3\, \boldsymbol{R_l}(\boldsymbol{\kappa' r}) \sum_{m=-l}^{+l} \boldsymbol{P_{lm}}\, \boldsymbol{Y_{lm}}(\boldsymbol{\theta},\boldsymbol{\phi}) \qquad \textbf{(Eq. II. 21)}$$

where:

- $\rho_{core}(r)$ denotes the spherical core electron density;
- $\rho_{val}(r)$ represents the spherical valence electron density;
- P_{val} is the valence electron population;

- $\kappa$and $\kappa'$are radial expansion/contraction parameters;
- $R_l$corresponds to Slater-type radial functions;
- $Y_{lm}(\theta, \phi)$are real spherical harmonics;
- $P_{lm}$are multipole population parameters describing angular deformation.

The first term represents the chemically inert inner-shell electrons, the second adjusts the spherical valence shell, whereas the third term introduces the angular deformation of the electron cloud arising from covalent bonding, lone pairs, intermolecular interactions, and polarization phenomena [14-15]. Through this formalism, the electron density is no longer constrained to spherical symmetry but is allowed to reproduce the real anisotropic distribution observed experimentally.

The multipolar refinement procedure consists of simultaneously adjusting structural and multipole population parameters in order to minimize the residual function:

$$\sum \boldsymbol{w}(|\boldsymbol{F_{obs}}| - |\boldsymbol{F_{calc}}|)^2 \rightarrow \mathbf{min} \qquad (\mathbf{Eq.\ II.22})$$

where $w$is the weighting factor associated with each reflection. Such refinement provides a highly accurate reconstruction of the experimental charge density and allows extraction of chemically meaningful properties including electrostatic potential, atomic charges, dipole moments, and intermolecular interaction analysis [15-16]. Consequently, the Hansen–Coppens model has become the reference theoretical basis for modern experimental charge density studies in molecular crystallography

II.6.3.4 Refinement Strategy and Software (MoPro)

The refinement of the crystal structure and electron-density distribution was carried out using the Hansen–Coppens multipolar formalism implemented in the software packages MoPro Suite. The refinement procedure started with a conventional spherical atom refinement based on the Independent Atom Model (IAM), which provided accurate atomic coordinates and anisotropic displacement parameters. After achieving convergence, a multipolar refinement was performed in order to model the aspherical distribution of electron density around atoms more realistically. In the Hansen–Coppens approach, the total electron density is divided into core, spherical valence, and deformation density contributions, allowing a detailed description of chemical bonding and intermolecular interactions [17]. During the refinement process, the scale factor, atomic positions, thermal displacement parameters, valence populations, multipole populations, and expansion–contraction coefficients were refined progressively to reduce parameter correlation and improve the stability of the model. The quality and reliability of the

final model were evaluated through statistical indicators such as the agreement factors $R(F)$, weighted residual factors $wR(F)$ goodness of fit values, and residual electron-density maps. These refinement strategies are widely used in high-resolution charge-density studies because they provide valuable information about electron delocalization, atomic charge distribution, and the nature of intermolecular interactions within crystalline materials **[18-19]**. Furthermore, the refined electron-density model can be analyzed within the framework of the Quantum Theory of Atoms in Molecules to investigate the topological properties of chemical bonds and weak intermolecular contacts **[19]**.

II.6.3.5 Derivation of Topological Properties from Multipolar Density

The topological properties of the electron density were derived from the refined multipolar model within the framework of Quantum Theory of Atoms in Molecules (QTAIM), developed by Bader **[20]**. In this approach, the experimental electron density obtained from multipolar refinement is analyzed to identify critical points and characterize the nature of chemical bonds and intermolecular interactions. The topology of the electron density is described through several parameters evaluated at the bond critical points (BCPs), including the electron density $\rho(r)$, the Laplacian of the electron density $\nabla^2\rho(r)$, and the energy density components. These topological descriptors provide valuable insight into the strength, covalent character, and polarity of chemical interactions. Covalent bonds are generally associated with high electron-density values and negative Laplacian values at the BCP, whereas closed-shell interactions such as hydrogen bonds and van der Waals contacts exhibit lower electron density and positive Laplacian values **[21-22]**. The derivation of these properties from multipolar electron density enables a detailed understanding of charge transfer, electron delocalization, and intermolecular stabilization mechanisms in crystalline systems. Such analyses have become essential in modern charge-density studies because they establish a direct relationship between experimental electron density and the electronic structure of molecular materials **[23]**.

II.6.3.6 The Electron Density and Its Gradient Field

The electron density ρ(r) is a scalar field that describes the probability of finding an electron at a given point r in space. It is defined as:

$$\rho(\mathbf{r}) = N \int \cdots \int |\Psi(\mathbf{r}, \mathbf{r_2}, \ldots, \mathbf{r^N})|^2 \, d\mathbf{r_2} \cdots d\mathbf{r^N} \qquad \textbf{(Eq. II.23)}$$

where N is the number of electrons and Ψ is the many-electron wave function. The electron density is a real, experimentally accessible quantity that can be obtained from high-resolution X-ray diffraction combined with multipole refinement [24].

The topology of ρ(r) is analyzed through its gradient vector field ρ(r), which at every point in space points in the direction of the steepest increase of the electron density:

$$\nabla\rho(r) = (\partial\rho/\partial x)\hat{i} + (\partial\rho/\partial y)\hat{j} + (\partial\rho/\partial z)\hat{k} \qquad \textbf{(Eq. II.24)}$$

The gradient vector field defines a set of trajectories, called gradient paths, that originate in regions of minimum electron density and terminate at local maxima corresponding to nuclear positions. This gradient field partitions real space into non-overlapping atomic basins, forming the physical basis of the QTAIM partitioning scheme.

II.6.3.7 Critical Points: Definition and Classification

A critical point (CP) is a point r^c in space where the gradient of the electron density vanishes identically:

$$\nabla\rho(r^c) = 0 \qquad \textbf{(Eq. II.25)}$$

At a critical point, the local topology of ρ(r) is fully characterized by the Hessian matrix, the symmetric 3×3 matrix of all second-order partial derivatives of ρ(r):

$$H_{ij} = \partial^2\rho \,/\, \partial x_i\, \partial x_j \qquad \textbf{(Eq. II.26)}$$

Diagonalization of H through a unitary transformation yields three real eigenvalues $\lambda_1 \leq \lambda_2 \leq \lambda_3$, each corresponding to the curvature of ρ(r) along its associated principal axis. Critical points are categorized by two integers: the rank (r), defined as the number of non-zero eigenvalues, and the signature (s), defined as the algebraic sum of the signs of the eigenvalues. For a stable, non-degenerate critical point, r = 3, and four types of CPs are possible:

Table II.1. Classification of critical points in QTAIM analysis

CP Type	Notation	Eigenvalue Signs	Physical Meaning
Nuclear Critical Point (NCP)	(3, −3)	$\lambda_1 < \lambda_2 < \lambda_3 < 0$	Local maximum; located at nuclear positions
Bond Critical Point (BCP)	(3, −1)	$\lambda_1 < \lambda_2 < 0 < \lambda_3$	Saddle point between two bonded atoms
Ring Critical Point (RCP)	(3, +1)	$\lambda_1 < 0 < \lambda_2 < \lambda_3$	Found within atomic ring structures
Cage Critical Point (CCP)	(3, +3)	$0 < \lambda_1 < \lambda_2 < \lambda_3$	Local minimum; enclosed within cage structures

The presence and connectivity of these critical points must satisfy the Poincaré–Hopf relationship:

$$n^{Nc}{}_p - n^{Bc}{}_p + n^{Rc}{}_p - n^{cc}{}_p = 1 \qquad \textbf{(Eq. II.27)}$$

This topological invariant serves as an important consistency check in any QTAIM analysis and must be satisfied for a chemically valid topology [25].

II.6.3.8 The Laplacian of the Electron Density

The Laplacian $\nabla^2\rho(r)$ is defined as the trace of the Hessian matrix and equals the sum of the three curvature eigenvalues:

$$\nabla^2\rho(r) = \lambda_1 + \lambda_2 + \lambda_3 = \partial^2\rho/\partial x^2 + \partial^2\rho/\partial y^2 + \partial^2\rho/\partial z^2 \qquad \textbf{(Eq. II.28)}$$

The Laplacian is of central importance in QTAIM because it reveals regions where electron density is locally concentrated ($\nabla^2\rho < 0$) or locally depleted ($\nabla^2\rho > 0$) relative to its surroundings. This physical interpretation follows directly from the signs and magnitudes of the individual eigenvalues at the BCP:

λ_1 and λ_2 (negative) — curvatures perpendicular to the internuclear axis. Their negative values indicate that $\rho(r)$ is concentrated in the plane perpendicular to the bond at the BCP, reflecting electron sharing between atoms.

Λ_3 (positive) — curvature along the internuclear axis. Its positive value indicates that $\rho(r)$ is depleted along the bond direction, as electrons are drawn toward the nuclear attractors.

Accordingly, the sign of the Laplacian reflects the competition between these opposing curvatures:

$$\nabla^2\rho < 0 \Rightarrow |\lambda_1 + \lambda_2| > \lambda_3 \quad \textbf{(shared/covalent interaction)} \qquad \textbf{(Eq. II.29)}$$

$$\nabla^2\rho > 0 \Rightarrow \lambda_3 > |\lambda_1 + \lambda_2| \quad \textbf{(closed-shell interaction)} \qquad \textbf{(Eq. II.30)}$$

The Laplacian also identifies the valence shell charge concentrations (VSCCs) and charge depletions around atomic centers, providing a direct link to the Lewis model of chemical bonding and the VSEPR theory of molecular geometry [26].

II.6.3.9 Bond Ellipticity and the π Character of Chemical Bonds

The two negative eigenvalues λ_1 and λ_2 at a BCP are not necessarily equal in magnitude. Their difference encodes information about the cylindrical symmetry of the bond, quantified through the bond ellipticity ε:

$$\varepsilon = (\lambda_1 / \lambda_2) - 1 \quad (\lambda_1 \leq \lambda_2 < 0) \qquad \textbf{(Eq. II.31)}$$

For a bond with perfect cylindrical symmetry, such as a pure σ bond $\lambda_1 = \lambda_2$ and thus $\varepsilon = 0$. Deviation from zero indicates a preferential accumulation of electron density in one plane, which is characteristic of π bonding. The ellipticity, therefore, provides a sensitive measure of the double-bond character and is particularly informative for:

- **Aromatic systems**, where ε values reflect partial π delocalization.
- **Conjugated bonds**, where ε correlates with bond order.
- **Intermolecular interactions**, where high ε may indicate geometric instability or anisotropy.

II.6.3.10 Energy Density Analysis at the Bond Critical Point

A more complete characterization of chemical bonding is obtained through the local energy densities evaluated at the BCP. The total energy density H(r) is defined as:

$$H(r)=G(r)+V(r) \qquad \textbf{(Eq. II.32)}$$

where G(r) is the kinetic energy density (always positive) and V(r) is the potential energy density (always negative). These quantities are connected through the local virial theorem:

$$(1/4)\nabla^2\rho(r) = 2G(r) + V(r) \qquad \textbf{(Eq. II.33)}$$

which allows G(r) to be estimated from the electron density via the approximation of Kirzhnits, and V(r) subsequently derived from the virial relation. The ratio of potential to kinetic energy density defines an additional bonding descriptor:

$$|V(r)| / G(r) \qquad \textbf{(Eq. II.34)}$$

The combination of $\nabla^2\rho$ and H(r) at the BCP provides a rigorous classification of interactions as proposed by Espinosa et al. [22]:

Table II.2. Topological criteria for interaction types

Criterion	Interaction Type
$\nabla^2\rho < 0,\ H < 0$	Shared (covalent) — strong electron sharing
$\nabla^2\rho > 0,\ H < 0$	Intermediate — partially covalent (e.g., strong H-bonds)
$\nabla^2\rho > 0,\ H > 0$	Closed-shell — ionic, hydrogen bonds, van der Waals

II.7 Conclusion

This chapter presented the theoretical foundations of crystallographic analysis and multipolar electron-density refinement methods used in modern charge-density studies. Particular attention was given to the principles of single-crystal X-ray diffraction and to the Hansen–Coppens Multipole Model, which provides a more accurate description of the aspherical distribution of electron density in crystalline materials. The refinement strategies implemented in the MoPro Suite software package were also discussed, highlighting their importance in experimental charge-density investigations. In addition, the chapter introduced the derivation of topological properties within the framework of the Quantum Theory of Atoms in Molecules, which enables a deeper understanding of chemical bonding and intermolecular interactions. These theoretical concepts provide an essential basis for the interpretation and analysis of electron-density distributions in crystalline systems.

Bibliographical references

[1] B. Fultz, J. Howe, Transmission Electron Microscopy and Diffractometry of Materials, Springer Berlin Heidelberg, Berlin, Heidelberg, 2013. https://doi.org/10.1007/978-3-642-29761-8.
[2] M. Jean-Luc, Caractérisation expérimentale des matériaux : II : Analyse par rayons X, électrons et neutrons, Presses polytechniques et universitaires romandes, Lausanne, 1998.
[3] F.F. B.A, F.Z.S, Elements Of X Ray Diffraction, (1958) 1–347.
[4] S.S. Karki, V.S. Bahaduria, V. Rana, S. Kumar, P.G. Subbaro, U. Das, J. Balzarini, E. De Clercq, J.R. Dimmock, 1-Arylmethyl-2,3-dioxo-2,3-dihydroindole thiosemicarbazones as leads for developing cytotoxins and anticonvulsants, J. Enzyme Inhib. Med. Chem. 24 (2009) 537–544. https://doi.org/10.1080/14756360802234885.
[5] C.-T. Chiou, W.-C. Lee, J.-H. Liao, J.-J. Cheng, L.-C. Lin, C.-Y. Chen, J.-S. Song, M.-H. Wu, K.-S. Shia, W.-T. Li, Synthesis and evaluation of 3-ylideneoxindole acetamides as potent anticancer agents, Eur. J. Med. Chem. 98 (2015) 1–12. https://doi.org/10.1016/j.ejmech.2015.04.062
[6] J. de Meulenaer, H. Tompa, The absorption correction in crystal structure analysis, Acta Crystallogr. 19 (1965) 1014–1018. https://doi.org/10.1107/S0365110X65004802.
[7] W.R. Busing, H.A. Levy, High-speed computation of the absorption correction for single-crystal diffraction measurements, Acta Crystallogr. 10 (1957) 180–182. https://doi.org/10.1107/S0365110X57000584.
[8] C. Giacovazzo, H.L. Monaco, D. Viterbo, F. Scordari, G. Gilli, G. Zanotti, M. Catti, C. Giacovazzo, P. Paufler, Fundamentals of Crystallography. International Union of Crystallography, Oxford Univ. Press 1992, 654 p. Pb. £ 27.50. ISBN 0-19-855578-4, Cryst. Res. Technol. 28 (1993) 370–370. https://doi.org/10.1002/crat.2170280318.
[9] A.G. J. J. Rousseau, Cristallographie géométrique et radiocristallographie, Paris, 2007.
[10] Giacovazzo, C. et al. Fundamentals of Crystallography. Oxford University Press, 2011.
[11] Massa, W. Crystal Structure Determination. Springer, 2010.
[12] Ladd, M. F. C., & Palmer, R. A. Structure Determination by X-ray Crystallography. Springer, 2003.
[13] Hansen, N. K., & Coppens, P. Testing aspherical atom refinements on small-molecule data sets. Acta Crystallographica A, 34 (1978) 909–921.
[14] Coppens, P. X-ray Charge Densities and Chemical Bonding. Oxford University Press, 1997.
[15] Koritsanszky, T., & Coppens, P. Chemical applications of X-ray charge-density analysis. Chemical Reviews, 101 (2001) 1583–1627.

[16] Hansen, N. K.; Coppens, P. (1978). "Testing aspherical atom refinements on small-molecule data sets." Acta Crystallographica Section A, 34, 909–921.
[17] Jelsch, C.; Guillot, B.; Lagoutte, A.; Lecomte, C. (2005). "Advances in protein and small-molecule charge-density refinement methods using MoPro." Journal of Applied Crystallography, 38, 38–54.
[18] Volkov, A.; Macchi, P.; Farrugia, L. J.; Gatti, C.; Mallinson, P.; Richter, T.; Koritsanszky, T. (2016). XD2016: A multipole refinement and topological analysis package for crystal electron densities.
[19] Bader, R. F. W. (1990). Atoms in Molecules: A Quantum Theory, Oxford University Press
[20] Bader, R. F. W. Atoms in Molecules: A Quantum Theory, Oxford University Press, 1990.
[21] Koch, U.; Popelier, P. L. A. "Characterization of C–H–O Hydrogen Bonds on the Basis of the Charge Density." Journal of Physical Chemistry, 1995, 99, 9747–9754.
[22] Espinosa, E.; Molins, E.; Lecomte, C. "Hydrogen bond strengths revealed by topological analyses of experimentally observed electron densities." Chemical Physics Letters, 1998, 285, 170–173.
[23] Coppens, P. X-ray Charge Densities and Chemical Bonding, Oxford University Press, 1997
[24] B.Fournier, « Modélisation des propriétés électrostatiques des complexes macromoléculaires à partir des données de diffraction des rayons X à très haute résolution », Nancy I, (2010).
[25] C. Lecomte, M. Souhassou, S. Pillet, Journal of Molecular Structure. 647, 53–64, (2003).
[26] E. Espinosa, M. Souhassou, H. Lachekar, C. Lecomte, Acta Cryst. 855,563- 572, (1999).

CHAPTER III

Quantum Chemical Methods and DFT Approaches in Molecular Modeling

III.1 Introduction 44
III.2 Theoretical foundations of quantum mechanics 44
III.2.1 The wave function 46
III.2.2 Hamiltonian formulation of the energy of a system 46
III.3 The Schrödinger Equation: The Heart of Quantum Chemistry 47
III.4 The Born–Oppenheimer Approximation: Decoupling Motion 48
III.5 The Hartree-Fock Method 49
III.5.1 The Orbital Approximation 49
III.5.2 Slater determinants: A mathematical form of the Pauli principle 50
III.5.3 Constructing molecular orbitals: The LCAO approximation 50
III.5.4 Roothaan Formulation of the Hartree–Fock Method 51
III.5.5 Beyond the Hartree–Fock Approximation 52
III.6 Density Functional Theory (DFT) 52
III.6.1 Local density approximation (LDA) 54
III.6.2 The generalized gradient approximation (GGA) 55
III.6.3 Hybrid Functions 55
III.7 Basis functions 56
III.7.1 Fundamental Functions in Quantum Chemistry 56
III.7.1.1 Slater Type Functions (STO) 56
III.7.1.2 Gaussian Type Functions (GTO) 57
III.7.1.3 Basic Split-Valence Functions 58
Bibliographical references 60

III.1 Introduction

Quantum chemistry [1] is one of the pillars of modern theoretical chemistry. It aims to describe and understand, at the atomic and subatomic scales, the properties and behavior of systems made up of atoms and molecules. This field is based on the foundations of quantum mechanics, a revolutionary theory elaborated at the beginning of the XX^{e} century by physicists such as Planck, Bohr, Schrödinger, and Heisenberg. Schrödinger's equation [2], in particular, occupies a central position, since it allows us to determine, in principle, the electronic structure and energy levels of the systems under study. However, the exact resolution of this equation quickly becomes unaffordable as the number of particles increases, due to the exponential complexity of interactions between electrons and nuclei.

To overcome this difficulty, numerous approximations and numerical methods have been developed over the last century. Among the most important are the Hartree-Fock method and density functional theory (DFT), which are now the most widely used tools in computational chemistry. Although based on simplifications of the initial problem, these approaches provide satisfactory accuracy for a wide range of practical applications. In particular, they enable us to predict and interpret a wide range of molecular properties, such as electronic structures, absorption and emission spectra, the nature of chemical bonds, and reaction mechanisms.

Thus, quantum chemistry is not limited to a theoretical role; it constitutes a genuine predictive and interpretative tool, whose impact extends to fields ranging from the fundamental understanding of chemical reactions to the design of new materials with specific properties [3]. This chapter will be devoted to presenting the basic concepts of quantum chemistry and examining the main computational methods employed. Emphasis will be placed on their theoretical foundations, advantages, and limitations, to provide a clear methodological framework for the applications developed in this thesis.

III.2 Theoretical foundations of quantum mechanics

Quantum mechanics constitutes one of the fundamental pillars of contemporary physics. It originated in the early 20th century as a theoretical framework to elucidate experimental phenomena that classical mechanics could not adequately account for, particularly concerning the behavior of subatomic particles, atoms, and molecules. In contrast to classical laws, which effectively describe macroscopic systems, quantum mechanics applies to minuscule entities

such as electrons, protons, and photons [4-6]. This field is founded upon several key principles, including energy quantization, wave-particle duality, and the uncertainty principle. These principles have significantly transformed our comprehension of microscopic interactions and have facilitated the development of novel theoretical and experimental methodologies.

- The principle of wave-particle duality is a critical concept in quantum mechanics, asserting that subatomic particles inherently possess both wave and particle characteristics. This dual nature empowers them to exist as either waves or as distinct material particles, profoundly shaping their behavior and interactions in the quantum realm.
- The quantum state of a system is described by a mathematical function called a wave function. This function contains all the information relating to the system, including its position, energy, and momentum.
- The Schrödinger equation [7] is the central axis of quantum mechanics. Formulated as a differential equation, it governs the dynamics of quantum systems by describing the temporal evolution of their wave function. This wave function contains all the information relating to the quantum state of a particle or system. The Schrödinger equation is therefore a fundamental tool for modeling and predicting the properties of subatomic particles and molecular systems.
- The principle of superposition is a fundamental concept in quantum mechanics. It asserts that a quantum system can exist simultaneously in multiple states until it is measured. When a measurement is made, the wave function collapses, resulting in the system adopting one of the possible states.
- Heisenberg's uncertainty principle states that it is fundamentally impossible to determine both the position and momentum of a particle with absolute precision at the same time. Any attempt to measure them imposes a limit on precision, reflecting the intrinsic nature of quantum systems.

Quantum mechanics marked a decisive turning point by profoundly influencing disciplines such as atomic physics, quantum chemistry, quantum electronics, and quantum computing, as well as elementary particle theory. It has not only renewed our understanding of matter and light radiation, but has also led to major technological advances that now occupy a central place in modern science and industry [8].

III.2.1 The wave function

The wave function Ψ(r,t) is the fundamental element of quantum mechanics. It characterizes the quantum state of a particle or a set of particles, with r denoting the spatial coordinates and t denoting time. Unlike classical mechanics, which allows the position and velocity of a particle to be determined precisely, quantum mechanics adopts a probabilistic approach [9]. Thus, the probability of locating a particle at a given point r is proportional to the square of the modulus of the wave function:

$$\boldsymbol{P(\mathbf{r},t) = |\Psi(\mathbf{r},t)|^2} \qquad \textbf{(Eq. III. 1)}$$

In quantum mechanics, the wave function must be normalized. This normalization entails that the total probability of locating the particle at any point in space must sum to one. In other words, when we consider all possible positions where the particle could be found, the likelihood of finding it somewhere within that space should equal certainty, represented by the value 1. This requirement ensures that the wave function accurately describes a physical reality, aligning with the fundamental principles of probability.:

$$\int |\, \boldsymbol{\Psi(r,t)}\, |^2 \, \boldsymbol{dr} = \mathbf{1} \qquad \textbf{(Eq. III. 2)}$$

III.2.2 Hamiltonian formulation of the energy of a system

The Hamiltonian is defined as the operator that characterizes the total energy of a system, incorporating both kinetic and potential energy. In the case of a system comprising N electrons and M nuclei, the Hamiltonian can be expressed as:

$$\boldsymbol{\hat{H} = \hat{T}_{\text{elec}} + \hat{T}_{\text{nucle}} + \hat{V}_{\text{elec-elec}} + \hat{V}_{\text{nucle-nucle}} + \hat{V}_{\text{elec-nucle}}} \qquad \textbf{(Eq. III. 3)}$$

With:

- $\hat{T}_{\text{elec}} = -\frac{\hbar^2}{2m_e}\sum_k^n \nabla_k^2$: kinetic energy of the electrons.
- $\hat{T}_{\text{nucle}} = -\frac{\hbar^2}{2}\sum_A^N \frac{1}{M_A}\nabla_A^2$: kinetic energy of nuclei.
- $\hat{V}_{\text{elec-elec}} = \frac{1}{2}\sum_k^n \sum_{k=l}^n \frac{e^2}{4\pi\varepsilon_0 r_{kl}}$: electron repulsion.
- $\hat{V}_{\text{nucle-nucle}} = \frac{1}{2}\sum_A^N \sum_B^N \frac{Z_A Z_B}{4\pi\varepsilon_0 R_{AB}}$: nuclear repulsion.
- $\hat{V}_{\text{elec-nucle}} = -\sum_k^n \sum_A^N \frac{Z_A e^2}{4\pi\varepsilon_0 r_{kA}}$: attraction between electrons and nuclei.

That is:

- e and m_e are the charge and mass of the electron, respectively.

- M_A denotes the mass of nucleus A.
- r_{kA} represents the distance between the k^{ieme} electron and the L^{ieme} nucleus.
- $_{kL}$ denotes the distance between the k^{ieme} electron and the L^{ieme}electron.
- R_{AB} is the distance between nuclei A and B, whose charges are Z_A and Z_B, respectively.
- ε_0 corresponds to the permittivity constant of vacuum, with the relationship where:

$4\pi\varepsilon_0 = 1{,}11265\times10^{-10}J^{-1}C^2m^{-1}$.

This comprehensive formulation facilitates a deeper understanding of the escalating complexity of interactions within a multielectron system **[10]**.

III.3 The Schrödinger Equation: The Heart of Quantum Chemistry

The foundation of quantum chemistry is deeply rooted in quantum mechanics, a revolutionary framework that describes the physical world at the scale of atoms and subatomic particles. Unlike classical physics, which operates on deterministic principles, quantum mechanics introduces concepts such as wave-particle duality, superposition, and the uncertainty principle. These concepts are crucial for accurately modeling the behavior of electrons, which exhibit both wave-like and particle-like characteristics. The central pillar of this theoretical construct is the Schrödinger equation **[11]**:

$$\hat{H}\Psi(r) = E\Psi(r) \qquad \textbf{(Eq. III. 4)}$$

Where:

- $\hat{H}$ represents the Hamiltonian operator, which accounts for the kinetic and potential energies of the electrons and nuclei within a molecular system.
- Ψ (Psi) is the wavefunction, a mathematical function that contains all the probabilistic information about a quantum system, such as the probability of finding an electron at a particular location.
- E is the energy eigenvalue, representing the total energy of the system.

The Schrödinger equation, a fundamental partial differential equation in quantum mechanics, lies at the heart of our comprehension of electronic structure in both atomic and molecular systems. This pivotal equation articulates the behavior of a quantum system by detailing how the wavefunction, an essential mathematical representation of the quantum state, evolves. It also establishes the framework for determining the various energy states that a quantum system can occupy. By meticulously solving the Schrödinger equation, quantum chemists unlock significant insights into the electronic configuration of atoms and molecules.

This knowledge not only reveals the stability and reactivity of different chemical species but also enhances our understanding of their interactions and behaviors at the quantum level. The solutions to this equation are crucial for predicting how substances will react under different conditions, paving the way for advancements in chemistry, materials science, and beyond.

III.4 The Born–Oppenheimer Approximation: Decoupling Motion

One of the most pivotal and extensively utilized approximations in quantum chemistry is the Born–Oppenheimer approximation. This concept arises from the substantial difference in mass between atomic nuclei and electrons. Due to this significant disparity, atomic nuclei, which are significantly heavier, move at a much slower pace compared to their lighter electron counterparts. As a result, the Born–Oppenheimer approximation posits that the movements of the nuclei and the electrons can be treated as separate phenomena [12]. More specifically, when calculating the electronic states of a molecule, it is assumed that the positions of the nuclei remain fixed, ignoring any motion they may have during the time frame of the electronic calculations. This crucial simplification enables the electronic Schrödinger equation to be solved independently of the complexities introduced by nuclear motion, thereby substantially reducing the computational demands typically associated with these calculations. By isolating the electronic behavior from the much slower nuclear dynamics, researchers can more efficiently study and predict the properties of molecular systems.

This approximation simplifies Schrödinger's equation by dividing it into two subproblems: one for electrons and one for nuclei. The total wave function is then expressed as a product:

$$\boldsymbol{\Psi(r,R) = \Psi_{elec}(r|R)\Psi_{nucle}(R)} \qquad \textbf{(Eq. III. 5)}$$

$\Psi (r, R)$: The total wave function, which depends on the electron coordinates r and the nuclear coordinates R.

- $\Psi_{elec} (r/R)$: The electronic wave function, conditioned by the position of the R nuclei.
- $\Psi_{nucle} (R)$: The wave function of nuclei.

In the Born-Oppenheimer approximation, the electronic energy $E_{elec} (R)$ calculated by considering the nuclei as fixed serves as the basis for solving the equation associated with nuclear motion. This separation between electronic and nuclear dynamics greatly simplifies calculations and is particularly well suited to determining potential energy surfaces and analyzing the vibrational and rotational spectra of molecules. However, this approximation

loses its validity in situations where the motions of electrons and nuclei are strongly coupled, such as during non-adiabatic interactions or rapid electronic transitions.

III.5 The Hartree-Fock Method

The Hartree-Fock method was conceived in the 1920s through the pioneering efforts of Douglas Hartree and subsequently refined by Vladimir Fock in 1930. During this period, a significant challenge in the field of early quantum mechanics was the accurate characterization of multi-electron systems, such as atoms and molecules. The presence of electron-electron interactions rendered the equations excessively complex, impeding exact solutions. To address this issue, Hartree proposed the concept of the mean field, wherein each electron is considered to operate not under the direct influence of all other electrons but within a mean potential that encapsulates all interactions. Fock then enhanced this framework by integrating the Pauli exclusion principle, which stipulates that two electrons cannot simultaneously occupy the same quantum state. This refinement made the problem more tractable while adhering to the foundational principles of quantum physics **[13].**

III.5.1 The Orbital Approximation

The complexity inherent in multi-electron systems arises from the intricate interdependencies that govern the motion of each electron. In these systems, every electron experiences a dual influence: it is continually attracted to the positively charged nucleus, while simultaneously feeling the repulsive electrostatic forces exerted by other electrons. This intricate dance of attraction and repulsion leads to a highly correlated movement among the electrons, making it exceedingly challenging to solve the Schrödinger equation accurately for any system containing more than two electrons. To navigate this complexity, physicists and chemists utilize the orbital approximation, a powerful simplification that allows for a more manageable analysis of these systems. This approach involves the assumption that each electron behaves as though it is moving independently within an average electrostatic field, which symbolizes the collective influence of all the other electrons present in the system. By adopting this perspective, we can express the behavior of each electron using a mathematical function known as a single-electron function or orbital, denoted as $\phi i(r)$ **[14]**.

The introduction of the orbital approximation effectively transforms the original many-body problem, where interactions among all electrons must be considered, into a more tractable form consisting of a series of single-body equations. Each equation describes the motion of a single electron in the average potential created by the other electrons, thereby significantly

reducing the mathematical complexity involved in solving the Schrödinger equation. Through this method, researchers can obtain valuable insights into the electronic structure and behavior of multi-electron systems while circumventing the insurmountable difficulties posed by direct solutions to the many-body problem.

III.5.2 Slater determinants: A mathematical form of the Pauli principle

The Pauli exclusion principle, elegantly formulated by physicist Wolfgang Pauli in 1925, asserts a fundamental rule regarding electrons within a given system: no two electrons can occupy the same quantum state simultaneously **[13].** This means that they cannot share the same quantum numbers—specifically, they cannot be in the same orbital while also having identical spins.

This principle highlights the unique characteristics of electrons, classified as fermions; their defining property is that their wave function must undergo a sign change when two indistinguishable particles, such as electrons, are exchanged. Consequently, any mathematical depiction of a system with multiple electrons must ensure that the total wave function displays antisymmetry when any two electrons are swapped **[15]**. In practical terms, physicists employ Slater's determinant as a robust tool to achieve this antisymmetry **[16]**. By utilizing this mathematical construct, a collection of single-electron orbitals can be accurately represented, ensuring compliance with the Pauli exclusion principle and providing a clearer understanding of the complex interactions within multi-electron systems. This antisymmetry is achieved using Slater's determinant:

$$\Psi(\mathbf{r}_1, \dots, \mathbf{r}_N) = \frac{1}{\sqrt{N!}} \begin{vmatrix} \phi_1(\mathbf{r}_1) & \cdots & \phi_N(\mathbf{r}_1) \\ \vdots & \ddots & \vdots \\ \phi_1(\mathbf{r}_N) & \cdots & \phi_N(\mathbf{r}_N) \end{vmatrix} \qquad \textbf{(Eq. III. 6)}$$

This determinant guarantees that the exchange of two rows or columns results in a change of sign in the wave function, thereby upholding the Pauli exclusion principle.

III.5.3 Constructing molecular orbitals: The LCAO approximation

The Linear Combination of Atomic Orbitals (LCAO) approximation is a fundamental theoretical approach used in molecular quantum chemistry to describe molecular orbitals. This method involves expressing the molecular orbitals as a weighted sum of the atomic orbitals associated with the various atoms that comprise the molecule. A key concept underlying the LCAO approximation is the delocalization of electrons within a molecule. Instead of being

confined to individual atomic orbitals localized on specific atoms, the electrons are spread out over the entire molecular structure. This delocalization is crucial for understanding molecular bonding and properties. When atomic orbitals from different atoms interact, they can do so either constructively or destructively. Constructive interference occurs when the wave functions of the atomic orbitals combine in phase, leading to the formation of molecular orbitals that are lower in energy, known as bonding molecular orbitals. Conversely, destructive interference occurs when the wave functions combine out of phase, resulting in higher-energy molecular orbitals termed antibonding molecular orbitals **[17]**.

The LCAO approach thus provides a powerful framework for understanding the electronic structure of molecules, allowing chemists to predict the stability, reactivity, and overall behavior of various chemical species based on the nature of the bonding and antibonding interactions among the contributing atomic orbitals. A molecular orbital, denoted as ψi, is thus articulated as a linear combination of atomic orbitals represented by orbitals χμ:

$$\boldsymbol{\psi_i = \sum_{\mu} c_{\mu i} \chi_{\mu}} \qquad \textbf{(Eq. III. 7)}$$

The coefficients $C_{\mu i}$ represent the linear combinations used in the analysis. These coefficients are obtained by minimizing the total energy of the system.

III.5.4 Roothaan Formulation of the Hartree–Fock Method

The Hartree-Fock equations may be reformulated in matrix form utilizing the Linear Combination of Atomic Orbitals (LCAO) approximation, thereby facilitating numerical solutions. This reformulation is commonly referred to as the Hartree-Fock-Roothaan equations:

$$\boldsymbol{FC = SC\varepsilon} \qquad \textbf{(Eq. III. 8)}$$

In the context of computational chemistry, the orbital energy vector, denoted as ε, plays a vital role in understanding the energy levels of electrons in a molecular system. Each component of this vector corresponds to the energy associated with a particular molecular orbital. The coefficient matrix, referred to as C, consists of linear combinations of atomic orbitals (LCAO) that are used to describe the molecular orbitals as a sum of atomic contributions. The atomic orbital overlap matrix, represented as S, quantifies the extent of overlap between different atomic orbitals, which is essential for determining the interactions between electrons in a molecular framework. Lastly, the Fock matrix, denoted as F, is

constructed to represent the one-electron energy terms, which include kinetic and potential energy contributions, as well as electron-electron interactions in a mean-field approximation. When utilizing computational chemistry software to analyze and model intricate chemical systems, the integration of these elements ε, C, S, and F is crucial for accurately predicting molecular behavior, energy states, and properties, ultimately aiding in the understanding of chemical reactivity and stability [12].

III.5.5 Beyond the Hartree–Fock Approximation

The Hartree-Fock method has proven to be effective for calculating electronic structures and ionization energies. However, it has a significant drawback: it overlooks dynamic electronic correlations. This oversight means that the method does not account for the instantaneous interactions that occur due to coordinated movements of electrons. As a result, the accuracy of the Hartree-Fock method can be limited, particularly in complex systems where these correlations play a crucial role [12].

III.6 Density Functional Theory (DFT)

This theory employs a different approach compared to the Hartree-Fock (SCF) method for calculating the electronic structure of molecules and solids. Density functional theory (DFT) utilizes electron density ρ(r) as the fundamental variable, defining the system based on this consideration. This approach simplifies the problem to n electrons in three-dimensional space, rather than dealing with the 3n-dimensional space of the wave function Ψ. The density of an n-electron system with a wave function Ψ(r_1,r_2, …, r_n) is written as follows:

$$\boldsymbol{\rho(r) = \int [\Psi(r_1, r_2, \dots, r_n)]^2 \, dr_1, r_2, \dots, r_n} \qquad \textbf{(Eq. III. 9)}$$

Where the standard of ρ is n. The two theorems established by Hohenberg and Kohn [18] serve as the foundational principles for Density Functional Theory (DFT) methodologies. The first theorem asserts the existence of a unique electron density ρ that is associated with a given external potential. The second theorem indicates that the variational principle can be effectively applied to the electron density ρ.

- **Theorem 1:** The total electron density at each spatial point, denoted as ρ(r), is the sole variable that determines the ground state of an electronic system subjected to an external potential V, which is generated by the nuclei.

- **Theorem 2:** The minimum value of the functional energy E[ρ] corresponds to the energy of the ground state:

$$\mathbf{E} = \boldsymbol{min}\mathbf{E}[\boldsymbol{\rho}(\mathbf{r})] \qquad \textbf{(Eq. III. 10)}$$

The following theorems apply solely to the static ground state. The expression for the functional energy is provided below, exclusive of spin considerations:

$$\mathbf{E}[\boldsymbol{\rho}] = \mathbf{T}[\boldsymbol{\rho}] + \mathbf{V}_{\boldsymbol{ee}}[\boldsymbol{\rho}] + \int \boldsymbol{\rho}(\mathbf{r})\boldsymbol{V}(\mathbf{r})\mathbf{dr} \qquad \textbf{(Eq. III. 11)}$$

The external potential V refers to the potential generated by the nuclei, while Vee [ρ] represents the electronic interaction energy functional, and T [ρ] denotes the kinetic energy functional. Although Hohenberg and Kohn's theorems confirm the existence of the functional E [ρ], they do not provide an analytical form for it.

The objective is to derive an approximate expression. The functional E[ρ] is affected by the kinetic contribution T0, which corresponds to a non-interacting system of electrons, as well as by the Coulomb contribution from a classical system:

$$\mathbf{E}[\boldsymbol{\rho}] = \mathbf{T_0}[\boldsymbol{\rho}] + \frac{\mathbf{1}}{\mathbf{2}}\iint \frac{\boldsymbol{\rho}(\mathbf{r})\boldsymbol{\rho}(\mathbf{r}')}{|\boldsymbol{r}-\mathbf{r}'|}\boldsymbol{drdr}' + \int \boldsymbol{\rho}(\mathbf{r})\,\boldsymbol{V}(\mathbf{r})\mathbf{dr} + \mathbf{E}_{\boldsymbol{XC}}[\boldsymbol{\rho}] \qquad \textbf{(Eq. III. 12)}$$

The functional E_{XC} [ρ] represents an exchange-correlation functional that effectively integrates both exchange and correlation effects. It also accounts for kinetic contributions associated with electron interactions, providing a comprehensive description of electron behavior in many-body systems.

$$\mathbf{E}_{\boldsymbol{XC}}[\boldsymbol{\rho}] = \mathbf{T}[\boldsymbol{\rho}] - \mathbf{T_0}[\boldsymbol{\rho}] + \mathbf{V}_{\boldsymbol{ee}}[\boldsymbol{\rho}] - \frac{\mathbf{1}}{\mathbf{2}}\iint \frac{\boldsymbol{\rho}(\mathbf{r})\boldsymbol{\rho}(\mathbf{r}')}{|\boldsymbol{r}-\mathbf{r}'|}\boldsymbol{drdr}' \qquad \textbf{(Eq. III. 13)}$$

The variational principle, when combined with the Lagrange multiplier (denoted as λ), yields the following result:

$$\frac{\boldsymbol{\delta}\mathbf{E}[\boldsymbol{\rho}]}{\boldsymbol{\delta}\boldsymbol{\rho}(\mathbf{r})} = \frac{\boldsymbol{\delta}\mathbf{T_0}}{\boldsymbol{\delta}\boldsymbol{\rho}(\mathbf{r})} + \boldsymbol{V}(\mathbf{r}) + \iint \frac{\boldsymbol{\rho}(\mathbf{r}')}{|\boldsymbol{r}-\mathbf{r}'|}\boldsymbol{dr} + \frac{\boldsymbol{\delta}\mathbf{E}_{\boldsymbol{XC}}[\boldsymbol{\rho}]}{\boldsymbol{\delta}\boldsymbol{\rho}(\mathbf{r})} = \boldsymbol{\lambda} \qquad \textbf{(Eq. III. 14)}$$

This equation will be solved using Kohn and Sham's approach **[19].** The following formula describes an electron system without interaction with an external potential V* (r):

$$\frac{\boldsymbol{\delta}\mathbf{E}[\boldsymbol{\rho}]}{\boldsymbol{\delta}\boldsymbol{\rho}(\mathbf{r})} = \frac{\boldsymbol{\delta}\mathbf{T_0}}{\boldsymbol{\delta}\boldsymbol{\rho}(\mathbf{r})} + \boldsymbol{V}^*(\mathbf{r}) = \boldsymbol{\lambda} \qquad \textbf{(Eq. III. 15)}$$

After comparing the two previous equations:

$$\boldsymbol{V^*(\mathbf{r}) = V(\mathbf{r}) + \int \frac{\rho(\mathbf{r}')}{|r - \mathbf{r}'|} dr + \frac{\delta \mathbf{E}_{XC}[\rho]}{\delta \rho(\mathbf{r})}} \qquad \textbf{(Eq. III. 16)}$$

The solution to equation (Eq. III.15) is well-established and corresponds to the density calculated using the orbitals defined by the following equation:

$$\left(-\frac{1}{2}\nabla_i^2 + V^*(\mathbf{r})\right)\Phi_i(r) = \mathcal{E}_i \Phi_i(r) \qquad \textbf{(Eq. III. 17)}$$

$$\rho(\mathbf{r}) = \sum_{i=1}^{n} |\Phi_i(r)|^2 \qquad \textbf{(Eq. III. 18)}$$

The interacting electron system is substituted with a hypothetical non-interacting electron system that evolves within an effective external potential, denoted as V*(r). Consequently, the equation represented in (Eq. III.14) is solved. The structure of the resulting self-consistent equations is akin to that of the Hartree-Fock equations; however, they differ in their incorporation of the total electron density of the system, reflecting the effects of electron interactions. The density ρ(r) is influenced by the Kohn–Sham orbitals, represented as Φ_i, and the respective energy levels $\mathcal{E}_i$.

To conduct Density Functional Theory (DFT) calculations, it is essential to determine the exchange-correlation energy, denoted as E_{XC} [ρ]. This energy can be decomposed into two distinct components: exchange energy and correlation energy.

$$\mathbf{E}_{XC}[\rho] = \mathbf{E}_X^{HF}[\rho] + \mathbf{E}_C[\rho] \qquad \textbf{(Eq. III. 19)}$$

The various types of functionals are well-documented in the existing literature, and ongoing advancements continue to emerge in this field. The primary approximations utilized within Density Functional Theory (DFT) include the Local Density Approximation (LDA) and the Generalized Gradient Approximation (GGA).

III.6.1 Local density approximation (LDA)

When it comes to these functions, the energy contribution is fascinatingly tied to the local density at each specific spot. It's all about how the density at that location shapes the energy dynamics:

$$\mathbf{E}_{XC}^{LDA} = \mathbf{E}_X^{gazuniforme} + \mathbf{E}_X^{locale} \qquad \textbf{(Eq. III. 20)}$$

The exchange energy depends on the density, specifically on $\rho^{(1/3)}$, and bears resemblance to the energy found in a uniform gas of electrons, as proposed by Dirac **[20]**. Local density serves as the sole factor influencing correlation energy. The Vosko, Wilk, and Nusair (VWN) functional is recognized as the most prominent correlation functional in this context **[21]**.

The Local Density Approximation (LDA) functional effectively manages molecular geometries; however, it tends to underestimate the lengths of bonds involved in hydrogen bonding, leading to shorter bond distances than expected. In certain cases, the LDA functional can accurately represent a minimum transition state. Additionally, while the vibrational frequencies predicted by LDA are generally reliable, it is important to note that LDA tends to overestimate bond energies when compared to the Hartree-Fock method **[22]**.

III.6.2 The generalized gradient approximation (GGA)

The properties of generalized gradient approximation (GGA) are influenced by both the electron density and its gradient.

Becke's Be88 **[23]** is recognized as one of the most commonly utilized exchange functions in computational chemistry. For assessing correlation, the LYP **[24]** functional developed by Lee, Yang, and Parr, along with the PW91 **[25]** functional proposed by Perdew and Wang, are frequently employed due to their effectiveness and reliability. The geometries and bond energies resulting from the Generalized Gradient Approximation (GGA) functionality demonstrate greater accuracy in comparison to those obtained through the Local Density Approximation (LDA) functionality. However, the calculation of vibrational frequencies associated with the GGA functionality is less accurate than that of the LDA functionality. It is important to note that surface potential energy barriers are often subject to underestimation **[22]**.

III.6.3 Hybrid Functions

Hybrid functionals integrate a portion of the Hartree-Fock exchange energy along with the exchange energy derived from Density Functional Theory (DFT). This combination aims to enhance the accuracy of calculations in quantum chemistry by leveraging the strengths of both methods.

$$E_{xc}^{hybride} = aE_{HF} + (1-a)E_{DFT} \qquad \textbf{(Eq. III. 21)}$$

The Becke, 3-Parameter, Lee-Yang-Parr (B3LYP) hybrid functional is among the most commonly utilized methods in computational chemistry. Introduced in the 1990s, it was designed to address the shortcomings of traditional density functional theory (DFT) functionals, including the Local Density Approximation (LDA) and Generalized Gradient Approximation (GGA). While DFT exhibited encouraging results, it often fell short in accurately predicting certain spectroscopic properties. The B3LYP functional integrates both Hartree-Fock exchange and DFT exchange-correlation to enhance performance and provide more reliable outcomes in calculations. The expression of exchange-correlation energy in B3LYP is [26]:

$$E_{xc}^{B3LYP} = aE_{HF} + (1-a)E_{DFT} + bE_{corr}^{DFT} \qquad (\text{Eq. III. 22})$$

With:

a=20% Hartree-Fock exchange energy.

(1-a) =80% DFT exchange energy (Becke 88),

B is the DFT correlation energy (Lee-Yang-Parr).

III.7 Basis functions

III.7.1 Fundamental Functions in Quantum Chemistry

Basis functions play a fundamental role in quantum chemistry calculations, as they determine the behavior of atomic and molecular orbitals within intricate electronic systems. The selection of these functions is crucial for effectively modeling electronic interactions while maintaining computational efficiency. In this section, we will examine two primary categories of basis functions: Slater-type orbitals (STO) and Gaussian-type orbitals (GTO). Each of these types has distinct characteristics and applications that contribute to the accuracy and efficiency of quantum chemical computations.

III.7.1.1 Slater Type Functions (STO)

Slater-type functions (STO) were introduced by physicist John C. Slater in the 1930s [27]. Slater aimed to create a function that accurately models the exponential decay characteristic of atomic orbitals, drawing inspiration from the exact solution of Schrödinger's equation about the hydrogen atom. STOs were among the pioneering functions utilized to represent atomic orbitals within the field of quantum chemistry. Their exponential formulation provides a robust approximation of electron density in proximity to the nucleus.

Slater-type orbitals (STOs) are characterized by an exponential decay, which makes them particularly effective for representing the behavior of an electron near the nucleus. Their general expression is given by:

$$\chi_{STO} = N \cdot r^{n-1} e^{-\zeta r} Y_{lm}(\theta, \phi) \qquad \textbf{(Eq. III. 23)}$$

Where:

- N is a normalization factor;
- r is the distance between the electron and the nucleus;
- n is a positive integer that defines the orbital;
- ζ (zeta) is an adjustment parameter that regulates the decay;
- Y_{lm} is the spherical harmonic, defining the angular dependence.

This exponential representation provides an approximation of the true electron density in regions proximal to the nucleus, which is crucial for calculations that demand a high level of accuracy.

Initially, Slater-Type Orbitals (STOs) were employed in ab initio calculations for simple systems. However, the integrals associated with STOs are inherently complex and challenging to solve analytically, which restricts their use to smaller-scale calculations. Semi-empirical methods, such as approximate Hartree-Fock approaches, often utilize STOs for light atomic systems because they provide a reasonably accurate portrayal of orbitals with manageable complexity in small systems. This makes STOs particularly effective for modeling core electrons. Nonetheless, the intricate nature of integral calculations tied to their exponential form limits their viability in larger-scale computations. As a result, STOs have gradually been supplanted by Gaussian-Type Orbitals (GTOs) in most modern computational chemistry applications.

III.7.1.2 Gaussian Type Functions (GTO)

Gaussian-type functions (GTFs) were introduced by chemist S. F. Boys in the 1950s as an alternative to Slater-type orbitals (STOs) to address computational limitations. GTFs simplify integral calculations by utilizing Gaussian decay, which replaces the exponential decay characteristic of STOs [28]. GTOs have become widely adopted for electronic structure calculations, particularly in large molecules and complex systems. They take the following form:

$$\chi_{GTO} = N \cdot x^a y^b z^c e^{-\alpha r^2} \quad \textbf{(Eq. III. 24)}$$

Where:

- N is a normalization factor;
- x, y, and z represent the coordinates of the electron relative to the nucleus;
- a, b, and c are exponents that define the atomic orbital (e.g., for a p orbital, a=1 and b=c=0);
- α is a decay parameter that adjusts the shape of the Gaussian.

In contrast to Slater-type orbitals (STOs), Gaussian-type orbitals (GTOs) exhibit a slower decrease in amplitude with distance from the nucleus due to their quadratic decay. This characteristic, while contributing to decreased accuracy in regions proximal to the nucleus, facilitates simplified integrated calculations and enables the analysis of larger systems efficiently. Essentially, GTOs facilitate rapid computational processes. However, their quadratic nature constrains their capacity to accurately depict orbitals in the nuclear vicinity, often necessitating the incorporation of multiple Gaussian functions for each atomic orbital to achieve a more precise representation of electron density.

To address the limitations in precision of pure Gaussian-type orbitals (GTOs), researchers have developed combinations known as "linear combinations of primitive Gaussians." A prime example is the STO-3G basis, where three Gaussian functions are combined to effectively approximate a Slater-type orbital (STO). This approach enables a more accurate modeling of atomic orbitals while avoiding the high computational costs typically associated with STOs **[29]**.

Bases such as STO-3G, 6-31G, and 6-311G have been developed to enhance the accuracy of Gaussian-type orbitals (GTOs) while allowing for efficient calculations. These Gaussian bases are designed to differentiate between core and valence orbitals, which improves flexibility and accuracy in areas where valence electrons interact in complex manners.

III.7.1.3 Basic Split-Valence Functions

Split-valence basis sets, particularly 6-31G and 6-311G, were developed to enhance the representation of valence orbitals. Created by John A. Pople and his collaborators, these basis sets are widely recognized for their adaptability and precision in calculations involving medium-sized molecules.

In split-valence basis sets, core and valence orbitals are handled separately to enhance the precision of calculations. Core orbitals utilize a fixed number of Gaussian functions—such as six in the 6-311G basis set—while valence orbitals are organized into multiple groups of functions. This distinction allows for a more detailed representation of the electrons that participate in chemical bonding, leading to more accurate computational results.

In the 6-311G basis set, the notation "6" signifies the use of six Gaussian functions to represent the core orbitals. The "311" part refers to the valence electrons, which are modeled with three different sets of Gaussian functions: three functions for the first valence sublayer, one for the second sublayer, and one for the third. This arrangement is referred to as "triple zeta," and it provides enhanced flexibility in accurately describing the valence region of a molecule.

III.7.1.3.1 Diffuse Functions

6-311+G: The designation “+” signifies the incorporation of diffuse functions specifically applied to non-hydrogen atoms within the computational model. Diffuse functions serve a critical role in enhancing the simulation of electron distribution, particularly for those electrons that are situated at considerable distances from the atomic nucleus. This capability is especially advantageous when analyzing anions, which carry a negative charge, as well as polarizable molecules that can easily adapt their electron clouds in response to external electric fields. Furthermore, the inclusion of these functions is significant for accurately representing weak interactions, such as Van der Waals forces, that arise due to transient dipoles and other non-covalent interactions in molecular systems.

The notation "6-311++G" reflects a sophisticated level of computational chemistry methodology. The "++" signifies that diffuse functions are incorporated for both heavy atoms and hydrogen atoms within the molecular model. This enhancement is crucial, as it enables a more precise representation of electronic interactions, particularly in scenarios where electrons from lighter atoms engage at extended distances from their respective nuclei. Such an approach is vital for studying intricate phenomena, including hydrogen bonding and the behavior of anionic systems, where long-range electron correlation plays a significant role. This added complexity ultimately leads to improved accuracy in the prediction and understanding of molecular behaviors and interactions [29].

III.7.1.3.2 Polarization Functions

The use of asterisks “*” and “**” indicates the inclusion of polarization functions in atomic orbital calculations. These polarization functions represent additional orbitals—specifically, p-type orbitals for hydrogen and d-type orbitals for heavier atoms. Their primary

purpose is to accurately model how electron density shifts in response to external electric fields or internal disturbances, such as the interactions that occur during chemical bonding. Incorporating polarization functions is crucial for calculations that involve excited states or phase transitions, as they provide a more detailed and realistic representation of electron behavior in various physical and chemical environments **[30]**.

Thus, for 6-311++G** or 6-311++G (d,p)

- 6-311G: The basis uses a triple zeta for valence electrons without polarization or diffuse functions.
- 6-311+G: Includes a diffuse function on non-hydrogen atoms.
- 6-311++G: Adds a diffuse function on hydrogen atoms as well.
- 6-311++G*: Includes polarization functions on heavy atoms (p-type orbitals).
- 6-311++G**: Adds polarization functions for hydrogen atoms (d-type orbitals).

Bibliographical references

[1] Méthodes de la chimie quantique, Techniques de l'Ingénieur. (n.d.). https://www.techniques-ingenieur.fr/base-documentaire/sciences-fondamentales-th8/fondamentaux-en-chimie-42106210/methodes-de-la-chimie-quantique-af6050/ (accessed October 8, 2023).

[2] V. Sahni, Generalization of the Schrödinger Theory of Electrons, in: 2022: pp. 49–92. https://doi.org/10.1007/978-3-030-97409-1_3.

[3] P. Hiberty, N.T. Anh, Introduction à la chimie quantique, Editions Ecole Polytechnique, 2008.

[4] G. Ludwig, Foundations of Quantum Mechanics I, Springer Science & Business Media, 2012.

[5] T. Norsen, Foundations of Quantum Mechanics, Springer International Publishing, Cham, 2017. https://doi.org/10.1007/978-3-319-65867-4.

[6] E. Adlam, Foundations of Quantum Mechanics, 1st ed., Cambridge University Press, 2021. https://doi.org/10.1017/9781108885515.

[7] E. Schrödinger, Quantisierung als Eigenwertproblem, Ann. Phys. 384 (1926) 361–376. https://doi.org/10.1002/andp.19263840404.

[8] L. Eisenbud, The Conceptual Foundations of Quantum Mechanics, American Mathematical Soc., 2007.

[9] A. Blais, M ´ ecanique quantique II PHQ-430, (2014).

[10] K. JASMINE, Quantum Chemis, 2014.

[11] Équation de Schrödinger dans le cas d'une molécule, Techniques de l'Ingénieur. (n.d.). https://www.techniques-ingenieur.fr/base-documentaire/archives-th12/archives-physique-chimie-tiafp/archive-1/methodes-de-la-chimie-quantique-af6050/equation-de-schrodinger-dans-le-cas-d-une-molecule-af6050niv10002.html (accessed October 8, 2023).

[12] F. Jensen, Introduction to Computational Chemistry, 2007. https://doi.org/10.1007/s00214-013-1372-6.

[13] V. Fock, Näherungsmethode zur Lösung des quantenmechanischen Mehrkörperproblems, Z. Physik. 61 (1930) 126–148. https://doi.org/10.1007/BF01340294.

[14] D.R. Hartree, The Wave Mechanics of an Atom with a Non-Coulomb Central Field. Part I. Theory and Methods, Math. Proc. Camb. Phil. Soc. 24 (1928) 89–110. https://doi.org/10.1017/S0305004100011919.
[15] J.C. Slater, Cohesion in Monovalent Metals, Phys. Rev. 35 (1930) 509–529.

https://doi.org/10.1103/PhysRev.35.509.
[16] J.C. Slater, Statistical Exchange-Correlation in the Self-Consistent Field, in: P.-O. Löwdin (Ed.), Advances in Quantum Chemistry, Academic Press, 1972: pp. 1–92. https://doi.org/10.1016/S0065-3276(08)60541-9.
[17] Roothaan CCJ. New Developments in Molecular Orbital Theory. Rev. Mod. Phys. 1951; 23: 69-89. Doi: 10.1103/RevModPhys.23.69.
[18] P. Hohenberg, W. Kohn, Inhomogeneous Electron Gas, Phys. Rev. 136 (1964) B864–B871. https://doi.org/10.1103/PhysRev.136.B864.
[19] W. Kohn, L.J. Sham, Self-Consistent Equations Including Exchange and Correlation Effects, Phys. Rev. 140 (1965) A1133–A1138. https://doi.org/10.1103/PhysRev.140.A1133.
[20] P. a. M. Dirac, Note on Exchange Phenomena in the Thomas Atom, Mathematical Proceedings of the Cambridge Philosophical Society. 26 (1930) 376–385. https://doi.org/10.1017/S0305004100016108.
[21] S.H. Vosko, L. Wilk, M. Nusair, Accurate spin-dependent electron liquid correlation energies for local spin density calculations: a critical analysis, Can. J. Phys. 58 (1980) 1200–1211. https://doi.org/10.1139/p80-159.
[22] H. Chermette, Density functional theory: A powerful tool for theoretical studies in coordination chemistry, Coordination Chemistry Reviews. 178–180 (1998) 699–721. https://doi.org/10.1016/S0010-8545(98)00179-9.
[23] A.D. Becke, Density-functional exchange-energy approximation with correct asymptotic behavior, Phys. Rev. A. 38 (1988) 3098–3100. https://doi.org/10.1103/PhysRevA.38.3098.
[24] C. Lee, W. Yang, R.G. Parr, Development of the Colle-Salvetti correlation-energy formula into a functional of the electron density, Phys. Rev. B. 37 (1988) 785–789. https://doi.org/10.1103/PhysRevB.37.785.
[25] J.P. Perdew, Density-functional approximation for the correlation energy of the inhomogeneous electron gas, Phys. Rev. B. 33 (1986) 8822–8824. https://doi.org/10.1103/PhysRevB.33.8822.
[26] M. Reiher, Theoretical Study of the Fe(phen) 2 (NCS) 2 Spin-Crossover Complex with Reparametrized Density Functionals, Inorg. Chem. 41 (2002) 6928–6935. https://doi.org/10.1021/ic0258911.

[27] J.C. Slater, Atomic Shielding Constants, Phys. Rev. 36 (1930) 57–64. https://doi.org/10.1103/PhysRev.36.57.
[28] S. F. Boys, Electronic wave functions - I. A general method of calculation for the stationary states of any molecular system, Proc. R. Soc. London. Ser. A. Math. Phys. Sci. 200 (1950) 542–554. https://doi.org/10.1098/rspa.1950.0036.

[29] R. Ditchfield, W.J. Hehre, J.A. Pople, Self-Consistent Molecular-Orbital Methods. IX. An Extended Gaussian-Type Basis for Molecular-Orbital Studies of Organic Molecules, J. Chem. Phys. 54 (1971) 724–728. https://doi.org/10.1063/1.1674902.

[30] W.J. Hehre, R. Ditchfield, J.A. Pople, Self—Consistent Molecular Orbital Methods. XII. Further Extensions of Gaussian—Type Basis Sets for Use in Molecular Orbital Studies of Organic Molecules, J. Chem. Phys. 56 (1972) 2257–2261. https://doi.org/10.1063/1.1677527.

CHAPTER IV

Structural, Electron Density and Quantum Chemical Investigations of FHP

IV.1 Introduction....62
IV.2 Structural characterization and electron density analysis....63
IV.2.1 Synthesis and Structural Description of FHP....63
IV.2.2 Geometry Optimization....66
IV.2.3 Electron Density and AIM Topological Analysis....69
IV.2.3.1 Experimental Electron Density Distribution....70
IV.2.4 QTAIM Topological Analysis of Bonding Interactions....72
IV.3 Electronic and intermolecular property analysis....76
IV.3.1 Frontier Molecular Orbitals and Global Reactivity Descriptors....76
IV.3.2 Molecular Electrostatic Potential and Hirshfeld Surface Analysis....79
IV.3.2.1 Molecular Electrostatic Potential....80
IV.3.2.2 Hirshfeld Surface Analysis and Two-Dimensional Fingerprint Plots....81
IV.3.3 Reduced Density Gradient (RDG) Analysis and Non-Covalent Interaction Mapping....84
IV.3.4 Electron Localization Function (ELF) and Localized Orbital Locator (LOL) Analysis ..86
Bibliographic references....90

IV.1 Introduction

The development of organic functional materials possessing extended π-conjugated systems has attracted considerable interest because of their remarkable structural, electronic, and optoelectronic properties. Among these materials, Schiff base derivatives and hydrazone compounds constitute an important class of organic molecules owing to their structural flexibility, strong intramolecular charge transfer, coordination ability, and nonlinear optical behavior [1,3]. These compounds are widely investigated for applications in molecular electronics, optical devices, photovoltaics, sensing, and coordination chemistry.

The title compound, *(E)-3-(1-(2-(9H-fluoren-9-ylidene)hydrazineyl)ethylidene)-6-methyl-2H-pyran-2,4(3H)-dione* (FHP), represents a conjugated zwitterionic Schiff base containing electron donor and electron acceptor groups linked through a hydrazone bridge. The coexistence of aromatic rings, heteroatoms, and conjugated π-electron pathways promotes efficient electron delocalization and intramolecular charge transfer processes, making the compound particularly suitable for theoretical and electron density investigations [4].

In recent years, the combination of experimental charge density analysis and Density Functional Theory (DFT) calculations has become an efficient strategy for understanding the relationship between molecular structure and electronic properties. High-resolution X-ray diffraction combined with multipolar refinement methods provides accurate information about electron density distribution, chemical bonding, and intermolecular interactions [5]. In this context, the Hansen–Coppens multipolar formalism implemented in the MoPro software package allows the modeling of aspherical electron density distributions beyond the independent atom approximation [6].

Moreover, the Quantum Theory of Atoms in Molecules (QTAIM), introduced by Bader [7], constitutes a powerful topological tool for analyzing the nature of chemical bonds and intermolecular interactions through the investigation of bond critical points, Laplacian distributions, and electron density topology.

In parallel, DFT calculations were employed to investigate the optimized geometry, frontier molecular orbitals, global chemical reactivity descriptors, molecular electrostatic potential, reduced density gradient, electron localization function, and localized orbital locator of the investigated compound. These complementary approaches provide a deeper

understanding of the electronic structure, charge transfer properties, and non-covalent interactions governing the physicochemical behavior of FHP.

The main objective of this chapter is therefore to correlate the molecular structure, electron density distribution, topological characteristics, and theoretical electronic properties of the synthesized hydrazone derivative.

IV.2 Structural characterization and electron density analysis

IV.2.1 Synthesis and Structural Description of FHP

The hydrazone derivative FHP, (E)-3-(1-(2-(9H-fluoren-9-ylidene)hydrazineyl)ethylidene)-6-methyl-2H-pyran-2,4(3H)-dione, was synthesized through a condensation reaction between (9H-fluoren-9-ylidene)hydrazine and 3-acetyl-4-hydroxy-6-methyl-2H-pyran-2-one (dehydroacetic acid) in ethanol under reflux conditions for one hour (**Figure IV.1**) **[8]**. The reaction proceeds via nucleophilic addition of the hydrazine amino group onto the carbonyl function of the pyranone ring, followed by dehydration and tautomerization, leading to the formation of the hydrazone Schiff base product. The mixture volume was subsequently reduced under vacuum until precipitation occurred, and the product was filtered, washed with water, and purified by recrystallization from EtOH/H_2O to yield diffraction-quality yellow crystals with high purity and stability **[8]**.

The synthetic pathway initially produces the enol form of the compound; however, structural analysis demonstrated that the final isolated product exists preferentially in the keto-hydrazone zwitterionic form. This transformation occurs through intramolecular proton transfer from the hydroxyl oxygen atom of the enol form toward the azomethine nitrogen atom, generating an iminium-enolate structure. The resulting zwitterionic form is stabilized by a strong intramolecular N–H···O hydrogen bond of the N^+–H···O^- type, as previously established by Guerraoui et al. **[9]** and confirmed in the present work through multipolar electron density analysis. While conventional techniques such as FT-IR and ^{1}H NMR spectroscopy were employed in the original structural report to confirm functional groups and solution-state behavior [9], the present work adopts a more rigorous and quantitative solid-state approach, providing a direct experimental description of chemical bonding in the crystalline state at the electron density level.

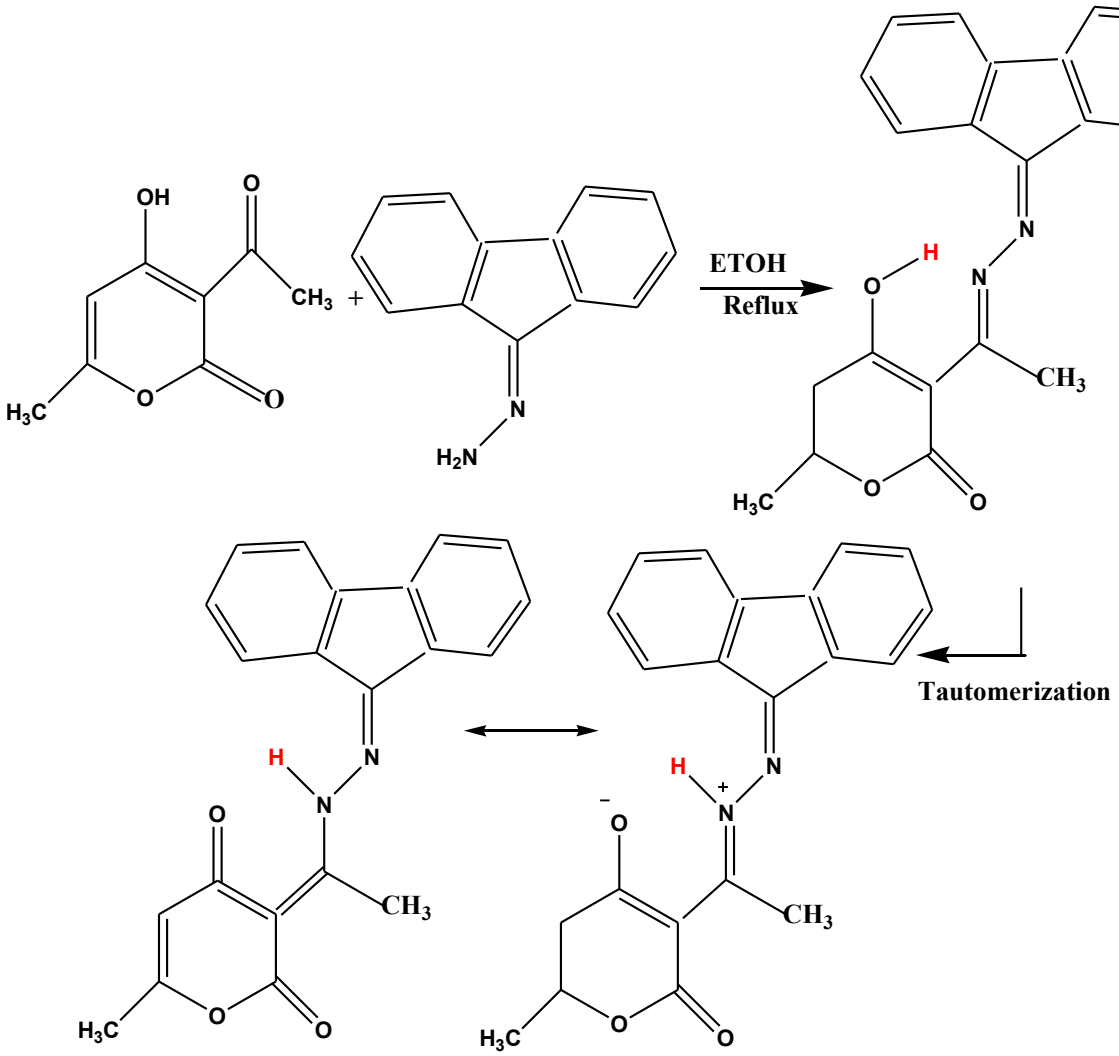


Figure IV.1. Synthesis of pyran-2,4-dione derivative.

Single-crystal X-ray diffraction analysis confirmed that FHP crystallizes in the monoclinic crystal system with the $P2_1/c$ space group (**Table IV.1**), with the molecular geometry adopting the E-configuration around the azomethine C=N linkage [13]. The crystal packing is stabilized through a network of intermolecular interactions, including C–H···O hydrogen bonds, C–H···π contacts, and π···π stacking interactions, forming a three-dimensional supramolecular framework.

Table IV.1. Crystal structure refinement details of the synthesized compound.	
Empirical formula	$C_{21}H_{16}N_2O_3$
Formula weight, g/mol	344.36
CCDC	2004993
Crystal color	Yellow
Space group	$P2_1/c$
Crystal system	Monoclinic
F (000)	552
a (Å)	11.976 (2)
b (Å)	5.0343 (17)
c (Å)	26.710 (7)
ß (°)	98.06 (2)
V (Å³)	1594.4 (7)
Z	4
Temperature/K	100
Radiation	Mo Kα (λ = 0.71073)
Dcalcd (g/cm³)	1.410
μ (mm^{-1})	0.10
Crystal size (mm)	0.62 × 0.06 × 0.04
Tmin, Tmax	0.548, 1.000
R [$F^2 > 2\sigma(F^2)$]	0.080
wR (F^2)	0.226
Rint	0.162
Δρmax, Δρmin(e/Å³)	0.41, −0.34

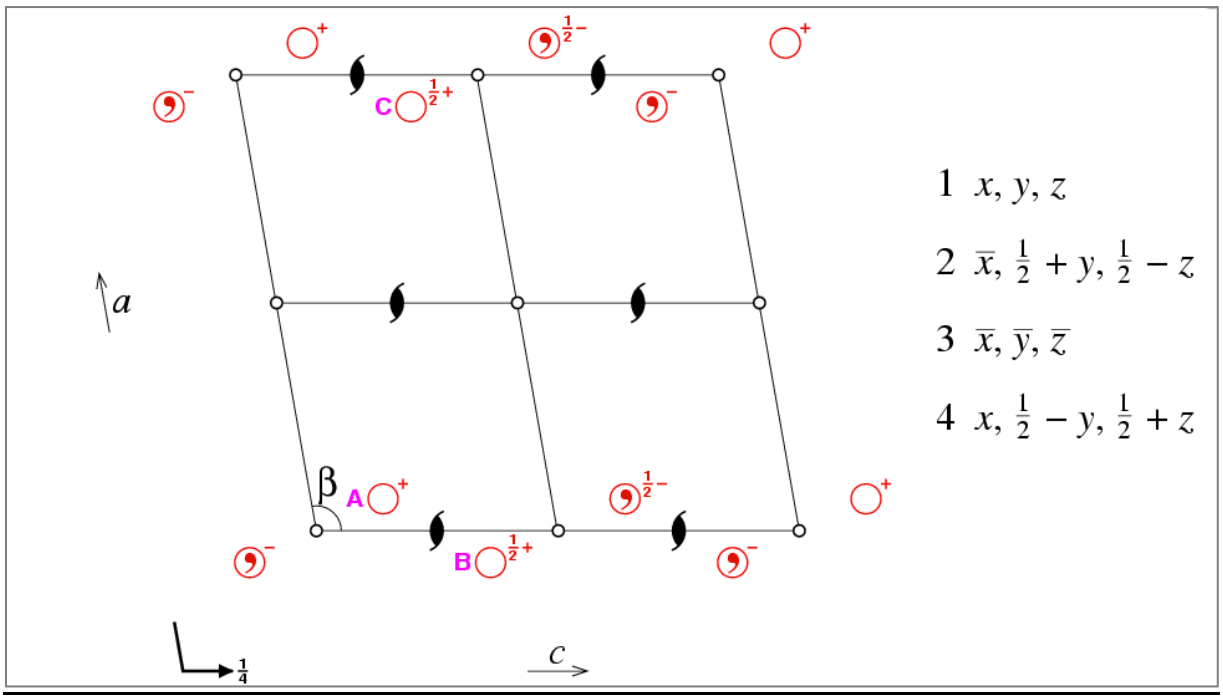


Figure IV.2. Space group presentation $P2_1/c$ of the monoclinic system

While conventional characterization techniques such as FT-IR and ^{1}H NMR spectroscopy were employed in the original structural report to confirm the functional groups and solution-state behavior of the compound **[8]**, the present work goes further by adopting a rigorous quantitative solid-state approach. The nature and strength of the chemical bonds in FHP were therefore investigated through multipolar electron density refinement using the MoPro software package, based on the Hansen–Coppens formalism. This approach provides a direct experimental characterization of each bonding interaction at the level of the electron density distribution, allowing the unambiguous determination of bond nature — covalent, polar, or closed-shell — through the topological analysis of the electron density within the QTAIM framework, as detailed in the following sections.

IV.2.2 Geometry Optimization

The molecular structure of the hydrazone derivative, *(E)*-3-(1-(2-(9H-fluoren-9-ylidene)hydrazineyl)ethylidene)-6-methyl-2H-pyran-2,4(3H)-dione (FHP), was determined by single-crystal X-ray diffraction analysis. **Figure IV.3** presents the molecular structure of FHP together with the crystal packing view, illustrating the orientation of the fused aromatic rings, the conformation adopted by the hydrazone linkage, and the spatial arrangement of the substituents within the molecule. The compound crystallizes in the monoclinic crystal system with the $P2_1/c$ space group, and the resulting unit cell and crystal packing are shown in **Figure IV.4**. Within this arrangement, the molecules are organized into a well-defined supramolecular network in which adjacent units are connected through directional intermolecular contacts. The molecular framework is stabilized by the extended conjugation of the fluorenylidene moiety with the hydrazone and pyran-dione units. The presence of heteroatoms such as nitrogen and oxygen gives rise to a rich network of intra- and intermolecular hydrogen bonds and dipole–dipole interactions, which contribute substantially to the stability and regularity of the crystal packing. It is worth noting that the crystal structure of FHP was first reported by Guerraoui et al. **[9]**, and the present work builds upon that structural determination.

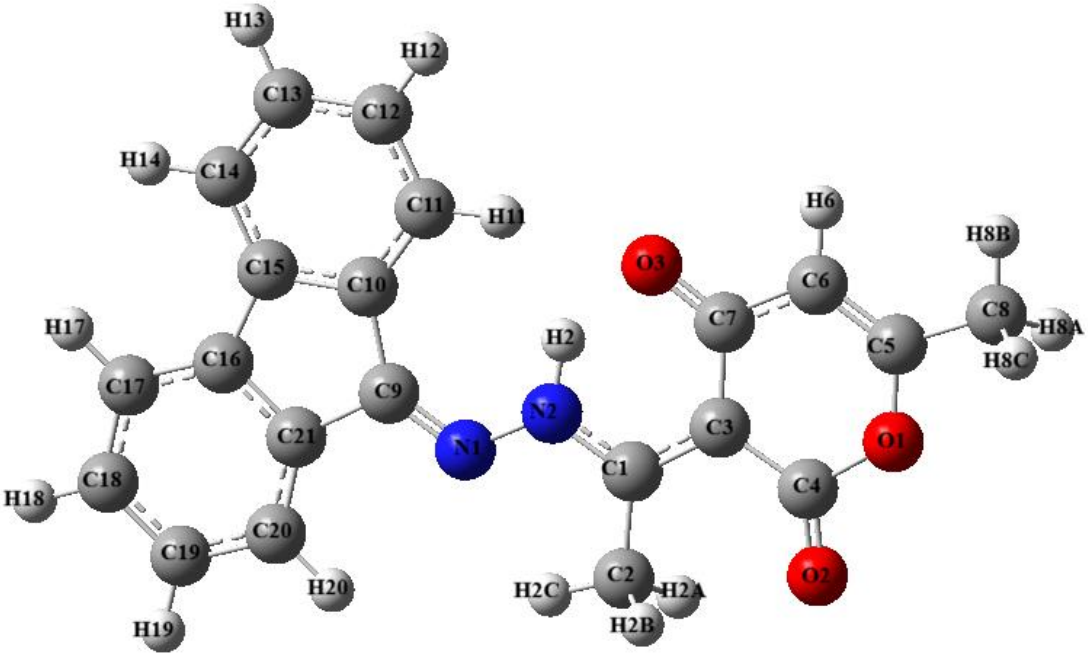


Figure IV.3. Molecular structure of FHP

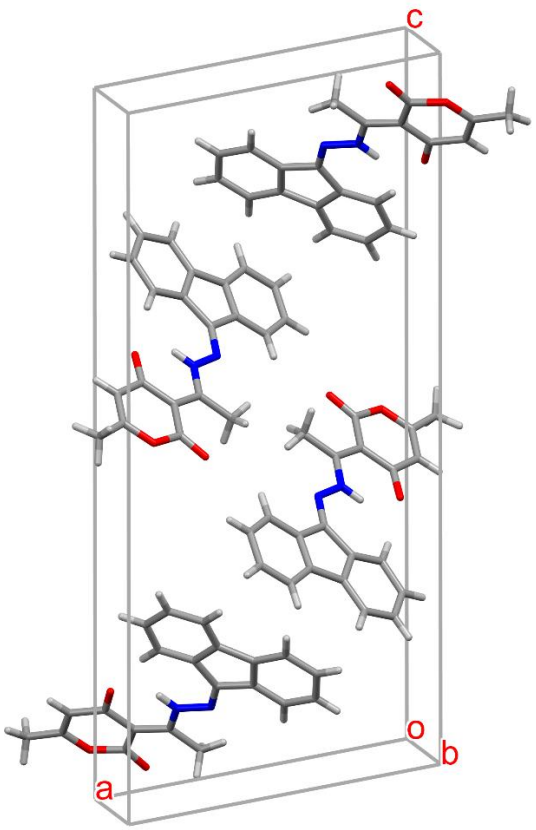


Figure IV.4. Perspective view of the crystal packing for FHP

The molecular geometry of FHP was further investigated through Density Functional Theory (DFT) calculations performed at the B3LYP/6-311G(d,p) level of theory, with solvent effects accounted for using the Polarizable Continuum Model (PCM) with dimethyl sulfoxide (DMSO) as the solvent medium. The optimized geometry obtained in the present work shows excellent agreement with the experimental crystallographic parameters, as summarized in **Table IV.2**, where the calculated bond lengths and bond angles are compared directly with the experimental X-ray values. This consistency confirms the reliability of the selected computational methodology for describing the ground-state geometry of FHP. These findings are further supported by the results of Guerraoui et al. **[9]**, who reported similar agreement using the B3LYP/6-311++G(d,p) basis set, reinforcing the robustness of the DFT description across different basis set choices.

Table IV.2. Selected DFT/XRD bond angles and bond lengths.

Distance bond	Bond length [Å]		Angle Bond	Angle value (°)	
	XRD	DFT		XRD	DFT
O3 C7	1.262	1.279	C5 O1 C4	122.8	122.3
O1 C5	1.355	1.376	N2 N4 C9	118.6	119.5
O1 C4	1.404	1.440	N4 N2 C1	120.8	120.6
O2 C4	1.210	1.226	N4 C9 C21	118.0	118.4
N4 N2	1.376	1.395	N4 C9 C10	135.9	135.6
N4 C9	1.290	1.297	C21 C9 C10	106.1	105.9
N2 C1	1.340	1.347	C21 C16 C15	108.6	108.0
C9 C21	1.479	1.486	C21 C16 C17	120.3	120.2
C9 C10	1.495	1.495	C15 C16 C17	131.1	131.8
C16 C21	1.395	1.410	O3 C7 C3	122.9	122.9
C16 C15	1.471	1.477	O3 C7 C6	119.8	120.2
C16 C17	1.381	1.391	C3 C7 C6	117.3	117.0
C7 C3	1.440	1.459	C9 C21 C16	109.2	109.3
C7 C6	1.431	1.446	C9 C21 C20	129.2	129.3
C21 C20	1.377	1.388	C16 C21 C20	121.6	121.4
C3 C1	1.415	1.415	C7 C3 C1	121.1	120.2
C3 C4	1.453	1.449	C7 C3 C4	119.3	121.1
C2 C1	1.498	1.505	C1 C3 C4	119.6	118.7
C10 C15	1.426	1.427	N2 C1 C3	117.9	118.0
C10 C11	1.385	1.396	N2 C1 C2	117.7	118.9
C15 C14	1.377	1.388	C3 C1 C2	124.4	123.1
C5 C6	1.335	1.345	C9 C10 C15	107.2	107.7
C5 C8	1.472	1.498	C9 C10 C11	133.2	132.8
C20 C19	1.384	1.400	C15 C10 C11	119.6	119.5
C12 C11	1.392	1.403	C16 C15 C10	108.8	109.1
C12 C13	1.385	1.395	C16 C15 C14	130.6	129.8
C14 C13	1.383	1.401	C10 C15 C14	120.6	121.1
C17 C18	1.389	1.402	O1 C5 C6	121.2	122.2
C19 C18	1.392	1.400	O1 C5 C8	112.9	112.1

The optimized structure preserves the molecular planarity around the hydrazone bridge, favoring conjugation and electronic delocalization. The strong intramolecular N–H···O hydrogen bond remains conserved after optimization, demonstrating its important role in stabilizing the zwitterionic form of the molecule.

The conjugated molecular framework formed by the fluorenyl ring system and pyran-dione fragment facilitates electron migration across the molecule, which is essential for charge-transfer processes and nonlinear optical properties.

IV.2.3 Electron Density and AIM Topological Analysis

The characterization of chemical bonding in molecular crystals has undergone a profound transformation with the advent of high-resolution X-ray diffraction techniques combined with rigorous mathematical formalisms for electron density modelling. In this context, electron density (ED) analysis and the Quantum Theory of Atoms in Molecules (QTAIM) represent two deeply interconnected and complementary approaches that together provide an exhaustive description of the electronic structure of a compound in its crystalline environment.

The electron density distribution, obtained experimentally through multipolar refinement of high-resolution X-ray diffraction data using the Hansen–Coppens formalism, constitutes the fundamental quantity from which all bonding information is extracted. It encodes, in a continuous and observable scalar field defined at every point in real space, the complete electronic structure of the molecule, including the nature, polarity, and strength of each chemical bond, the localization of lone pairs, and the extent of electron delocalization across conjugated frameworks.

QTAIM, introduced by Bader **[7]**, provides the rigorous theoretical framework through which this electron density field is interpreted in terms of chemical bonding. By analyzing the topology of $\rho(r)$ its critical points, gradient paths, and associated curvature properties **[10]**, QTAIM establishes a partition of molecular space into atomic basins and identifies bond critical points (BCPs) as the unambiguous signature of bonding interactions. The values of the electron density $\rho(r)$ and its Laplacian $\nabla^2\rho(r)$ evaluated at BCPs serve as quantitative descriptors that distinguish between shared covalent interactions, polar bonds, and closed-shell noncovalent contacts **[11]**.

In the present work, the electron density of FHP was derived from multipolar refinement using the MoPro software package, and the resulting density was subjected to a full QTAIM topological analysis. The following sections present, first, the experimental electron density distribution visualized through deformation density maps, and second, the complete topological characterization of all bonding interactions identified in the structure.

IV.2.3.1 Experimental Electron Density Distribution

Significant advances over recent decades in cryogenic X-ray diffraction techniques have enabled the accurate experimental reconstruction of charge density distributions in molecular solids, particularly in systems composed of light atoms, with results that show remarkable agreement with those obtained from high-level theoretical calculations [12]. The following relation expresses the electron density as a function of the structure factor:

$$\boldsymbol{\rho}(\mathbf{r}) = \frac{\mathbf{1}}{\boldsymbol{V}} \sum_{\boldsymbol{hkl}} \boldsymbol{F_{hkl}} \cdot \boldsymbol{e}^{-2\pi i \mathbf{h}\cdot\mathbf{r}} \qquad \textbf{(Eq IV. 1)}$$

where F_{hkl}, the structure factor of the hkl reflection, and V is the volume of the unit cell. The Hansen–Coppens multipolar model provides a particularly powerful framework for analysing experimental electron density, as it goes beyond the independent atom model by accounting explicitly for the asphericity of valence electron distributions. In this formalism, the electron density around each atom is expanded into multipolar components: monopoles, dipoles, quadrupoles, and octupoles, allowing a precise and physically meaningful representation of the true charge distribution in the crystalline environment **[12,14]**. The multipolar model is expressed as:

$$\boldsymbol{\rho_{atom}}(\mathbf{r}) = \boldsymbol{\rho_{core}}(\boldsymbol{r}) + \boldsymbol{P_\kappa \kappa^3 \rho_{val}}(\boldsymbol{\kappa r}) + \sum_{\boldsymbol{l=0}}^{\boldsymbol{l_{max}}} \boldsymbol{\kappa'^3}\, \boldsymbol{R_l}(\boldsymbol{\kappa' r}) \sum_{\boldsymbol{m=0}}^{\boldsymbol{l}} \boldsymbol{P_{lm\pm}}\, \boldsymbol{d_{lm\pm}}(\boldsymbol{\theta}, \boldsymbol{\phi}) \quad \textbf{(Eq. IV. 2)}$$

Where ρ_{core} and ρ_{val} are the spherically averaged Hartree–Fock core and valence densities, respectively, with ρ_{val} normalized to one electron. The Slater-type radial functions R_l are given by:

$$\boldsymbol{R_l}(\boldsymbol{r}) = \frac{\boldsymbol{\zeta}^{\boldsymbol{n_l+3}}}{(\boldsymbol{n_l+2})!} \boldsymbol{r}^{\boldsymbol{n_l}} \boldsymbol{e}^{-\boldsymbol{\zeta r}} \qquad \textbf{(Eq. IV.3)}$$

Where the normalization factor and the par, and ζ are selected following the guidelines proposed by Coppens [12]. During the refiement, the poulation arameters P_κ and P_{lm}, together with the radial expansion–contraction parameters κ and κ', are refined simultaneously. The non-

spherical electron density was modelled up to the octupole level (l = 3) for C, N, and O atoms, while for H atoms the refinement was limited to the dipole level (l = 1), with cylindrical symmetry imposed along the H–heavy atom bond direction **[15]**.

The electron density (ED) distribution of FHP was analyzed through high-resolution 2D and 3D static deformation density maps derived from the multipolar refinement, as shown in **Figure IV.5**. The 2D deformation map, displayed with a contour interval of 0.05 e·Å^{-3}, provides a clear visualization of the redistribution of valence electron density with respect to the promolecule reference. Positive contours, indicating charge accumulation, are observed along all bonding paths throughout the molecular framework, encompassing both nonpolar C–C interactions within the fluorenyl aromatic system and polar C–O and C–N bonds of the hydrazone and pyran-dione units. This charge accumulation in internuclear regions is the hallmark of covalent bonding and confirms the effectiveness of the multipolar refinement in capturing the true valence electron distribution.

Notably, the atomic nuclear positions are devoid of significant electron density maxima, particularly for non-hydrogen atoms, in full agreement with theoretical predictions and consistent with the deformation density concept, which by construction removes the spherical atomic contribution and reveals only the chemically meaningful valence redistribution.

The deformation maps also provide direct evidence of lone pair localisation. The non-bonding electron density around the oxygen atoms O2 and O3 appears as well-resolved off-nuclear maxima, indicating the presence of spatially localized lone pairs oriented in directions consistent with their expected hybridization. Similarly, the imine functional group C(9)=N(1)–N(2) exhibits a distinct lone pair density peak on N(1), with symmetrical charge distribution along the N=C and N–N bonds, a feature previously observed in analogous hydrazone and Schiff base systems.

The 3D deformation density representation further confirms these observations, revealing continuous ridges of electron density accumulation along all chemical bonds, with a complete absence of density maxima at nuclear positions reflecting the expected electron depletion at nuclear sites due to valence shell bonding interactions. This pattern is fully consistent with the interpretation of bonding as directional electron-sharing interactions, in agreement with QTAIM theory. Furthermore, in the region of the intramolecular N–H···O hydrogen bond, a charge deficiency is observed between the donor and acceptor atoms, indicative of the partially electrostatic nature of this interaction, consistent with the findings of

Espinosa et al. [16-17], who associated reduced electron density in such regions with closed-shell noncovalent character.

Overall, the 2D and 3D deformation density maps **Figure IV.5.** confirm the physical soundness of the multipolar model and provide the experimental electron density field upon which the full QTAIM topological analysis presented in the following section is based.

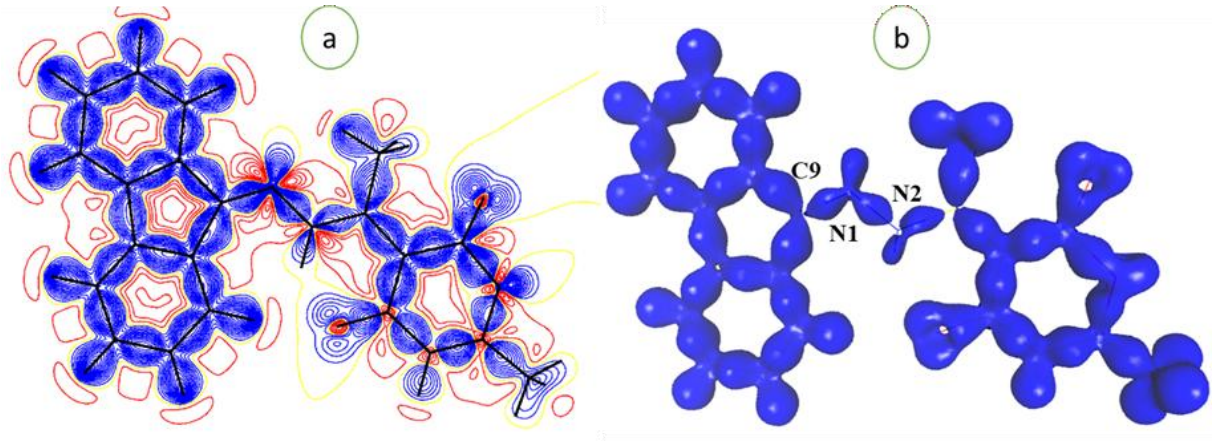


Figure IV.5. Electron density maps for FHP, (a) 2D-ED with a contour of 0.05 e.Å^3, and (b) 3D-ED.

IV.2.4 QTAIM Topological Analysis of Bonding Interactions

The quantum theory of atoms in molecules, developed by Bader, establishes a rigorous and unambiguous framework for the analysis of chemical bonding through the topology of the electron density scalar field ρ(r) [18]. Within this formalism, bonding interactions are identified and characterized through the properties of critical points in space where the gradient of the electron density vanishes, $\nabla\rho(r) = 0$. Among these, bond critical points (BCPs), classified by the topological index (3, –1), are of particular chemical relevance, as each BCP located between two nuclei constitutes a necessary and sufficient condition for the existence of a bonding interaction between them.

At each BCP, a set of topological descriptors is evaluated to characterize the nature and strength of the interaction. The electron density $\rho(r)_{BCP}$ reflects the accumulation of charge in the internuclear region and serves as a measure of bond order and strength. The Laplacian $\nabla^2\rho(r)_{BCP}$, defined as the sum of the three eigenvalues λ_1, λ_2, and λ_3 of the Hessian matrix of ρ(r), provides the most decisive criterion for bond classification: a negative Laplacian ($\nabla^2\rho < 0$) indicates local charge concentration in the internuclear region, characteristic of shared-shell

covalent interactions, while a positive Laplacian ($\nabla^2\rho > 0$) signals charge depletion and is associated with closed-shell interactions such as ionic bonds, hydrogen bonds, and van der Waals contacts. The eigenvalues λ_1 and λ_2, which are negative and describe the curvature of $\rho(r)$ perpendicular to the bond path, together with the positive λ_3 describing curvature along the bond axis, provide additional insight into the anisotropy of the electron density at the BCP. Finally, the ellipticity ε, defined as $\varepsilon = (\lambda_1/\lambda_2) - 1$, measures the deviation of the electron density from cylindrical symmetry about the bond path and serves as an indicator of π-character and electron delocalization.

The complete set of topological parameters derived from the MoPro multipolar refinement for all significant interactions in FHP is summarized in **Table IV. 3**, and the following discussion addresses each category of bonding interaction identified in the structure.

Table IV.3. Topological properties of the electron density of FHP.

A1	A2	D_{12}(Å)	D_{1cp}(Å)	D_{2cp}(Å)	ρ(eÅ^{-3})	$\nabla^2\rho$ (eÅ^{-5})	λ_1	λ_2	λ_3	ε
O3	C7	1.26	0.79	0.46	2.70	-30.99	-23.57	-20.72	13.29	0.13
O1	C5	1.35	0.83	0.52	1.99	-15.98	-15.64	-13.76	13.42	0.13
O1	C4	1.40	0.79	0.61	2.24	-15.72	-18.88	-16.33	19.49	0.15
O2	C4	1.21	0.79	0.41	2.80	-23.12	-27.59	-25.96	30.44	0.06
N1	N2	1.37	0.67	0.69	2.42	-3.13	-19.69	-16.05	32.61	0.22
N1	C9	1.29	0.81	0.48	2.21	-20.53	-16.50	-14.44	10.41	0.14
N2	H2	0.86	0.69	0.16	2.95	-92.58	-60.20	-58.12	25.73	0.03
N2	C1	1.33	0.82	0.51	2.15	-20.96	-16.55	-13.93	9.52	0.18
C9	C21	1.47	0.73	0.75	1.84	-12.07	-13.60	-10.79	12.31	0.26
C9	C10	1.49	0.73	0.75	1.79	-11.29	-13.21	-10.44	12.36	0.26
C16	C21	1.39	0.69	0.69	2.13	-17.90	-16.14	-13.27	11.51	0.21
C16	C15	1.47	0.73	0.73	1.90	-12.88	-14.01	-11.44	12.57	0.22
C16	C17	1.38	0.68	0.69	2.14	-19.29	-16.05	-13.81	10.57	0.16
C7	C3	1.44	0.70	0.73	2.02	-17.13	-15.33	-12.84	11.04	0.19
C7	C6	1.43	0.70	0.72	2.05	-17.86	-15.48	-13.07	10.69	0.18
C21	C20	1.37	0.68	0.69	2.15	-19.66	-16.20	-13.93	10.46	0.16
C3	C1	1.41	0.70	0.70	2.01	-16.49	-15.15	-12.52	11.18	0.20
C3	C4	1.45	0.74	0.71	1.97	-16.69	-15.08	-12.60	10.99	0.19
C2	H2A	0.96	0.59	0.36	2.14	-25.35	-19.44	-18.52	12.61	0.04
C2	H2B	0.95	0.59	0.36	2.14	-25.38	-19.46	-18.52	12.60	0.05
C2	H2C	0.96	0.59	0.36	2.14	-25.36	-19.48	-18.50	12.62	0.05
C2	C1	1.49	0.72	0.77	1.70	-9.93	-11.39	-10.00	11.46	0.13
C10	C15	1.42	0.71	0.71	2.03	-15.62	-15.20	-12.47	12.05	0.21
C10	C11	1.38	0.68	0.70	2.12	-18.93	-15.89	-13.68	10.64	0.16
C15	C14	1.37	0.67	0.69	2.15	-19.67	-16.18	-13.93	10.45	0.16
C5	C6	1.33	0.66	0.66	2.35	-24.70	-18.93	-14.98	9.21	0.26
C5	C8	1.47	0.77	0.70	1.82	-12.32	-12.62	-10.95	11.26	0.15
C6	H6	0.92	0.60	0.32	2.34	-34.87	-24.42	-23.23	12.79	0.05
C20	H20	0.93	0.60	0.33	2.33	-34.81	-24.28	-23.09	12.56	0.05
C20	C19	1.38	0.69	0.69	2.17	-19.43	-16.39	-13.62	10.58	0.20
C12	H12	0.92	0.59	0.33	2.33	-34.85	-24.02	-23.36	12.53	0.02
C12	C11	1.39	0.69	0.69	2.14	-18.82	-16.16	-13.42	10.75	0.20

C12	C13	1.38	0.69	0.69	2.16	-19.34	-16.35	-13.59	10.60	0.20
C11	H11	0.93	0.59	0.33	2.33	-34.80	-24.25	-23.07	12.52	0.05
C14	H14	0.92	0.59	0.32	2.34	-34.85	-24.30	-23.11	12.56	0.05
C14	C13	1.38	0.69	0.69	2.17	-19.54	-16.43	-13.66	10.55	0.20
C13	H13	0.93	0.60	0.33	2.33	-34.81	-24.28	-23.09	12.56	0.05
C8	H8A	0.95	0.59	0.36	2.14	-25.37	-19.50	-18.57	12.70	0.05
C8	H8B	0.95	0.59	0.36	2.14	-25.37	-19.51	-18.57	12.72	0.05
C8	H8C	0.95	0.59	0.36	2.14	-25.36	-19.46	-18.59	12.69	0.04
C17	H17	0.93	0.59	0.33	2.33	-34.81	-24.27	-23.08	12.54	0.05
C17	C18	1.38	0.69	0.69	2.15	-19.05	-16.24	-13.49	10.68	0.20
C19	H19	0.93	0.60	0.33	2.33	-34.76	-24.26	-23.07	12.56	0.05
C19	C18	1.39	0.69	0.69	2.14	-18.81	-16.15	-13.42	10.75	0.20
C18	H18	0.93	0.60	0.33	2.33	-34.76	-24.25	-23.06	12.55	0.05

Covalent bonds — C=O and C–N interactions: The strong covalent bonds within the pyran-dione and hydrazone units are characterized by relatively high electron densities at their BCPs and significantly negative Laplacian values, unambiguously confirming their shared-shell covalent nature. Representative examples include the C=O bond O3–C7, with $\rho = 2.70$ e·Å^{-3} and $\nabla^2\rho = -30.99$ e·Å^{-5}, and the C–O bond O2–C4, with $\rho = 2.80$ e·Å^{-3} and $\nabla^2\rho = -23.12$ e·Å^{-5}. In both cases, the eigenvalues λ_1 and λ_2 are negative while λ_3 is positive, reflecting charge accumulation perpendicular to the bond path and depletion along the internuclear axis, as expected for covalent bonding. These values fall within the ranges reported in the literature for analogous C=O and C–N bonds in Schiff base and hydrazone derivatives [19], confirming the consistency and reliability of the present multipolar refinement.

Polar covalent bonds — N–H interaction: The N2–H2 bond exhibits particularly high electron density ($\rho = 2.95$ e·Å^{-3}) and a very negative Laplacian ($\nabla^2\rho = -92.58$ e·Å^{-5}), with large λ_1 and λ_2 contributions (–60.20 and –58.12 e·Å^{-5}, respectively). These values are characteristic of a polar covalent N–H bond and are consistent with the strong hydrogen-bond donor character of this group, which participates in the intramolecular N–H···O hydrogen bond identified in the crystal structure. The high charge concentration at this BCP reflects the strongly directional nature of the N–H bond and supports its role in stabilizing the zwitterionic keto-hydrazone form of FHP.

Aromatic C–C bonds and electron delocalization: The aromatic C–C bonds of the fluorenyl system display moderate electron densities and negative Laplacians consistent with covalent character, together with moderate ellipticity values that reflect their π-character and the delocalization of electron density across the conjugated framework. The consistent pattern of negative Laplacians and intermediate ellipticities throughout the aromatic rings confirms the

planarity and extended conjugation inferred from the structural analysis, and is in good agreement with QTAIM studies of related π-conjugated systems **[20]**.

C–H bonds: The C–H bonds throughout the molecule exhibit low ellipticity values (ε < 0.10), reflecting their strong σ-character and near-cylindrical symmetry about the bond path, as expected for bonds with dominant s-character. Their ρ and $\nabla^2\rho$ values are consistent with those reported for C–H bonds in related aromatic systems.

Noncovalent interactions, hydrogen bonds, and closed-shell contacts: Several intermolecular interactions were identified at the BCP level, including C–H···O hydrogen bonds and other weak contacts. These interactions are characterized by low electron densities and positive Laplacian values at their BCPs, unambiguously confirming their closed-shell, noncovalent nature. This is fully consistent with the observations of Espinosa et al. **[18-19]**, who established that positive $\nabla^2\rho$ values at BCPs of hydrogen bond interactions reflect the dominance of electrostatic and dispersive contributions over covalent ones.

Taken together, the QTAIM topological analysis of FHP provides a complete, quantitative, and physically rigorous description of all bonding interactions present in the molecule and crystal. The topological parameters derived from the experimental electron density are in excellent agreement with values reported in the literature for structurally analogous compounds **[20]**, validating both the quality of the multipolar refinement performed with MoPro and the bonding picture that emerges from it.

The QTAIM topological parameters of the identified intermolecular interactions provide a detailed quantitative description of their nature. All interactions are characterized by relatively low electron density values at the bond critical points (ρ ≈ 0.09–0.25 e $Å^{-3}$) in **Table IV. 4** together with positive Laplacian values ($\nabla^2\rho > 0$), confirming their closed-shell, noncovalent character typical of hydrogen-bonding interactions.

A more detailed energetic analysis can be obtained from the kinetic energy density (Gcp) and potential energy density (Vcp). In all cases, the magnitude of the potential energy density |Vcp| is significantly larger than the kinetic energy density Gcp, indicating that attractive electrostatic interactions dominate over repulsive contributions. This relationship is a key criterion for hydrogen-bond stabilization within the framework of QTAIM.

Furthermore, the total energy density (Hcp = Gcp + Vcp) is expected to be negative for these interactions, which confirms their partially stabilizing nature despite their weak,

noncovalent character. The most significant interaction, observed for the O···H contacts, exhibits higher electron density and more negative Vcp values, indicating stronger hydrogen-bond character compared to the remaining contacts.

Overall, the combined analysis of ρ, $\nabla^2\rho$, Gcp, and Vcp clearly demonstrates that these intermolecular interactions are primarily governed by electrostatic attraction with a measurable stabilizing contribution, consistent with weak but structurally relevant hydrogen bonds in the crystal packing.

Table IV. 4. Topological parameters of intermolecular hydrogen-bond interactions

Parameter	O3···H2	O3···H11	O2···H2B
D12 (Å)	1.83	2.27	2.35
D1cp (Å)	1.16	1.35	1.33
D2cp (Å)	0.66	0.92	1.05
ρ (e Å^{-3})	0.25	0.09	0.09
$\nabla^2\rho$ (e Å^{-5})	3.28	1.17	1.69
λ_1	-1.35	-0.40	-0.30
λ_2	-1.02	-0.29	-0.27
λ_3	5.65	1.86	2.27
Ellipticity	0.32	0.39	0.12
Gcp (kJ mol^{-1})	10.23	13.36	15.08
Vcp (kJ mol^{-1})	-7.08	-9.02	-10.62
Type	(3,-1)	(3,-1)	(3,-1)

IV.3 Electronic and intermolecular property analysis

Subsequent to the investigations of structural and electron density properties, a more profound examination of the electronic behavior and intermolecular interactions of the compound in question was conducted through a series of theoretical analyses. These evaluations yield critical insights into electronic distribution, chemical reactivity, charge transfer characteristics, and non-covalent interactions present within the molecular system. Consequently, analyses involving frontier molecular orbitals (HOMO–LUMO), molecular electrostatic potential (MEP), reduced density gradient (RDG), Hirshfeld surface, and localization functions (LOL/ELF) were performed to achieve a comprehensive understanding of the compound's electronic properties.

IV.3.1 Frontier Molecular Orbitals and Global Reactivity Descriptors

Lowest unoccupied molecular orbitals (LUMO) are classified as electron acceptors, while the highest occupied molecular orbitals (HOMO) indicate the capacity to donate electrons. Meanwhile, the ionization potential is represented by the HOMO energy,

while the electron affinity energy is represented by the LUMO energy **[21]**. Through HOMO-LUMO analysis, the molecular orbitals were identified, and the molecule's charge transfer was analyzed. The difference in energy between the HOMO and LUMO orbits is called the energy gap; it should be noted that this amount of energy is described as an electronic excitation of the HOMO and LUMO orbitals and corresponds to the energy of electronic absorption **[22]**. The chemical reactivity of the Schiff base derivative was investigated using global chemical reactivity descriptors (GCRD) derived from DFT calculations at B3LYP/6-31G(d,p) levels of theory and B3LYP/6-311G(d,p), with solvent effects incorporated through DMSO. The energies of orbital borders (HOMO and LUMO) and the gap (E_{HOMO}-E_{LUMO}) are calculated by the DFT/6-311G(d,p) and DFT (B3LYP/6-31G (d,p)) and are shown in **Table IV. 5**. The HOMO–LUMO energy gap (ΔE) is a critical parameter that reflects the stability of molecular structures and their charge-transfer behavior. For the two employed basis sets, the calculated energy gaps were found to be 3.57 eV and 3.51 eV, respectively. Notably, when utilizing the 6-311G(d,p) basis set in the presence of the DMSO solvent, the energy gap exhibits a slight decrease to 3.53 eV. These values indicate a moderate electronic excitation energy, which suggests that the molecule possesses good chemical stability while still allowing for effective intramolecular charge-transfer processes. To understand its binding character, the distribution and the energy levels of molecular orbitals of the molecule are shown in **Figure IV.6**. Moreover, the sequential frontier orbital gaps (HOMO/LUMO = 3.53 eV, HOMO-1/LUMO+1 = 4.88 eV, HOMO-2/LUMO+2 = 5.9 eV) provide further insight into the energy levels available for excitation, confirming that HOMO→LUMO transitions dominate the low-energy absorption spectrum, potentially useful in optical or electronic device contexts. The frontier molecular orbital analysis shows that the HOMO is localized over the seton moiety, while the LUMO is delocalized over the three benzene rings, indicating that electronic excitation is likely to involve charge transfer across distinct parts of the molecule, a feature that can influence both photophysical and redox behavior.

To identify the relationship between the stability of a material and its structure, the GCRD or global chemical reactivity descriptors and the DFT method simulation are crucial. Various factors such as electron affinity (EA), ionization potential (IP), chemical potential (μ), electronegativity (χ), chemical hardness (η), chemical softness (s), nucleophilicity (ε) and electrophilicity index (ω) play an essential role in determining the reactivity of a molecule. All these quantum chemical properties of molecules could be calculated using the following equations **[23]**:

$$IP = -E_{HOMO} \quad \textbf{(Eq. IV.4)}$$

$$EA = -E_{LUMO} \quad \textbf{(Eq. IV.5)}$$

$$\chi = -\frac{1}{2}(E_{LUMO} + E_{HOMO}) \quad \textbf{(Eq. IV.6)}$$

$$\eta = \frac{1}{2}(E_{LUMO} - E_{HOMO}) \quad \textbf{(Eq. IV.7)}$$

$$\mu = \frac{1}{2}(E_{LUMO} + E_{HOMO}) \quad \textbf{(Eq. IV.8)}$$

$$S = \frac{1}{2\eta} \quad \textbf{(Eq. IV.9)}$$

$$\omega = \frac{P^2}{2\eta} \quad \textbf{(Eq. IV.10)}$$

$$\varepsilon = \frac{1}{\omega} \quad \textbf{(Eq. IV.11)}$$

The computed ionization potential (IP) and electron affinity (EA) values for the 6-311G(d,p) basis set (6.19 eV and 2.68 eV, respectively) suggest that the molecule has moderate reactivity and favorable intrinsic stability. By using DMSO, both the IP and EA values experience a slight increase (to 6.31 eV and 2.78 eV), indicating enhanced stabilization of the frontier orbitals in the polar solvent. Based on this information, the corresponding GCRD parameters were extracted (**Table IV. 5**). The findings indicate that the molecule displays significant electrophilic characteristics, as evidenced by the electrophilicity index (ω) rising from 5.03 eV in the gas phase to 5.84 eV in DMSO, which highlights an increased propensity to accept electrons in the solvent medium. The chemical hardness (η) remains relatively constant between both scenarios (approximately 1.76–1.77 eV), suggesting a consistent resistance to charge transfer. Additionally, the negative values for chemical potential further confirm the compound's structural stability, with DMSO providing a slight enhancement to this stability. In summary, the comparison illustrates that DMSO incrementally boosts the electrophilic nature and fortifies the electronic structure without making considerable changes to the molecule's hardness or softness **[24]**.

The experimental energy gap of 1.58 eV is significantly lower than the theoretical values, which range from 3.47 eV to 3.57 eV, and 3.53 eV in DMSO. This reduction is expected, as electrochemical measurements consider solvent effects and environmental conditions that stabilize charged species, reducing the gap between the HOMO and LUMO. This highlights the complementary nature of theoretical and experimental methods: theoretical calculations reflect intrinsic electronic characteristics, while electrochemical data represent behavior under practical conditions **[25]**.

Table IV.5. HOMO-LUMO gap and GCRD calculated values of FHP by DFT/B3LYP.

Parameters	Energy			
	6-31G(d,p)	6-311++G(d,p)[19]	6-311G(d,p) with solvent	6-311G(d,p)
E_{HOMO}	–6.02	–6.09	–6.31	–6.19
E_{LUMO}	–2.45	–2.62	–2.78	–2.68
ΔE (eV)	3.57	3.47	3.53	3.51
I_p	6.02	6.09	6.31	6.19
E_A	2.45	2.62	2.78	2.68
χ	4.23	4.35	4.54	4.20
P	–4.23	–4.35	–4.54	–4.20
η	1.78	1.73	1.76	1.77
S	0.89	0.86	0.88	0.88
ω	5.02	5.47	5.84	5.03
ε (ev^{-1})	0.19	0.18	0.17	0.19

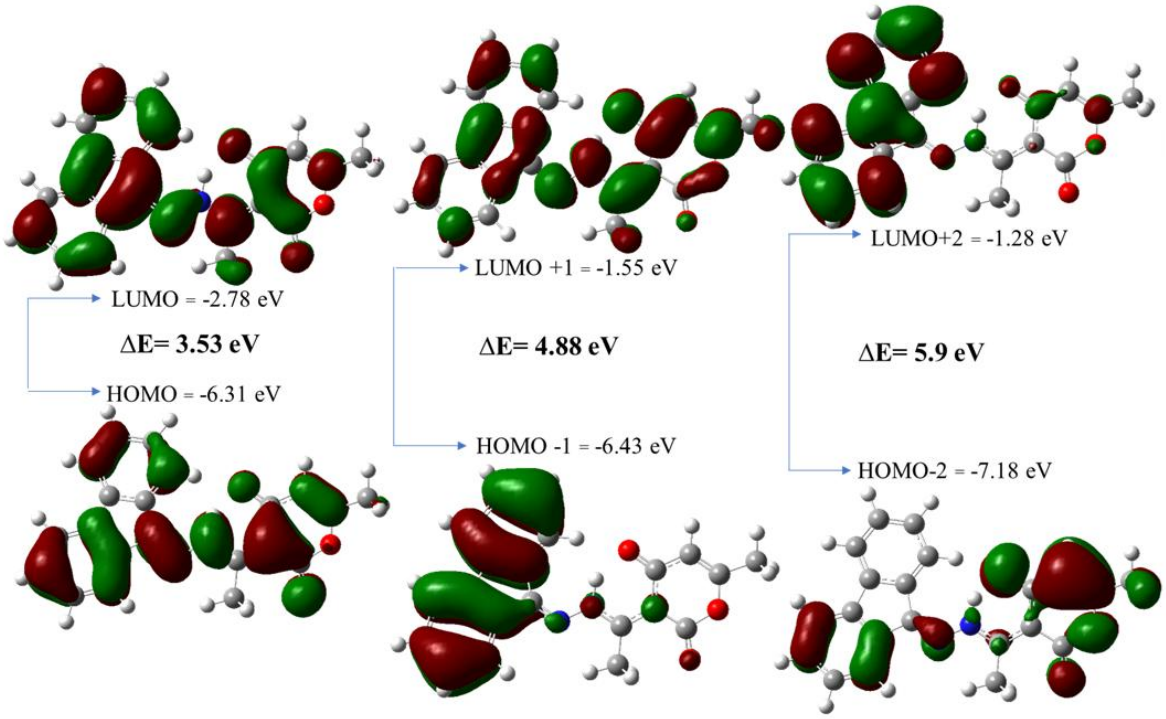


Figure IV.6. Variation of the molecule's energy gap at B3LYP/6-311G(d,p) with solvent

IV.3.2 Molecular Electrostatic Potential and Hirshfeld Surface Analysis

A complete characterization of intermolecular interactions in molecular crystals involves a topological analysis of electron density and a broader mapping of the electrostatic and geometric environments within the crystal lattice. The molecular electrostatic potential (MEP) and Hirshfeld surface analysis are complementary approaches that link the intrinsic electronic structure of isolated molecules to the supramolecular organization of the crystal. The MEP reveals the distribution of electrostatic character on the molecular surface, identifying

regions that promote intermolecular recognition. Meanwhile, the Hirshfeld surface analysis, using CrystalExplorer, quantifies and visualizes the actual intermolecular contacts in the solid state. Together, these methods provide a sequential understanding: the MEP predicts potential interactions, while the Hirshfeld surface confirms their presence and strength. Combining these tools with QTAIM topological parameters offers a comprehensive description of bonding and packing in FHP, spanning from electron density topology to crystal organization.

IV.3.2.1 Molecular Electrostatic Potential

The MEP map of FHP was computed at the B3LYP/6-311G(d,p) level of theory and mapped onto the total electron density isosurface, as shown in **Figure IV.7**. The color scale spans from –7.275 × 10^{-2} a.u. (red, maximum negative potential) to +7.275 × 10^{-2} a.u. (blue, maximum positive potential), with intermediate values represented by orange, yellow, green, and cyan, providing an intuitive visualization of the electrostatic reactivity of the molecular surface.

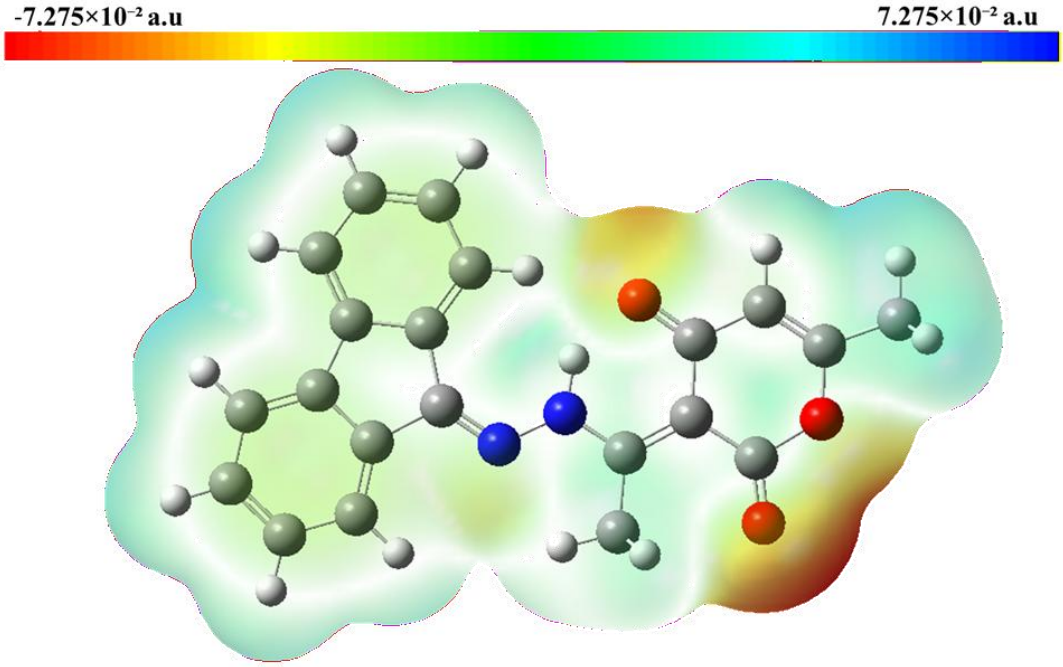


Figure IV.7. Molecular electrostatic potential (MEP) map of FHP

The MEP map reveals a pronounced spatial segregation of electrostatic character across the FHP framework, fully consistent with its donor–π–acceptor architecture. The regions of highest negative potential, displayed in deep red and orange, are sharply localized on the oxygen atoms of the pyran-dione moiety, directly reflecting the presence of lone pairs on the carbonyl

and ring oxygens. These electron-rich regions identify the pyran-dione oxygens as the dominant hydrogen-bond acceptors and preferred sites for electrophilic approach, a prediction directly confirmed by the Hirshfeld surface, where the most prominent red features on the d_{norm} map and the sharp O···H spikes in the fingerprint plots are located precisely in their vicinity.

In contrast, the fluorenyl aromatic system presents a predominantly green to light blue surface, reflecting the delocalized and near-neutral electrostatic character of the π-system. The mildly positive aromatic C–H periphery accounts for the C–H···O and C–H···π contacts identified on the Hirshfeld surface and the substantial H···C contribution of 29% in the fingerprint plots. The flat aromatic faces with near-zero MEP curvature are further consistent with the π···π stacking interactions evidenced by the alternating concave–convex pattern on the shape index surface.

The N–H group of the hydrazone linkage occupies an intermediate cyan-green region on the MEP, reflecting its partial positive character as a hydrogen-bond donor. Its interaction with the electron-rich pyran-dione oxygens constitutes the strongest and most directional contact in the system, producing the shortest and most intense red spot on the d_{norm} surface at 2.412 Å, fully validating the MEP-based prediction.

IV.3.2.2 Hirshfeld Surface Analysis and Two-Dimensional Fingerprint Plots

The Hirshfeld surface analysis of FHP **[13]**, carried out using CrystalExplorer, provides the crystallographic counterpart to the MEP analysis presented above, translating the electrostatic tendencies of the isolated molecule into a quantitative map of the actual intermolecular contacts present in the crystal. **Figure IV.8.** presents the Hirshfeld surfaces mapped with d_{norm}, d_e, d_i, shape index, and curvedness, while **Figure IV.9.** shows the two-dimensional fingerprint plots decomposed by contact type.

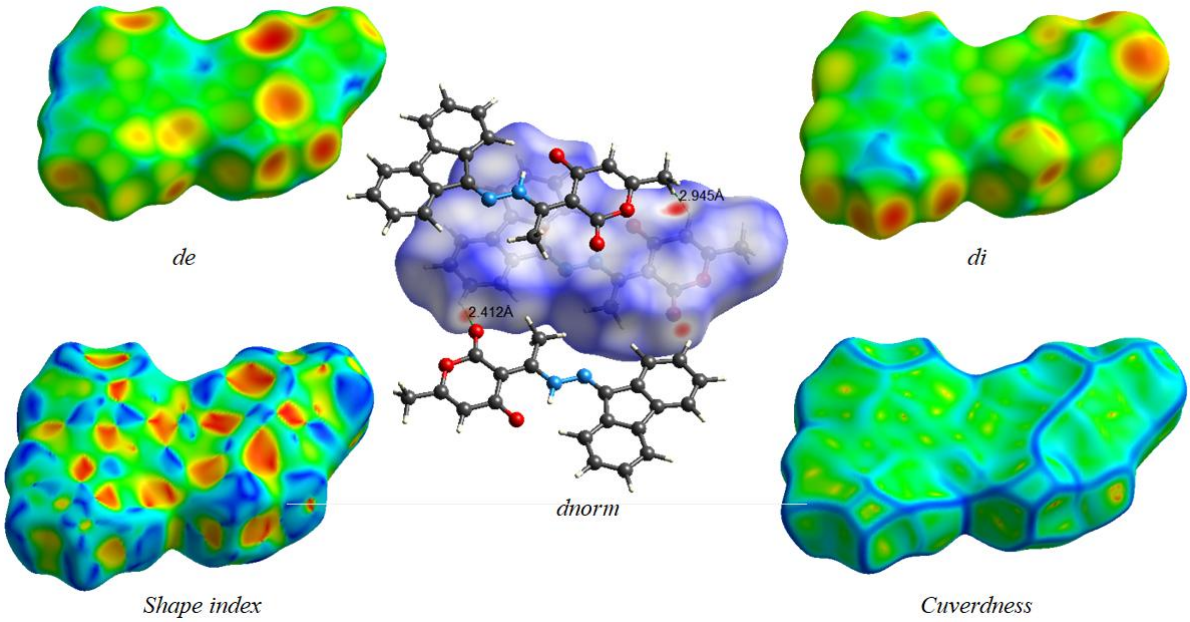


Figure IV.8. Hirshfeld surface maps of FHP: d_{norm}, d_e, d_i, shape index and curvedness.

d_{norm} surface: The d_{norm} map encodes normalized contact distances relative to van der Waals radii, serving as a key indicator of close intermolecular contacts. The FHP surface features two distinct red areas that highlight interaction sites predicted by the MEP. The most prominent red spot, located at 2.412 Å in the N–H donor group, indicates a strong intramolecular N–H···O hydrogen bond, significantly below the van der Waals radii, demonstrating the importance of this interaction. A second, less intense red feature appears at 2.945 Å near an oxygen acceptor, corresponding to an intermolecular C–H···O hydrogen bond. The correlation between these red spots and the electron-rich oxygen areas on the MEP confirms the strongest intermolecular contacts. The blue and white background of the d_{norm} surface indicates normal or longer van der Waals contacts in the rest of the molecular surface, consistent with the weakly polar aromatic C–H characteristics observed on the MEP.

d_e and d_i surfaces: The d_e and d_i maps, which encode the distances from the Hirshfeld surface to the nearest external and internal nuclei, respectively, provide complementary spatial information. The d_e surface shows warm-colored patches concentrated around the oxygen-containing pyran-dione region, reflecting the close approach of neighboring molecule atoms in that area, in direct agreement with the negative MEP potential localized on those oxygen atoms, which attracts the electropositive C–H and N–H groups of adjacent molecules. The d_i surface presents a corresponding pattern viewed from the interior of the molecular volume, confirming

the directionality and asymmetry of the intermolecular environment, consistent with the MEP charge distribution.

Shape index and curvedness: The shape index surface displays a characteristic pattern of alternating red, concave regions and blue, convex regions across the aromatic face of the fluorenyl system. This pattern is the unambiguous geometric fingerprint of π···π stacking interactions and is fully consistent with the near-neutral green regions observed on the MEP over the aromatic faces, where the flat electrostatic potential surface facilitates parallel face-to-face aromatic overlap. The curvedness map reinforces this interpretation, showing broad flat green patches across the aromatic system, indicative of extended planar contacts between neighboring fluorenyl units in the crystal stack.

Two-dimensional fingerprint plots: The decomposed fingerprint plots provide a quantitative inventory of intermolecular contacts in the crystal as percentages of the total Hirshfeld surface area, relating to the MEP electrostatic landscape. H···H contacts dominate at 41.8%, indicated by broad diffuse scatter in the fingerprint plot, reflective of extensive van der Waals interactions in the hydrogen-rich aromatic regions. H···C / C···H contacts contribute 29%, shown as asymmetric wings typical of C–H···π interactions, where aromatic hydrogen interacts with neighboring π-faces. O···H / H···O contacts account for 14.2%, appearing as sharp spikes linked to C–H···O hydrogen bonds due to strong electrostatic complementarity. C···C contacts contribute 4.2%, aligning with π···π stacking confirmed by the MEP. O···C / C···O and N···C / C···N contacts each contribute around 4%, reflecting weak polar interactions involving heteroatoms. Finally, N···H / H···N contacts form a minor 1.3%, associated with the hydrazone N–H donor.

The quantitative analysis reveals that the intermolecular interactions in FHP are primarily driven by dispersion-type H···H and H···C contacts due to the large aromatic surface area, alongside significant O···H hydrogen bonds from the negatively charged pyran-dione oxygens. This framework, characterized by strong directional hydrogen bonds and extensive aromatic van der Waals and π-stacking contacts, supports the three-dimensional supramolecular architecture observed in the crystal packing analysis, aligning with the QTAIM topological analysis of FHP's electronic and structural organization in the solid state.

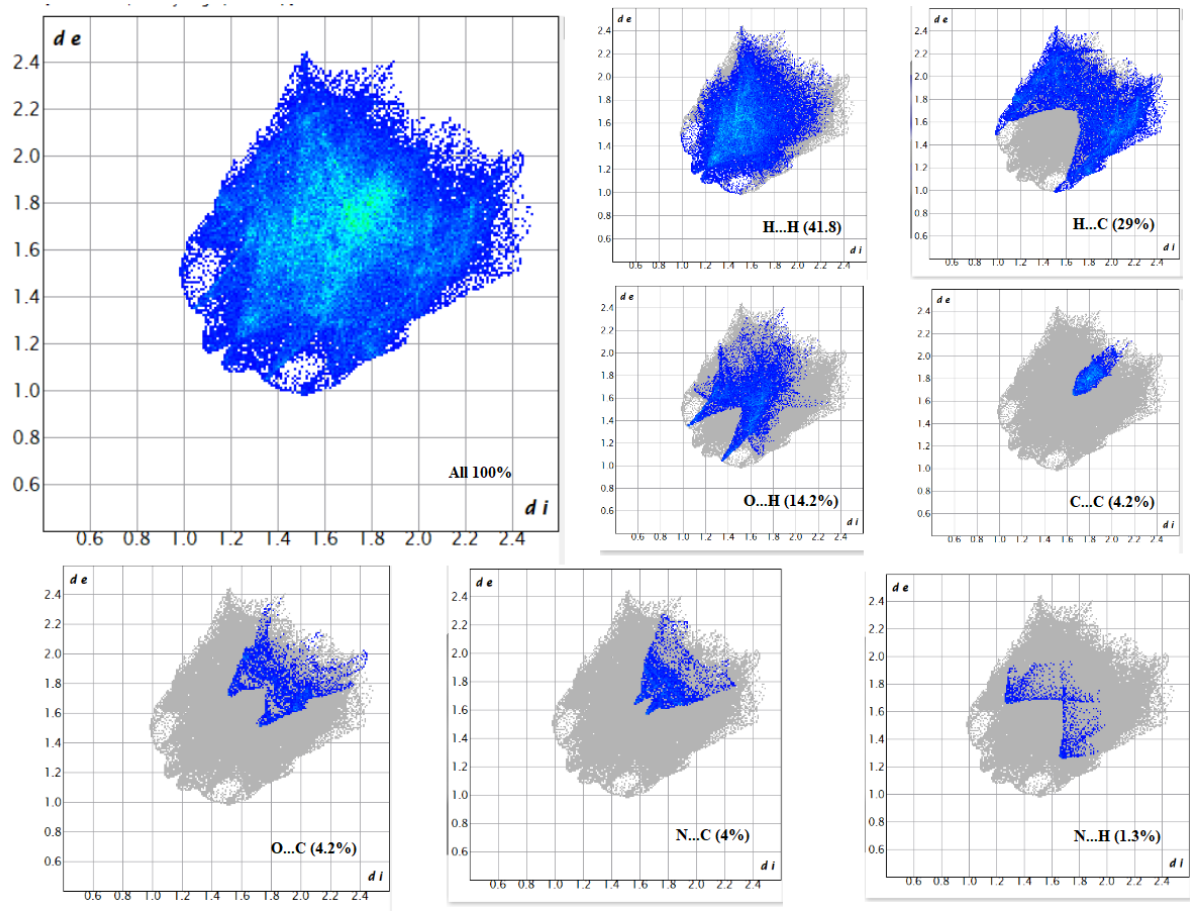


Figure IV.9. Two-dimensional fingerprint plots of FHP and their decomposed contact contributions

IV.3.3 Reduced Density Gradient (RDG) Analysis and Non-Covalent Interaction Mapping

The Reduced Density Gradient (RDG) is a dimensionless scalar quantity derived from the electron density and its spatial gradient, widely employed to characterize and visualize both intra- and intermolecular interactions within a chemical system. Mathematically, the RDG is expressed as **[26]:**

$$RDG(r) = \frac{1}{2(3\pi r^2)} \frac{|\nabla \rho(r)|}{\rho(r)^{\frac{4}{3}}} \qquad \textbf{(Eq. IV.12)}$$

where ρ(r) represents the electron density at a given point r in three-dimensional space, and ∇ρ(r) denotes its gradient vector, reflecting the rate and direction of density variation. In regions of space where non-covalent interactions (NCIs) occur, the electron density is relatively low, and the RDG exhibits characteristic spikes when plotted against the reduced variable $\text{sign}(\lambda_2)\cdot\rho$, making this approach a powerful tool for interaction fingerprinting.

To extract chemically meaningful information, the computed RDG values were mapped onto a two-dimensional scatter plot as a function of sign(λ_2)·ρ, where λ_2 is the second eigenvalue of the electron density Hessian matrix. The sign of λ_2 serves as a critical discriminator for the nature of the identified interactions: negative values of sign(λ_2) are associated with attractive bonded interactions, such as hydrogen bonds and strong electrostatic interactions; positive values indicate destabilizing, repulsive non-bonded interactions typically found in sterically congested ring centers; and values near zero, in the intermediate region, correspond to weak, dispersive van der Waals (VDW) interactions. This elegant sign-based classification enables a comprehensive mapping of interaction types across the molecular framework in a single unified analysis **[27]**.

In the present work, both the two-dimensional scatter diagram and the three-dimensional RDG isosurface plots were generated using the Multiwfn and VMD software packages, and the resulting interaction maps are presented in **Figure IV.10.** The color-coding scheme employed in the isosurface visualization provides an immediate and intuitive distinction between the different interaction categories:

- **Green isosurface regions** correspond to weak van der Waals interactions in the intermediate sign(λ_2)·ρ range, observed between the atomic pairs **C11–H11···N2–H2** and **C17–H17···C14–H14**. These dispersive interactions, though individually weak, play a significant role in stabilizing the overall molecular conformation and crystal packing arrangement.
- **Red isosurface regions** are indicative of strong repulsive steric interactions arising from spatial electron density crowding. In the present molecule, these repulsive effects are prominently localized at the centers of aromatic and heterocyclic rings, specifically within the ring systems defined by atoms **(C10, C12)**, **(C9, C21)**, **(C17, C21)**, and **(C4, O1)**. Such steric congestion at ring centers is a well-known consequence of the Pauli repulsion between overlapping electron clouds and is commonly observed in polycyclic systems.
- **Mixed red-green regions**, reflecting a weak-to-moderate repulsive character, were identified between **C2–H2B···O2** and **C2–H2C···N1**. These regions suggest the presence of geometrically close but electronically weakened contacts, which contribute marginally repulsive character to the local interaction landscape.
- **Blue isosurface regions** represent the strongest attractive interactions and are diagnostic of hydrogen bonding. A well-defined intramolecular hydrogen bond, **N2–H2···O3–C7**, was clearly identified and highlighted in blue. The formation of this intramolecular N–H···O

hydrogen bond indicates significant electron density accumulation in the internuclear region, contributing to the conformational rigidity and thermodynamic stability of the molecular structure.

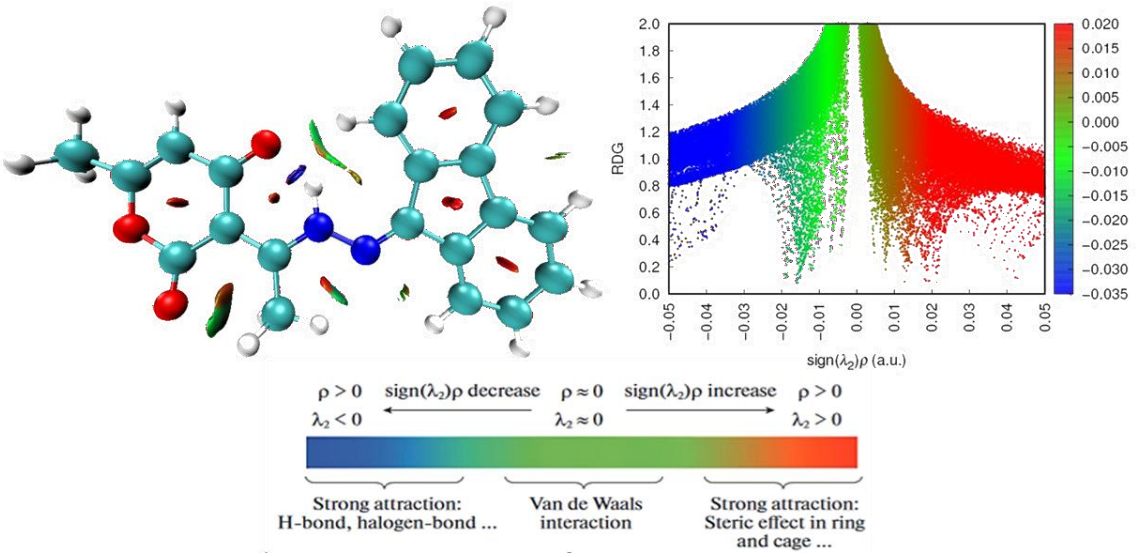


Figure IV.10. The scatter diagram and gradient isosurfaces of FHP.

These findings were further corroborated through topological analysis of the electron density within the framework of the Quantum Theory of Atoms in Molecules (QTAIM), as implemented in the Multiwfn program. QTAIM analysis enabled the precise identification of bond critical points (BCPs), ring critical points (RCPs), and their associated electron density and Laplacian values, thereby providing a rigorous quantum mechanical basis for the classification of all bonding and non-bonding interactions observed in the RDG isosurface maps. Together, the RDG and QTAIM approaches offer a complementary and comprehensive picture of the electronic structure and interaction topology of the studied molecule.

IV.3.4 Electron Localization Function (ELF) and Localized Orbital Locator (LOL) Analysis

The analysis of molecular surfaces based on covalent bonding interactions provides a powerful means of visualizing and interpreting the spatial distribution of electrons within a molecule. Two complementary quantum chemical descriptors, the Electron Localization Function (ELF), denoted τ(r), and the Localized Orbital Locator (LOL) [28], denoted η(r), were employed in this study to construct detailed maps of electron pair probability distributions across the molecular space. Both functions were computed using the Multiwfn program, and

their corresponding color-shaded and contour maps for the title molecule are presented in **Figures IV.11.** and **IV.12.**, respectively.

Although ELF and LOL **[29]** share a common dependence on the kinetic energy density of the electron system, they differ fundamentally in their conceptual foundations and the chemical information they convey. ELF, τ(r), is grounded in the concept of electron pair density, quantifying the probability of finding an electron pair localized in a given region of space by comparing the local kinetic energy density to that of a homogeneous electron gas reference model. Its value is dimensionless and strictly bounded between 0.0 and 1.0, where values in the range 0.5–1.0 indicate regions of high electron localization corresponding to bonding electron pairs and non-bonding lone pairs, while values below 0.5 are characteristic of delocalized electron behavior, as typically encountered in aromatic or conjugated systems. LOL, η(r), on the other hand, is rooted in the spatial behavior of localized molecular orbitals, specifically capturing regions where the gradients of such orbitals are maximized due to orbital overlap. Like ELF, LOL values are normalized between 0 and 1, with values exceeding 0.5 signaling dominant electron localization attributable to covalent bonds, lone pairs, or nuclear shell structure. Importantly, LOL tends to produce sharper and more visually distinct spatial boundaries than ELF, making it a more decisive descriptor for identifying localization features within complex molecular frameworks.

The ELF color-shaded map of the title molecule, shown in **Figure IV.11,** reveals several chemically significant features. High ELF regions, represented by red and orange colors approaching $\tau(r) \rightarrow 1.0$, are prominently observed in the vicinity of hydrogen atoms, consistent with the presence of highly localized bonding electrons in C–H and N–H covalent bonds, where electron–electron repulsion is minimal, and pairing probability is high. In contrast, blue regions observed around select carbon atoms reflect low ELF values below 0.5, indicating the presence of a delocalized electron cloud extending across the aromatic and conjugated portions of the molecular skeleton. This delocalization is an expected consequence of π-electron spreading in aromatic systems, where electrons are distributed across multiple atomic centers rather than confined between any two specific atoms. Intermediate ELF regions represented by green and yellow colors correspond to transition zones between localized and delocalized electron behavior, commonly found along bond paths and at the periphery of atomic shells.

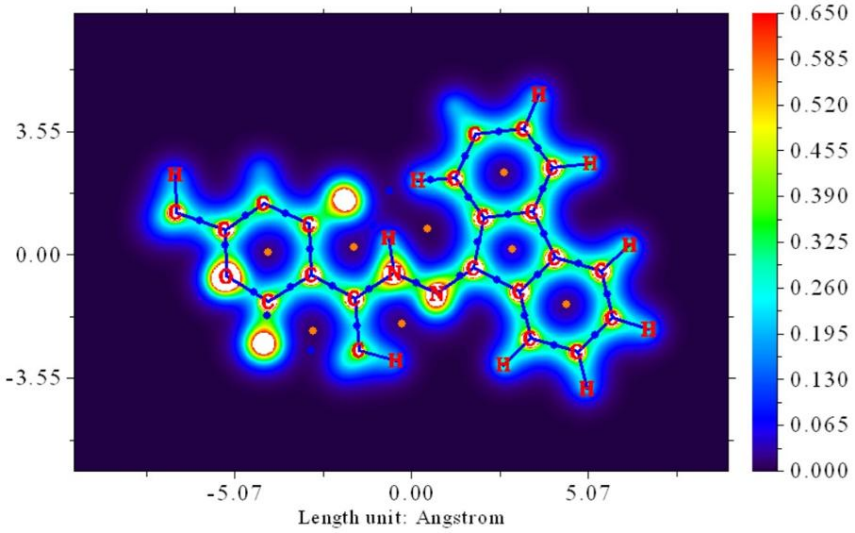


Figure IV.11. ELF, color-filled and contour map of the title compound

The LOL map presented in **Figure IV.12** provides a complementary and more visually informative picture of electron localization within the molecule. The central regions of hydrogen atoms appear white in the map, indicating that the LOL value at those points exceeds the upper limit of the color scale at $\eta(r) > 0.80$, reflecting the extremely high degree of electron localization at hydrogen nuclear positions where the single valence electron is tightly confined with no competing inner shell electrons. Red-colored regions observed between hydrogen and nitrogen atoms are indicative of highly localized electron density associated with strong N–H covalent bonds, where significant orbital overlap and electron pairing confirm the presence of well-defined covalent interactions. Blue circular regions surrounding carbon and oxygen nuclei correspond to zones of electron depletion located at the boundary between the inner core shell and the outer valence shell of these heavier atoms, reflecting the well-known inter-shell structure of multi-electron atoms where the kinetic energy density rises sharply, reducing localization probability and creating visible shell boundaries in the LOL map.

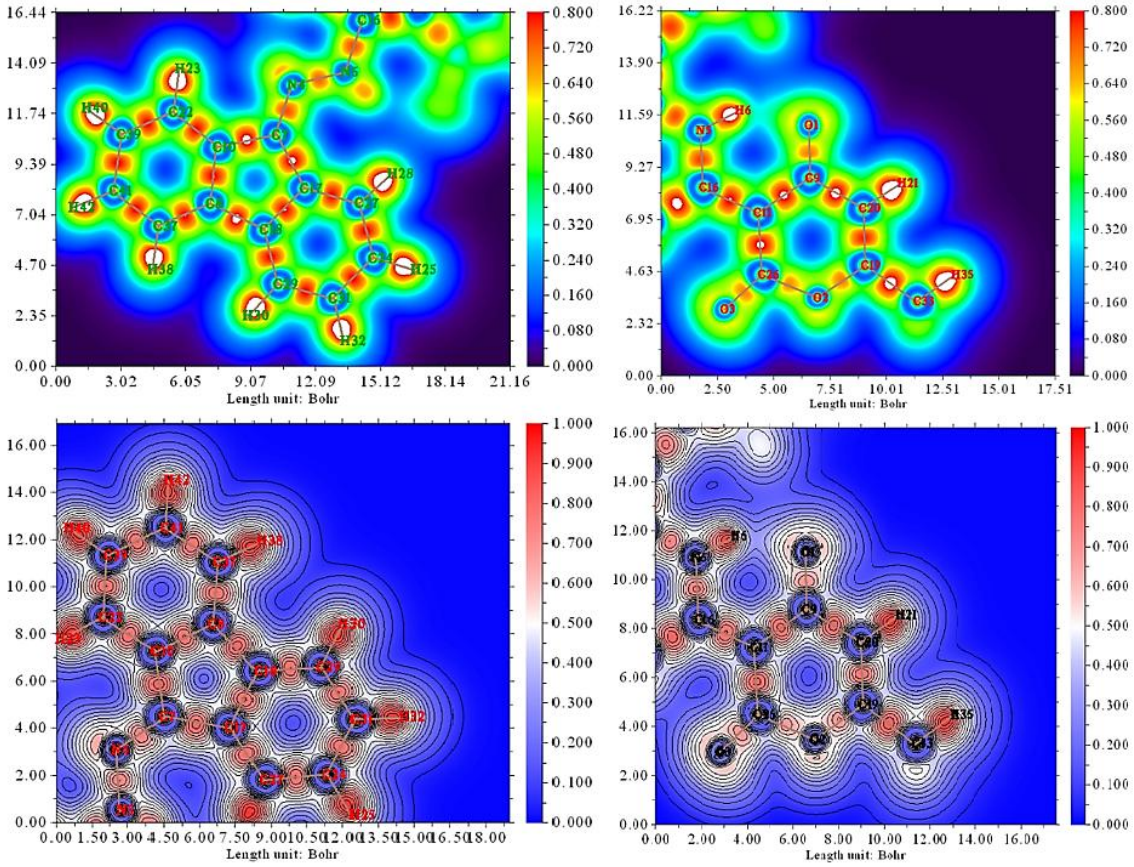


Figure IV.12. LOL color-filled and contour maps for the title compound.

While both ELF and LOL successfully capture the essential features of electron localization in the title molecule, LOL consistently produces more sharply defined and chemically interpretable spatial features, offering cleaner contrast between bonding, non-bonding, and electron depletion regions. This makes LOL the more decisive tool for identifying subtle electronic structure details, particularly in systems with mixed covalent, aromatic, and delocalized bonding character. Taken together, the ELF and LOL analyses provide a robust and comprehensive description of the electronic architecture of the molecule, offering valuable and complementary insight into its bonding nature, electron distribution, and overall chemical stability.

IV. 4 Conclusion

In this chapter, an extensive structural, topological, and theoretical investigation of the zwitterionic hydrazone derivative FHP was carried out using complementary experimental and computational approaches. The synthesis and crystallographic characterization confirmed the formation of a stable zwitterionic structure stabilized by a strong intramolecular N–H···O hydrogen bond. Geometry optimization calculations demonstrated excellent agreement with experimental X-ray diffraction results. The HOMO–LUMO analysis and global reactivity descriptors revealed efficient intramolecular charge transfer and moderate chemical stability. MEP analysis identified the principal electrophilic and nucleophilic reactive sites within the molecule. RDG, ELF, and LOL analyses highlighted the presence of important non-covalent interactions together with significant electron delocalization over the conjugated framework. Finally, the experimental charge density investigation using the Hansen–Coppens multipolar model and AIM topological analysis confirmed the covalent nature of the principal bonds and the stabilizing role of weak intermolecular interactions. Overall, the obtained results demonstrate that the FHP molecule possesses remarkable electronic delocalization and charge-transfer properties, making it a promising candidate for optoelectronic and nonlinear optical applications.

Bibliographic references

[1] Uddin, M. N., Salam, M. A., Chowdhury, D. A., & Siddique, M. A. B. "Binuclear Tetrahedral Dimeric Mg (II) Complexes of Dibasic Tridentate Schiff Base Ligands and Their Microbial Studies.". J. Nat. Sci. 2014 Vol. 13(1), p. 23.

[2] Uddin, Mohammad Nasir, Md Abdus Salam, and Md Abu Bakar Siddique. "Complexes of VO3+ with dibasic tetradentate Schiff bases and their microbial studies." American Journal of Chemistry and Applications 1.2, 2014, pp. 19-27.

[3] Hameed A., Al-Rashida M., Uroos M., Ali S. A. and Khan K. M., "Schiff bases in medicinal chemistry: a patent review (2010-2015)." Expert opinion on therapeutic patents 2017, vol. 27, no 1, pp. 63-79

[4] Yousaf, M., Hassan, A., Ahmad, S., Idrees, M., & Adil, M. "Biointerface Research in Applied Chemistry." Volume 10, Issue 2, 2020, pp. 5217 - 5223

[5] Ourari, A., Ouari, K., Khan, M. A., & Bouet, G. "Dioxygen activation with a cytochrome P450 model. Characterization and electrochemical study of new unsymmetrical tetradentate Schiff-base complexes with iron (III) and cobalt (II)." Journal of Coordination Chemistry, 2008, vol. 61, no 23, pp. 3846-3859.

[6] Kagkelari, A., Papaefstathiou, G. S., Raptopoulou, C. P., & Zafiropoulos, T. F. "Synthesis and structure of N-salicylidene-o-aminophenolato gallium (III) complexes." Polyhedron, 2009, vol. 28, no 15, pp. 3279-3283.

[7] Bader, Nabil Ramadan. "Applications of schiff's bases chelates in quantitative analysis a review." RASAYAN j. Chem, 2010, vol. 3, no 4, pp. 660-670.

[8] Guerraoui, A., Fellahi, Z., Direm, A., Thabti, S., Djedouani, A., & Boumaza, A. "Synthesis, Spectral, Structural Characterizations and HSA of the interactions in a New Zwitterionic Schiff Base." *Conference Paper*, November 2021.

[9] Guerraoui, A., Djedouani, A., Jeanneau, E., Boumaza, A., Alsalme, A., Zarrouk, A., & Warad, I. "Crystal structure and spectral of new hydrazine-pyran-dione derivative: DFT enol↔hydrazone tautomerization via zwitterionic intermediate, Hirshfeld analysis and optical activity studies." *Journal of Molecular Structure*, 2020, vol. 1220, p. 128728.
[10] Espinosa, E., Souhassou, M., Lachekar, H., and Lecomte, C., *Acta Crystallogr. B*, 1999, vol. 55, p. 563.
[11] Ganguly, A., *Comput. Theor. Chem*., 2023, vol. 1226, p. 114210.
[12] Jelsch, C., Guillot, B., Lagoutte, A., and Lecomte, C., *J. Appl. Crystallogr*., 2005, vol. 38, p. 38.
[13] Guerraoui, A., Djedouani, A., Jeanneau, E., Boumaza, A., Alsalme, A., Zarrouk, A., Salih, K.S.M., and Warad, I., *J. Mol. Struct*., 2020, vol. 1220, p. 128728.
[14] Chouaih, A., Hamzaoui, F., and Vergoten, G., *J. Mol. Struct*., 2005, vol. 738, p. 33.
[15] Fischer, R.X., and Tillmanns, E., *Acta Crystallogr. C*, 1988, vol. 44, p. 775.
[16] Espinosa, E., Lecomte, C., and Molins, E., *Chem. Phys. Lett*., 1999, vol. 300, no. (5–6), p. 745.
[17] Espinosa, E., Alkorta, I., Elguero, J., and Molins, E., *J. Chem. Phys*., 2002, vol. 117, p. 5529.
[18] Espinosa, E., Souhassou, M., Lachekar, H., and Lecomte, C., *Acta Crystallogr. B*, 1999, vol. 55, p. 563.
[19] Ganguly, A., *Comput. Theor. Chem*., 2023, vol. 1226, p. 114210.
[20] Benaissi, H., Drissi, M., Yahiaoui, S., Megrouss, Y., Chouaih, A., and Hamzaoui, F., *J. Optoelectron. Biomed. Mater*., 2018, vol. 10, no. 3, p. 73.
[21] Boukabcha, N., Direm, A., Drissi, M., Megrouss, Y., Khelloul, N., Dege, N., Tuna, M., and Chouaih, A., *Inorg. Chem. Commun*., 2021, vol. 133, p. 108884.
[22] Silvi, B., and Savin, A., *Nature*, 1994, vol. 371, p. 683.
[23] Jacobsen, H., *Can. J. Chem*., 2009, vol. 87, p. 695.
[24] Tamer, O., Şimşek, M., Avcı, D., and Atalay, Y., *Spectrochim. Acta A Mol. Biomol. Spectrosc*., 2023, vol. 286, p. 122005.
[25] Sęk, D., Siwy, M., Małecki, J.G., Kotowicz, S., Golba, S., Nowak, E.M., Sanetra, J., and Schab-Balcerzak, E., *Spectrochim. Acta A Mol. Biomol. Spectrosc*., 2017, vol. 175, p. 168.
[26] Noureddine, O., Issaoui, N., Medimagh, M., Al-Dossary, O., and Marouani, H., *J. King Saud Univ. Sci*., 2021, vol. 33, p. 101334.
[27] Saidj, M., Djafri, A., Rahmani, R., Belkafouf, N.E.H., Boukabcha, N., Djafri, A., and Chouaih, A., *Polycycl. Aromat. Compd*., 2023, vol. 43, no. 3, p. 2152.
[28] Silvi, B., and Savin, A., *Nature*, 1994, vol. 371, p. 683.
[29] Jacobsen, H., *Can. J. Chem*., 2009, vol. 87, p. 695.

CHAPTER V

Nonlinear Optical (NLO) Properties

V.1 Introduction 92
V.2 Fundamentals of Nonlinear Optics 93
V.2.1 Electromagnetism in Material Media 93
V.2.2 Polarization 93
V.2.3 Spontaneous and Stimulated Emission 93
V.2.4 Linear vs Nonlinear Optics 94
V.3 Basics of NLO 94
V.3.1 Light Sources and Lasers 94
V.3.2 Properties of NLO Materials 94
V.4 Basics of NLO Materials 95
V.4.1 Methodology and Studied Parameters 95
V.5 Results and Discussion 96
V.5.1 Molecular Structure 96
V.5.2 Nonlinear optical properties 97
V.5.3 Static NLO properties 97
V.5.4 Dynamic NLO properties 98
V.5.5 Anisotropic contributions 99
V.6 Conclusion 100
Bibliographic references 100

V.1 Introduction

The (E)-3-(1-(2-(9H-fluoren-9-ylidene)hydrazineyl)ethylidene)-6-methyl-2H-pyran-2,4(3H)-dione (FHP) has attracted considerable attention in the field of nonlinear optics (NLO) owing to its highly conjugated molecular structure and remarkable electronic properties. The molecule contains electron-donating and electron-accepting fragments connected through an extended π-conjugated system, which promotes efficient intramolecular charge transfer and enhances molecular polarization. Such donor–π–acceptor architectures are widely recognized for their strong nonlinear optical responses and their potential applications in advanced optoelectronic technologies.

Organic compounds containing azomethine ($C = N$)linkages and heteroatoms such as nitrogen and oxygen generally exhibit enhanced charge delocalization and electronic flexibility, leading to improved optical and electronic properties. In the FHP molecule, the fluorene moiety behaves mainly as an electron donor, whereas the pyran-dione fragment acts as an electron acceptor, facilitating electron migration through the conjugated molecular framework. This electronic interaction contributes significantly to the stabilization of excited states and enhances the nonlinear optical activity of the compound.

Nonlinear optical materials are of great scientific and technological importance due to their applications in optical communication systems, optical switching, electro-optic modulation, laser technologies, photonic devices, frequency conversion, and information storage systems. The nonlinear optical efficiency of a molecular system is closely related to several important electronic parameters, including dipole moment, molecular polarizability, first-order hyperpolarizability, and second-order hyperpolarizability. The first hyperpolarizability is associated with second-order nonlinear optical phenomena such as second harmonic generation, whereas the second hyperpolarizability is related to third-order nonlinear optical effects including two-photon absorption and optical limiting behavior.

In the present work, the structural, electronic, and nonlinear optical properties of the FHP molecule were investigated using density functional theory (DFT) calculations. Particular attention was devoted to the analysis of frontier molecular orbitals, molecular electrostatic potential, intramolecular charge-transfer characteristics, dipole moment, linear polarizability, first hyperpolarizability, and second hyperpolarizability. The obtained theoretical results provide valuable insight into the relationship between molecular structure and nonlinear optical

behavior and demonstrate the potential applicability of the investigated compound as a promising organic material for photonic and optoelectronic applications.

V.2 Fundamentals of Nonlinear Optics

V.2.1 Electromagnetism in Material Media

The interaction between electromagnetic radiation and matter is fundamentally described by Maxwell's equations. These equations outline how electric and magnetic fields propagate through space and interact with various materials. When an external electric field is applied to a molecular system, it induces a displacement or redistribution of the electronic cloud surrounding the atoms and molecules. This phenomenon, known as polarization, occurs because the external field creates forces that act on the charged particles within the matter. As a result, there is a slight separation of positive and negative charges within the material **[1]**. This redistribution alters the local electric field within the medium, affecting how the material responds to the electromagnetic radiation. The degree of polarization depends on factors such as the strength of the applied electric field, the frequency of the radiation, and the intrinsic properties of the material, including its dielectric constant and molecular structure. This complex interplay is essential for understanding various optical phenomena, such as refraction, dispersion, and absorption, as well as the behavior of materials under different electromagnetic environments.

V.2.2 Polarization

The polarization P of a material subjected to an electric field E may be represented as a power series expansion **[2]**.

$$\boldsymbol{P = \varepsilon_0\left(\chi^{(1)}E + \chi^{(2)}E^2 + \chi^{(3)}E^3 + \cdots\right)} \qquad \textbf{(Eq. V. 1)}$$

In the context of nonlinear optics, the parameter $\chi^{(1)}$ represents the linear susceptibility, while $\chi^{(2)}$ and $\chi^{(3)}$ denote the second- and third-order nonlinear susceptibilities, respectively. These higher-order susceptibilities play a crucial role in phenomena such as second harmonic generation (SHG), sum-frequency generation, and optical Kerr effects.

V.2.3 Spontaneous and Stimulated Emission

Understanding spontaneous and stimulated emission is key to grasping light–matter interactions **[3]**.

Spontaneous emission occurs randomly when an excited atom or molecule returns to a lower energy state, emitting incoherent light without external influence. In contrast, stimulated emission happens when an incoming photon prompts an excited atom to release its energy as a photon, resulting in amplified, coherent light [4-6]. This process is fundamental to laser operation, enabling the generation of intense light that is synchronized in phase, frequency, and direction. The coherent light produced through stimulated emission is essential for various nonlinear optical effects, which are crucial in applications like telecommunications, medical technologies, and laser manufacturing. Therefore, understanding these two types of emission is vital for advancing in optics and photonics.

V.2.4 Linear vs Nonlinear Optics

In the realm of linear optics, the phenomenon of induced polarization responds proportionately to the strength of an applied electric field. This relationship is characterized by the first-order susceptibility, denoted as $\chi^{(1)}$. This linear interaction is straightforward and predominant under typical lighting conditions. On the other hand, nonlinear optics comes into play when we encounter high-intensity electromagnetic fields. In these scenarios, the interaction becomes more complex as higher-order susceptibilities, such as the second and third, begin to play a significant role. This complexity gives rise to fascinating optical phenomena, including second harmonic generation, where light of a specific frequency is converted into light of double that frequency and various third-order optical effects that can lead to unique applications in technology and research [7-8].

V.3 Basics of NLO

V.3.1 Light Sources and Lasers

Nonlinear optical effects necessitate the use of high-intensity and coherent light sources. Lasers are particularly well-suited for this purpose because they possess characteristics such as monochromaticity, coherence, and high-power density. These attributes facilitate robust interactions between light and matter, making lasers essential tools in nonlinear optics.

V.3.2 Properties of NLO Materials

Efficient nonlinear optical (NLO) materials are distinguished by their strong intramolecular charge transfer, high molecular polarizability, and notable hyperpolarizability. Among these, organic systems, especially Schiff base derivatives, present promising options.

This is largely due to their π-conjugated structures and donor-acceptor configurations, which enhance electron delocalization and contribute to their NLO properties.

V.4 Basics of NLO Materials

Nonlinear optical phenomena necessitate the use of high-intensity light sources, which are usually lasers. This is because lasers possess characteristics such as coherence, monochromaticity, and high-power density. These features facilitate a strong interaction with matter, thereby amplifying nonlinear responses.

Materials that demonstrate significant nonlinear optical (NLO) properties must have certain specific characteristics, including:

- High molecular polarizability
- Significant hyperpolarizability
- Strong intramolecular charge transfer (ICT)
- Non-centrosymmetric structure (facilitating second-order effects)

Organic compounds, especially Schiff bases, are notable for their π-conjugated systems and donor–acceptor configurations. These attributes enable charge delocalization and may enhance nonlinear optical (NLO) responses [9].

V.4.1 Methodology and Studied Parameters

The nonlinear optical properties of the Schiff base compounds under investigation were analyzed using Density Functional Theory (DFT). This approach offers precise insights into the electronic structure and associated optical characteristics.

The following parameters were evaluated:

- **Dipole moment (μ):** The dipole moment is a vector quantity that provides a measure of the degree of charge separation within a molecule. It is calculated as the product of the magnitude of the charge and the distance between the centers of positive and negative charges. A higher dipole moment indicates a greater polarity, meaning that the molecule has a significant difference in electronegativity between the atoms, leading to uneven charge distribution. This property is crucial for understanding molecular interactions, solubility, and behavior in an electric field.
- **Polarizability (α):** Polarizability refers to the ability of the electron cloud surrounding a molecule to distort in response to an external electric field. It quantifies how easily the electron density can be displaced, which can induce a dipole moment in the molecule, even

if it is initially nonpolar. The polarizability depends on the size and shape of the electron cloud and the nature of the chemical bonds within the molecule. Molecules with higher polarizability tend to have stronger van der Waals interactions and exhibit different optical properties [10-12].

- **First hyperpolarizability (β):** First hyperpolarizability is a third-order nonlinear optical property that describes how the polarization of a material responds to an applied electric field in a nonlinear manner. Specifically, it is linked to second-order nonlinear optical effects, such as second harmonic generation, where two photons combine to form a new photon with double the energy (or frequency) of the original photons. This property is significant in the development of advanced materials for optical applications, such as frequency doubling in lasers [13].
- **Second hyperpolarizability (γ):** Second hyperpolarizability deals with third-order nonlinear optical phenomena and is an essential parameter in understanding processes like third harmonic generation, where three photons combine to produce a new photon with triple the energy. Additionally, it plays a vital role in the optical Kerr effect, which describes the change in the refractive index of a material in response to intense light. The magnitude of the second hyperpolarizability impacts the efficiency of various optical devices and is crucial in the design of materials for telecommunications and laser technology [13].

These parameters were calculated from the tensor components obtained via quantum-chemical computations.

V.5 Results and Discussion

V.5.1 Molecular Structure

The studied compound, *(E)-3-(1-(2-(9H-fluoren-9-ylidene)hydrazineyl)ethylidene)-6-methyl-2H-pyran-2,4(3H)-dione (FHP)*, is a highly conjugated organic system characterized by an extended π-electron framework. Its molecular architecture integrates an electron-rich fluorenyl moiety acting as a donor group, connected through a hydrazone linkage to a π-conjugated spacer, which is further coupled with a pyran-dione fragment functioning as an electron-withdrawing acceptor unit.

This donor–π–acceptor (D–π–A) configuration promotes efficient intramolecular charge transfer (ICT) across the molecule, which is a key requirement for enhanced nonlinear optical response. The presence of the hydrazone bridge increases conjugation and planarity, facilitating

electron delocalization throughout the system. Consequently, the structural features of FHP make it a promising candidate for nonlinear optical applications.

V.5.2 Nonlinear optical properties

The nonlinear optical (NLO) behavior of the zwitterionic Schiff base was investigated using DFT calculations. The molecular structure, characterized by a push-pull electronic system, is a well-established design strategy for enhancing NLO responses [14]. This structural motif facilitates intramolecular charge transfer (ICT), thereby increasing polarizability and hyperpolarizability, which are crucial for applications in photonic and optoelectronic devices [15].

The relationship between the molecular and electronic structures and the static and dynamic hyperpolarizabilities of the hydrazone molecule was systematically investigated using the B3LYP/6-311G(d,p) level of theory [16]. To account for solvent effects, DMSO was incorporated through an appropriate solvation model. The magnitudes of the total static dipole moment (μ), isotropic polarizability (α), and the first- and second-order hyperpolarizability parameters (β and γ) were calculated in the x, y, and z directions. This analysis provides a deeper understanding of the molecule's nonlinear optical response, known as nonlinear optical parameters, using the following equations **[17]**:

$$\mu = (\mu^2_x + \mu^2_y + \mu^2_z)^{1/2} \qquad (Eq.V.2)$$

$$\alpha = 1/3\ (\alpha_{xx} + \alpha_{yy} + \alpha_{zz}) \qquad (Eq.V.3)$$

$$\beta = [(\beta_x)^2 + (\beta_y)^2 + (\beta_z)^2\ ]^{1/2} \qquad (Eq.V.4)$$

$$\gamma = 1/5(\gamma_{xxxx} + \gamma_{yyyy} + \gamma_{zzzz} + 2\gamma_{xxyy} + 2\gamma_{xxzz} + 2\gamma_{yyzz}) \qquad (Eq.V.5)$$

The corresponding results obtained at the DFT/B3LYP level using both the 6-311G(d,p) basis set in the gas phase and the 6-311G(d,p) basis set with DMSO solvation are presented in **Table V.1**, allowing for a comparative analysis of the solvent effect on the calculated parameters. These parameters are reported in atomic units (a.u), and the calculated values have been converted into electrostatic units (esu) (α:1 a.u = 0.1482×10^{-24} esu; β: 1 a.u = 8.6393×10^{-33} esu).

V.5.3 Static NLO properties

The computed dipole moments (μ) of the molecule are measured at 3.38 Debye in the gas phase and 4.16 Debye in DMSO, indicating an increase in polarity upon solvation [18]. This enhancement underscores the stabilizing influence of the polar solvent on charge separation. For comparative purposes, similar Schiff base derivatives typically present dipole

moments ranging from 2.8 to 4.5 Debye, thereby positioning both values within the anticipated range for nonlinear optical (NLO) active materials, with the solvated form exhibiting a more pronounced polar character [19]. The static isotropic polarizability α(0;0) is 6.26×10^{-23} esu, indicating a considerable electronic cloud deformability. The calculated isotropic polarizability ($\alpha = 6.23 \times 10^{-23}$ esu) is substantially greater than that of typical organic chromophores, such as para-nitroaniline (PNA), which demonstrates $\alpha \approx 40 \times 10^{-24}$ esu. This elevated value suggests that the hydrazone molecule exhibits a highly delocalized electronic distribution, thereby facilitating enhanced molecular polarization in response to an external electric field. The increased polarizability can be attributed to the extended π-conjugation and the presence of heteroatoms within the molecular framework, both of which promote more significant charge-transfer interactions and thereby enhance the nonlinear optical response of the system [20]. The first-order static hyperpolarizability β(0;0,0) is calculated as 42.51×10^{-28} esu, which is significantly higher than that of PNA ($\beta \approx 7.2 \times 10^{-30}$ esu) and comparable to other highly conjugated Schiff base derivatives reported in the literature [21]. Such values suggest efficient charge transfer characteristics and strong NLO potential under static. The second-order hyperpolarizability γ(0,0,0,0) demonstrates a significant solvent dependency, increasing from 111.85×10^{-36} esu in the gas phase to 425.51×10^{-36} esu. This notable enhancement indicates a more robust third-order nonlinear optical (NLO) response under solvation conditions. In comparison, similar Schiff-base-type NLO materials typically exhibit γ values within the range of $80–150 \times 10^{-36}$ esu, positioning the gas-phase value within the customary interval. Conversely, the value obtained in the solvated state clearly surpasses this range, underscoring the substantial impact of the solvent in augmenting the third-order NLO characteristics of the molecule [22].

V.5.4 Dynamic NLO properties

As can be shown in Table V.1, the dynamic first-order hyperpolarizability β(–ω;ω;0) is elevated to 2.93×10^{-28} esu. The calculated static first-order hyperpolarizability ($\beta = 42.51 \times 10^{-28}$ esu) is higher than the dynamic value ($\beta = 2.93 \times 10^{-28}$ esu). The decline in β at the dynamic frequency suggests that the nonlinear optical response of the hydrazone molecule diminishes when subjected to an oscillating electric field. This reduction can be associated with restricted electronic polarization and slower charge-transfer processes at elevated frequencies. The second-order dynamic hyperpolarizability, denoted as γ(–ω; ω; 0; 0), demonstrates a significant dependence on solvent environment, exhibiting an increase from 1148.18×10^{-36} esu in the gas

phase to 4160.55 × 10^{-36} esu when using a solvent. This notable enhancement under solvent conditions underscores the compound's considerable potential for third-order nonlinear optical (NLO) applications. The elevated dynamic γ values further substantiate its applicability in areas such as optical limiting, the dc-Kerr effect, and other frequency-dependent NLO processes [23].

V.5.5 Anisotropic contributions

By considering the anisotropic contributions of NLO parameters, directional analysis reveals that the molecular β_z and γ_{xxxx} tensor components dominate, indicating that charge transfer occurs primarily along the molecular backbone. This anisotropy supports the conclusion that the molecular framework facilitates efficient delocalization and ICT along the x- and z-axes. Moreover, the computed anisotropy of polarizability Δα (3.05× 10^{-23} esu) and the significant increase in β and γ suggest that the molecule could be effectively aligned in thin films or bulk media to maximize optical response, a crucial factor in materials design for nonlinear optical devices.

Table V. 1. The static/dynamic polarizability, anisotropy of polarizability, first-order hyperpolarizability, and second-order hyperpolarizability for FHP obtained by B3LYP/6-311G(d.p) level of theory.

Parameters	6-311G (d,p) with solvent		6-311G (d,p)	
	Static	**Dynamic**	**Static**	**Dynamic**
Dipole moment				
μ_x	2.83		0	
μ_y	3.01		0	
μ_z	-0.03		3.38	
μ (D)	4.16		3.38	
Polarizability	α(0;0)	α(- ω ; ω)	α(0;0)	α(- ω ; ω)
α_{xx}	5.30	5.82	4.51	5.54
α_{yy}	5.19	5.45	2.42	2.72
α_{zz}	8.30	9.60	5.63	7.50
α (au)	422.44	469.37	282.54	280.84
α × 10^{-23} (esu)	6.26	6.95	4.18	5.25
Δα (10^{-23} (esu))	3.05	3.98	2.82	4.16
First-order hyperpolarizability	β(0,0,0)	β(-ω,ω,0)	β(0,0,0)	β(-ω,ω,0)
β_x	-23.33	-1.56	-9.69	-7.66
β_y	-17.50	-1.27	-6.89	-4.04
β_z	30.91	2.14	1.47	-2.82
β (au)	4930.84	34022.71	2190.54	10031.45
β × 10^{-28} (esu)	42.51	2.93	0.18	0.86
Second-order hyperpolarizability	γ(0,0,0,0)	γ(- ω,ω,0,0)	γ(0,0,0,0)	γ(- ω,ω,0,0)
γ_{xxxx}	207	780	90	346
γ_{yyyy}	184.98	584.74	9.18	28.59
γ_{zzzz}	550.55	2797.2	188.03	1107
γ_{xxyy}	184.55	634.72	25.29	95.87

γ_{xxzz}	217.72	1086.70	86.38	452.52
γ_{yyzz}	190.48	839.70	24.32	117.37
$\gamma \times 10^{-36}$ (esu)	425.51	4160.55	111.85	1148.18

V.6 Conclusion

In this chapter, the nonlinear optical (NLO) properties of the hydrazone-based Schiff base compound were systematically investigated using the DFT/B3LYP/6-311G(d,p) method in both the gas phase and DMSO solvent environment. The obtained results demonstrated that the molecular structure possesses a pronounced donor–π–acceptor architecture, which promotes efficient intramolecular charge transfer (ICT) and enhances the electronic polarization of the system. The calculated dipole moment, polarizability, and hyperpolarizability values revealed a significant NLO response, particularly in the presence of solvent effects. The increase in the dipole moment and hyperpolarizability parameters in DMSO confirms that the polar medium stabilizes charge separation and strengthens the nonlinear optical behavior of the molecule. Furthermore, the large first-order hyperpolarizability (β) and second-order hyperpolarizability (γ) values indicate that the studied compound exhibits stronger NLO activity than many conventional organic chromophores, highlighting its potential as an efficient NLO material. The analysis of the tensor components showed that the charge transfer mainly occurs along the molecular backbone, confirming the important role of π-conjugation and molecular anisotropy in the enhancement of the optical response. In addition, the dynamic NLO calculations revealed a considerable frequency-dependent behavior, suggesting that the compound may be suitable for third-order NLO applications such as optical switching, optical limiting, and photonic devices. Overall, the theoretical investigation confirms that the studied Schiff base derivative possesses promising nonlinear optical characteristics and could be considered a potential candidate for future optoelectronic and photonic applications.

Bibliographic references

[1] F. Adams, C. Barbante, Nanotechnology and Analytical Chemistry, in: 2015: pp. 125–157. https://doi.org/10.1016/B978-0-444-63439-9.00004-9.
[2] N. Moroney, L. Del Bino, S. Zhang, M.T.M. Woodley, L. Hill, T. Wildi, V.J. Wittwer, T. Südmeyer, G.-L. Oppo, M.R. Vanner, A Kerr polarization controller, Nat. Commun. 13 (2022) 398.
[3] Lesson Explainer: Spontaneous and Stimulated Emission | Nagwa, (n.d.). https://www.nagwa.com/en/explainers/378138614013/ (accessed February 7, 2024).
[4] A.V. Durrant, Some basic properties of stimulated and spontaneous emission: A semiclassical approach, Am. J. Phys. 44 (1976) 630–635.
[5] 7.1: Absorption, Spontaneous Emission, Stimulated Emission, Eng. Libr. (2020). https://eng.libretexts.org/Bookshelves/Electrical_Engineering/Electro-

Optics/Direct_Energy_(Mitofsky)/07%3A_Lamps%2C_LEDs%2C_and_Lasers/7.01%3A_Absorption%2C_Spontaneous_Emission%2C_Stimulated_Emission (accessed February 7, 2024).
[6] Matthew Parry-Hill, Robert T. Sutter, Thomas J. Fellers and Michael W. Davidson, Spontaneous and Stimulated Processes - Java Tutorial | Olympus LS, (n.d.). https://www.olympus-lifescience.com/en/microscope-
[7] P.A. Franken, J.F. Ward, Optical Harmonics and Nonlinear Phenomena, Rev. Mod. Phys. 35 (1963) 23–39. https://doi.org/10.1103/RevModPhys.35.23.
[8] R.M. Asath, T.N. Rekha, S. Premkumar, T. Mathavan, A.M.F. Benial, Vibrational, spectroscopic, molecular docking and density functional theory studies on N -(5-aminopyridin-2-yl)acetamide, J. Mol. Struct. 1125 (2016) 633–642. https://doi.org/10.1016/j.molstruc.2016.07.064
[9] M. Yıldız, H. Ünver, D. Erdener, A. Kiraz, N. Ocak İskeleli, Synthesis, Spectroscopic studies and crystal structure of (E)-2-(2,4-dihydroxybenzylidene) thiosemicarbazone and (E)-2-[(1H-indol-3-yl)methylene] thiosemicarbazone, J. Mol. Struct. 919(1–3), (2009) 227–234. https://doi.org/10.1016/j.molstruc.2008.09.008
[10] C. Valverde, R. Medeiros, L.R. Franco, F.A. Osório, M.A. Castro, T.L. Fonseca, Theoretical investigation on the linear and nonlinear optical properties of DAPSH crystal, Sci. Rep. 13 (2023) 8616.
[11] G. Le Breton, O. Bonhomme, E. Benichou, C. Loison, First hyperpolarizability of water in the bulk phase: long-range electrostatic effects included via the second hyperpolarizability, (2022).
[12] B. Raaghul, M.R. Kannan, T. Vijayakumar, First Order Hyper polarizability and Intramolecular Charge Transfer of N-Ethyl-N-(2-Hydroxyethyl)-4-(4-Nitrophenylazo) Aniline for Photonic Applications, in: IOP Conf. Ser. Mater. Sci. Eng., IOP Publishing, 2022: p. 012035.
[13] Amina Lahouali Dit Yahyaoui, Mohammed Hadj Mortada Belhachemi, Amine Ould Rabah, Khayra Hammou, Latifa Bensassi, Abdelkader Chouaih, Merzouk Saidj, Ömer Tamer, Davut Avcı, Yusuf Atalay, DFT-based investigation of structural, optoelectronic and molecular docking analysis of thiosemicarbazone derivatives, Next Materials, Volume 10, 2026, 101391, ISSN 2949-8228, https://doi.org/10.1016/j.nxmate.2025.101391.
[14] Harmankaya, A., Medetalibeyoğlu, H., Ortaakarsu, A.B., Atalay, A., Manap, S., Koca, E., Yıldız, Ç., Köçek, N., and Yüksek, H., *J. Mol. Struct*., 2025, vol. 1338, p. 142286.
[15] Guerraoui, A., Djedouani, A., Jeanneau, E., Boumaza, A., Alsalme, A., Zarrouk, A., Salih, K.S.M., and Warad, I., *J. Mol. Struct*., 2020, vol. 1220, p. 128728.

[16] Tahir, M., Aftab, H., Shafiq, I., Khalid, M., Haq, S., El-kott, A.F., Zein, M.A., Hani, U., and Shafiq, Z., *RSC Adv*., 2024, vol. 14, no. 6, p. 4221.
[17] Avcı, D., *Spectrochim. Acta A Mol. Biomol. Spectrosc*., 2011, vol. 82, p. 37.
[18] Poonam, R., Ram Niwas, S., Anshu, G., Mukesh, K., Riya, S., Poonam, B., *ACS Omega,* 2022, vol. 7, no. 34, p. 29571.
[19] Yadav, A., Kaushik, C.P., and Kumar, M., *J. Mol. Struct*., 2023, vol. 1283, p. 135163.
[20] Kabé, C.G., Ottou Abe, M.T., Bouba, M.O., Kabé, C., Nya, F.T., and Ndjaka, J.M., *Mater. Sci. Semicond. Process*., 2024, vol. 180, p. 108583.
[21] Avcı, D., Özge, Ö., Sönmez, F., Başoğlu, A., Tamer, Ö., and Atalay, Y., *Mater. Sci. Semicond. Process*., 2024, vol. 179, p. 108523.
[22] Fatima, Z., Basha, H.A., and Khan, S.A., *J. Mol. Struct*., 2023, vol. 1292, p. 136062.
[23] Anwar, A., Nadeem, S., Usman Khan, M., Rizwan, H.A., Al-Shaalan, N.H., Alharthi, S., and Amin, M.A., *J. Mol. Liq*., 2025, vol. 434, p. 128013.

CHAPTER VI

Electrochemical Methods and Photovoltaic Application

VI.1 Introduction 102
VI.2 Experimental Electrochemical Analysis 103
VI.3 Cyclic Voltammetry Measurements 104
VI.4 Determination of HOMO and LUMO Energy Levels 106
VI.5 Electrochemical Behavior of the Studied Compound 107
VI.6 Photovoltaic Properties 107
VI.7 Calculation of Photovoltaic Parameters 108
VI.8 Evaluation of Voc, FF and PCE 109
VI.9 Photovoltaic Performance with Different Donors 110
VI.10 Theoretical and Experimental Energy Level Analysis 111
VI.11 Conclusion 113
Bibliographic references 113

VI.1 Introduction

The investigation of electrochemical and photovoltaic properties of organic semiconducting materials has become an important research field due to the growing demand for efficient, low-cost, and environmentally friendly optoelectronic devices [1,15]. Organic compounds containing conjugated π-electron systems and donor–acceptor architectures exhibit remarkable electronic characteristics, including tunable energy levels, efficient charge-transfer ability, and favorable optical responses, which make them promising candidates for photovoltaic and electronic applications [16,31]. Among these materials, hydrazone and Schiff base derivatives have attracted particular attention because of their structural flexibility, strong intramolecular charge transfer, and excellent electrochemical activity [13].

Electrochemical characterization provides valuable information concerning oxidation–reduction behavior, charge-transfer processes, and frontier molecular orbital energies of organic compounds [1]. In particular, cyclic voltammetry is widely employed to determine the HOMO and LUMO energy levels, which are fundamental parameters governing the semiconducting and photovoltaic behavior of molecular systems [2]. The energetic alignment between HOMO and LUMO levels directly influences charge separation efficiency, electron mobility, and photovoltaic performance in donor–acceptor solar-cell devices [18].

In addition to electrochemical investigations, the evaluation of photovoltaic parameters such as open-circuit voltage (V_{oc}), fill factor (FF), and power conversion efficiency (PCE)is essential for assessing the applicability of organic materials in photovoltaic systems [19]. Theoretical calculations combined with experimental electrochemical measurements provide a comprehensive understanding of the electronic structure and charge-transfer properties of the investigated molecules [26].

Therefore, this chapter aims to investigate the electrochemical and photovoltaic applications of the studied hydrazone derivative through cyclic voltammetry measurements and theoretical analysis. The HOMO and LUMO energy levels were experimentally determined and compared with theoretical results. Furthermore, photovoltaic parameters including V_{oc}, FF, and PCEwere evaluated using different donor materials in order to assess the photovoltaic potential of the investigated compound. The obtained results provide important insight into the relationship between molecular electronic structure and photovoltaic performance.

VI.2 Experimental Electrochemical Analysis

Electrochemical analysis represents one of the most powerful experimental techniques for investigating the electronic structure, charge-transfer ability, and redox behavior of organic semiconducting materials. In conjugated donor–acceptor systems, electrochemical measurements provide valuable information concerning electron mobility, oxidation–reduction processes, and the energetic positions of frontier molecular orbitals, which are directly related to photovoltaic and optoelectronic performance **[1,2].** In the present work, the electrochemical properties of the investigated hydrazone derivative were studied using a Voltalab potentiostat–galvanostat system in a conventional three-electrode configuration comprising a platinum disk as the working electrode, a platinum wire as the counter electrode, and a saturated calomel electrode (SCE) as the reference electrode. The measurements were carried out in acetonitrile solution containing 0.1 M tetrabutylammonium tetrafluoroborate (Bu4NPF6) as the supporting electrolyte under a nitrogen atmosphere at room temperature to minimize oxygen interference and ensure electrochemical stability **[3].**

Electrochemical characterization is particularly important for organic photovoltaic materials because the oxidation and reduction potentials can be directly correlated with the HOMO and LUMO energy levels (**Figure VI.1**). These energy levels govern the electron-donating and electron-accepting abilities of the molecule and strongly influence the efficiency of charge separation processes in solar-cell devices **[4]**. The electrochemical data reveal that the studied compound exhibits pronounced electroactivity, indicating the presence of an extended π-conjugated system that facilitates intramolecular charge transfer. Such behavior is characteristic of semiconducting organic molecules containing donor and acceptor moieties interconnected through conjugated bridges **[5]**. Therefore, the electrochemical investigation confirms the suitability of the synthesized hydrazone derivative for potential applications in optoelectronic and photovoltaic systems.

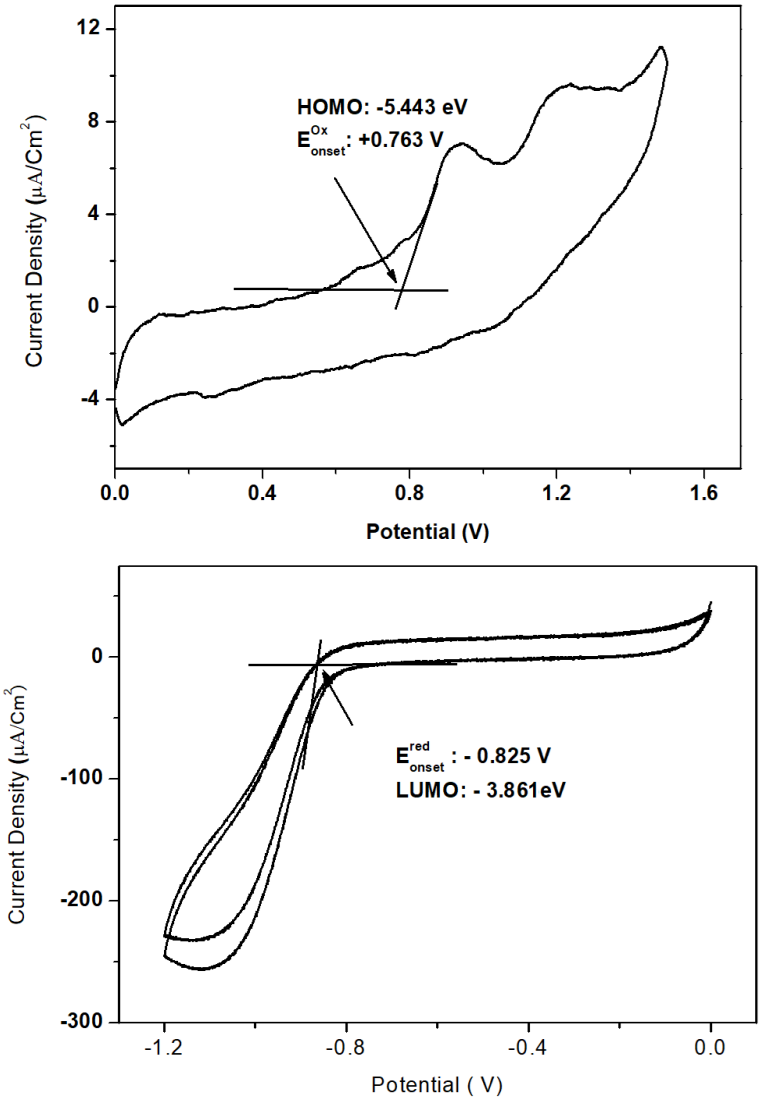


Figure VI.1. CV enregistred in MECN/ 0.1 M Bu_4NPF_6 for oxidation (Top) and for reduction (Bottom) [12.5 10^{-4}M], Sweep-rate: 100 mV/s, working electrode: platinum disk, diameter 1 mm.

VI.3 Cyclic Voltammetry Measurements

Cyclic voltammetry (CV) is a widely employed electrochemical method used to investigate oxidation and reduction phenomena occurring at the electrode–electrolyte interface. This technique provides important information regarding electron-transfer kinetics, reversibility of electrochemical reactions, and the electronic communication between molecular fragments **[6].** In the present study, the cyclic voltammograms of the investigated hydrazone derivative exhibited two irreversible anodic oxidation peaks located at approximately 0.93 V and 1.22 V versus SCE, together with one irreversible cathodic reduction peak observed in the negative potential region.

The first oxidation process is attributed to the oxidation of the oxygen atom due to the presence of nonbonding electron pairs, whereas the second anodic peak corresponds to the

oxidation of the azomethine (C=N) functional group [7]. The reduction peak observed in the cathodic scan is associated with the reduction of the imine moiety and reflects the electron-accepting ability of the molecule. The irreversible character of the oxidation and reduction processes suggests that electron transfer is accompanied by structural reorganization and possible formation of unstable intermediate species during the electrochemical reaction [8].

The redox behavior of the molecule can be represented by the following simplified oxidation and reduction processes:

$$M + e^- \rightarrow M^- \qquad \textbf{(Eq. VI.1)}$$

$$M \rightarrow M^+ + e^- \qquad \textbf{(Eq. VI.2)}$$

The observed electrochemical response demonstrates strong donor–acceptor interactions within the conjugated molecular structure. The presence of heteroatoms such as oxygen and nitrogen contributes significantly to charge delocalization and stabilization of oxidized and reduced species. Furthermore, the relatively low oxidation potential indicates that the molecule can easily donate electrons, which is a desirable characteristic for organic semiconductors and photovoltaic materials [9]. Consequently, the cyclic voltammetry results confirm the efficient charge-transfer properties and electrochemical stability of the investigated compound.

In order to better understand the electronic behavior of the investigated compound, global reactivity descriptors derived from electrochemical measurements were analyzed. The results reveal a relatively high HOMO energy level (−5.44 eV) together with a low LUMO energy level (−3.86 eV), leading to a small energy gap of 1.58 eV. This narrow gap suggests an efficient intramolecular charge transfer and enhanced electronic delocalization within the conjugated framework.

In addition, the calculated ionization potential (5.44 eV) indicates a facile electron-donating ability, while the electron affinity (3.86 eV) reflects a significant tendency to accept electrons, confirming the ambipolar character of the molecule. The low chemical hardness (η = 0.79 eV) further supports the high reactivity and softness of the system, which is favorable for organic semiconductor applications. Moreover, the high electrophilicity index (ω = 13.68 eV) highlights the strong ability of the compound to stabilize additional electronic charge.

Overall, these electrochemical descriptors confirm the pronounced charge-transfer character and good electronic adaptability of the studied compound, consistent with its potential use in optoelectronic and photovoltaic devices.

VI.4 Determination of HOMO and LUMO Energy Levels

The frontier molecular orbitals, namely the highest occupied molecular orbital (HOMO) and the lowest unoccupied molecular orbital (LUMO), constitute fundamental parameters for understanding the electronic and photovoltaic properties of organic materials [10]. The HOMO energy level reflects the electron-donating capability of the molecule, while the LUMO energy level describes its electron-accepting ability. The energy difference between these orbitals, commonly referred to as the band-gap energy (E_g), determines the ease of electronic excitation and strongly influences the optical and photovoltaic behavior of the material [11].

In the present work, the HOMO and LUMO energy levels were experimentally estimated from the onset oxidation and reduction potentials obtained from cyclic voltammetry measurements using the empirical equations proposed by Jenekhe et al. [12]:

$$E_{LUMO} = -(E_{red}^{onset} + 4.68)\ \text{eV} \qquad \textbf{(Eq. VI.3)}$$

$$E_{HOMO} = -(E_{ox}^{onset} + 4.68)\ \text{eV} \qquad \textbf{(Eq. VI.4)}$$

The electrochemical energy gap was calculated according to:

$$E_g^{el} = | E_{HOMO} - E_{LUMO} | \qquad \textbf{(Eq. VI.5)}$$

The experimental HOMO and LUMO energy levels were found to be −5.44 eV and −3.86 eV, respectively, resulting in an electrochemical band-gap energy of 1.58 eV. The relatively low energy gap indicates strong π-electron delocalization and efficient intramolecular charge transfer within the molecular backbone [13]. Such characteristics are highly desirable for organic photovoltaic applications because narrow band-gap materials generally exhibit enhanced light absorption and improved charge transport properties [14].

Moreover, the low HOMO level suggests good oxidative stability of the molecule, whereas the low LUMO energy level facilitates electron injection and electron-accepting behavior. These results demonstrate that the investigated hydrazone derivative possesses suitable electronic characteristics for semiconducting and photovoltaic applications. The obtained experimental energy levels also show reasonable agreement with theoretical DFT calculations, confirming the reliability of both experimental and computational approaches.

VI.5 Electrochemical Behavior of the Studied Compound

The electrochemical behavior of conjugated organic compounds is strongly influenced by their molecular geometry, donor–acceptor interactions, and electron density distribution [15]. In donor–acceptor systems, the presence of electron-rich and electron-deficient fragments promotes intramolecular charge transfer, which significantly affects the oxidation and reduction properties of the material [16]. The investigated hydrazone derivative exhibited pronounced electrochemical activity characterized by irreversible oxidation and reduction processes associated with the hydroxyl and azomethine groups.

The electrochemical band-gap value obtained experimentally confirms the semiconducting nature of the compound and demonstrates efficient electronic communication throughout the π-conjugated framework. The presence of nitrogen and oxygen heteroatoms contributes to the stabilization of charged intermediates formed during oxidation and reduction processes. In addition, the conjugated molecular structure facilitates electron delocalization, thereby reducing the energy required for electronic excitation [17].

The electron-transfer process occurring within the molecule may be represented schematically as follows:

$$\mathbf{D - \pi - A \rightarrow D^{+} - \pi - A^{-}} \qquad \textbf{(Eq.VI.6)}$$

where $D\ represents$ the electron donor fragment and A corresponds to the electron acceptor fragment. The efficient donor–acceptor interaction promotes charge separation and facilitates electron mobility within the molecular structure. Such properties are essential for improving the performance of organic photovoltaic and optoelectronic devices **[18].**

Furthermore, the experimental electrochemical findings are consistent with the theoretical DFT calculations, which predicted strong charge-transfer characteristics and favorable frontier orbital overlap. The agreement between theoretical and experimental approaches confirms the reliability of the electronic structure analysis and demonstrates the potential applicability of the investigated molecule in organic semiconducting materials and photovoltaic systems [19].

VI.6 Photovoltaic Properties

Organic photovoltaic (OPV) materials have attracted considerable attention due to their lightweight nature, low fabrication cost, mechanical flexibility, and tunable electronic properties [20]. The performance of organic solar cells mainly depends on the energetic alignment between donor and acceptor materials, charge-transfer efficiency, and the ability of

the active layer to facilitate exciton dissociation and charge transport [21]. In donor–acceptor systems, the transfer of electrons from the donor HOMO level toward the acceptor LUMO level plays a crucial role in determining photovoltaic efficiency.

In the present study, the investigated hydrazone derivative was evaluated as an electron-acceptor material combined with several donor compounds, namely anthracene, tetracene, and pentacene. The molecular system exhibits a conjugated π-electron framework and electron-withdrawing functional groups, which enhance intramolecular charge transfer and improve electron mobility. Such characteristics are highly favorable for organic photovoltaic applications because efficient charge separation reduces recombination losses and promotes photocurrent generation [22].

The photovoltaic mechanism occurring in donor–acceptor systems can be summarized as follows:

$$D + A + h\nu \rightarrow D^{+} + A^{-} \qquad \textbf{(Eq. VI.7)}$$

where D represents the donor molecule, A, the acceptor molecule, and $h\nu$ the absorbed photon energy. Upon light absorption, excitons are generated and subsequently dissociated at the donor–acceptor interface, leading to charge separation and electrical current generation [23].

The obtained results indicate that the studied hydrazone derivative possesses favorable frontier orbital alignment and efficient charge-transfer capability, confirming its suitability as an acceptor material for organic photovoltaic devices.

VI.7 Calculation of Photovoltaic Parameters

The photovoltaic performance of organic solar cells is generally evaluated using several important parameters, including the open-circuit voltage (V_{oc}), fill factor (FF), short-circuit current density (J_{sc}), and power conversion efficiency (PCE) [24]. These parameters provide information regarding the electrical quality of the photovoltaic system and the effectiveness of charge separation and transport processes.

The open-circuit voltage was estimated using the empirical relationship proposed by Scharber et al. [25]:

$$V_{oc} = \frac{1}{e}\left(\left| E_{HOMO}^{Donor} \right| - \left| E_{LUMO}^{Acceptor} \right|\right) - 0.3 \qquad \textbf{(Eq. VI.8)}$$

where E_{HOMO}^{Donor} corresponds to the HOMO energy level of the donor material, $E_{LUMO}^{Acceptor}$ represents the LUMO energy level of the acceptor molecule, and 0.3 eV accounts for empirical energy losses occurring during charge-transfer processes.

The fill factor (FF), which reflects the electrical quality of the photovoltaic device, was calculated using:

$$FF = \frac{\frac{eV_{oc}}{k_BT} - \ln\left(\frac{eV_{oc}}{k_BT} + 0.72\right)}{\frac{eV_{oc}}{k_BT} + 1} \qquad \textbf{(Eq. VI.9)}$$

The power conversion efficiency was determined from:

$$PCE = \frac{J_{SC}V_{oc}FF}{P_{in}} \qquad \textbf{(Eq. VI.10)}$$

where J_{sc} is the short-circuit current density and P_{in} is the incident light power. The calculated photovoltaic parameters demonstrate that the investigated hydrazone derivative exhibits promising photovoltaic behavior characterized by relatively high V_{oc} and FF values. These findings indicate efficient donor–acceptor charge separation and reduced charge recombination effects within the active layer **[26].**

VI.8 Evaluation of Voc, FF and PCE

The open-circuit voltage (V_{oc}), fill factor (FF), and power conversion efficiency (PCE) are considered fundamental indicators for evaluating the effectiveness of photovoltaic materials **[27].** High V_{oc} values generally indicate efficient energetic alignment between donor and acceptor materials, whereas high FF values reflect reduced electrical losses and improved charge transport characteristics **[28].**

In the present work, the calculated theoretical V_{oc} values ranged from 1.88 eV to 2.51 eV depending on the donor material employed, while the experimental values varied between 1.13 eV and 1.53 eV. The lower experimental values compared to theoretical predictions can be attributed to charge recombination effects, intermolecular interactions, and energy losses occurring at donor–acceptor interfaces under practical operating conditions **[29]**.

The fill factor values remained relatively high, ranging between 89% and 94%, indicating favorable charge transport properties and good electrical quality of the investigated donor–acceptor systems. Similarly, the calculated power conversion efficiencies ranged from 8.45% to 19.84%, with the anthracene/FHP system exhibiting the highest efficiency among the investigated donor materials.

The superior photovoltaic performance observed for anthracene can be explained by its favorable HOMO energy level alignment with the LUMO level of the investigated acceptor molecule. This energetic compatibility enhances charge separation efficiency and minimizes electron–hole recombination losses [30]. Therefore, the obtained results demonstrate that the investigated hydrazone derivative possesses promising photovoltaic characteristics suitable for organic solar-cell applications.

VI.9 Photovoltaic Performance with Different Donors

The photovoltaic efficiency of donor–acceptor systems strongly depends on the electronic compatibility between the donor and acceptor materials [31]. Appropriate energetic alignment facilitates exciton dissociation, charge separation, and electron transport, thereby improving the overall photovoltaic performance of the device (**Figures VI.2 and VI.3**).

In this work, anthracene, tetracene, and pentacene were investigated as donor materials combined with the studied hydrazone acceptor. The obtained theoretical and experimental results reveal that the anthracene/FHP interface exhibited the highest V_{oc}, FF, and PCEvalues compared to tetracene and pentacene systems. This behavior can be attributed to the optimal energetic difference between the HOMO level of anthracene and the LUMO level of the acceptor molecule, which facilitates efficient electron transfer and charge separation [32].

By contrast, pentacene exhibited lower photovoltaic performance due to less favorable frontier orbital overlap and increased recombination losses. The comparative study clearly demonstrates that the nature of the donor material significantly influences the photovoltaic response of the investigated system.

The charge-transfer interaction between donor and acceptor materials may be represented as:

$$D^* + A \rightarrow D^+ + A^- \qquad \textbf{(Eq. VI.11)}$$

where D^*represents the excited donor species generated after photon absorption. Efficient charge transfer from donor to acceptor is essential for improving photocurrent generation and overall device efficiency [33].

Therefore, the obtained results confirm that anthracene represents the most suitable donor material among the investigated systems for enhancing the photovoltaic performance of the studied hydrazone derivative.

VI.10 Theoretical and Experimental Energy Level Analysis

The comparison between theoretical and experimental energy levels provides important insight into the electronic structure and charge-transfer behavior of organic semiconducting materials [34]. Density Functional Theory (DFT) calculations describe the intrinsic electronic properties of isolated molecules in the gas phase, whereas experimental electrochemical measurements reflect the influence of solvent effects, intermolecular interactions, and environmental stabilization [35].

In the present study (Table VI.1), the theoretical HOMO–LUMO energy gap was calculated to be approximately 3.5 eV, whereas the experimental electrochemical band-gap value obtained from cyclic voltammetry measurements was significantly lower (1.58 eV). The reduction observed in the experimental gap can be attributed to stabilization of charged species in solution and enhanced intermolecular electronic interactions during electrochemical measurements [36].

Despite these quantitative differences, both theoretical and experimental approaches consistently confirm the donor–acceptor nature of the investigated molecule and its efficient intramolecular charge-transfer capability. The localization of the HOMO orbital over the electron-donating fragment and the LUMO orbital over the electron-accepting fragment promotes charge separation and facilitates electron transport processes.

The agreement between theoretical predictions and experimental observations validates the computational methodology employed in this study and confirms the reliability of the obtained electronic parameters. Overall, the combined theoretical and experimental investigation demonstrates that the studied hydrazone derivative possesses suitable electronic and photovoltaic characteristics for potential applications in organic photovoltaic and optoelectronic devices [37].

Table VI. 1. Calculated values of open circuit voltage (V_{oc}), Fill Factor (FF) and Energy Conversion Efficiency (PCE) for the studied molecule, with various donors.

Theoretical values							
Acceptor	**Donor**	**V_{oc} (eV)**	**Normalized V_{oc} (eV)**	**E_{LL}(eV)**	**E_{CT} (eV)**	**FF (%)**	**PCE (%)**
FHP	Anthracene	2.51	97.00	0.77	2.81	94.30	19.84
	Tetracene	2.14	82.71	0.33	2.44	93.52	16.77
	Pentacene	1.88	72.66	0.02	2.18	92.81	14.62
Experimental values							
Acceptor	**Donor**	**V_{oc} (eV)**	**Normalized V_{oc} (eV)**	**E_{LL}(eV)**	**E_{CT} (eV)**	**FF (%)**	**PCE (%)**
FHP	Anthracene	1.53	59.13	1.57	1.83	91.53	11.74
	Tetracene	1.33	51.40	1.07	1.63	90.55	10.09
	Pentacene	1.13	43.67	0.67	1.43	89.27	8.45

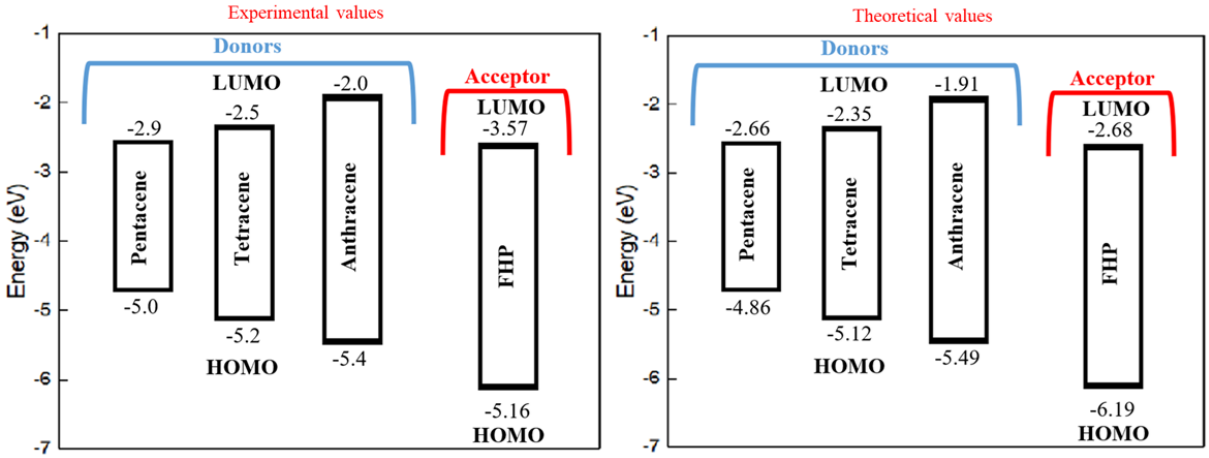


Figure VI.2. HOMO and LUMO of FHP and with different donors.

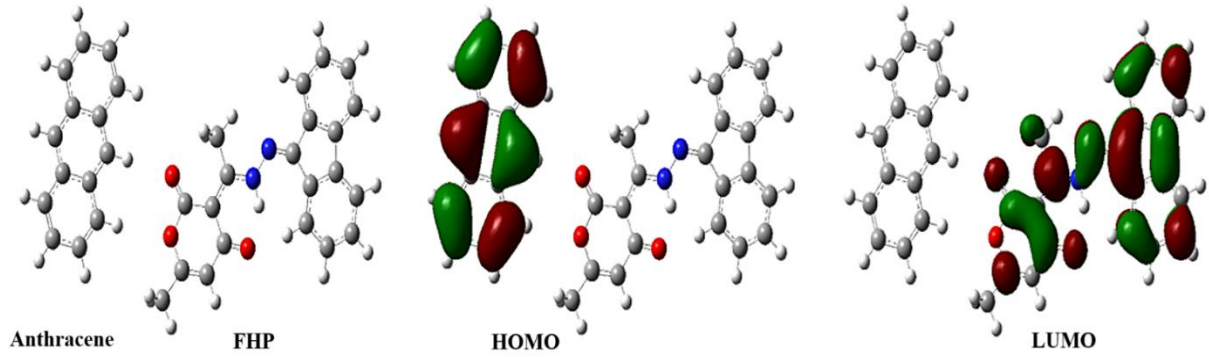


Figure VI.3. HOMO and LUMO of FHP and anthracene.

VI.11 Conclusion

In this chapter, the electrochemical and photovoltaic properties of the investigated hydrazone derivative were systematically studied using both experimental and theoretical approaches. Cyclic voltammetry measurements revealed irreversible oxidation and reduction processes associated mainly with the hydroxyl and azomethine functional groups, confirming the electroactive nature of the compound and the existence of efficient intramolecular charge-transfer interactions. The experimental electrochemical analysis allowed the determination of the HOMO and LUMO energy levels, which were found to be −5.44 eV and −3.86 eV, respectively, leading to a relatively low electrochemical band-gap value of 1.58 eV. This narrow band gap indicates enhanced π-electron delocalization and favorable semiconducting behavior suitable for optoelectronic applications. The comparison between experimental and theoretical energy levels demonstrated good qualitative agreement, despite the lower experimental band-gap value resulting from solvent effects and intermolecular interactions during electrochemical measurements. Both approaches consistently confirmed the donor–acceptor character of the investigated molecule and its efficient charge-transfer capability. The photovoltaic study showed that the investigated hydrazone derivative exhibits promising photovoltaic properties when combined with different donor materials. The calculated V_{oc}, FF, and PCE values demonstrated that the anthracene/FHP system possesses the highest photovoltaic efficiency due to favorable energetic alignment and enhanced charge separation processes. The relatively high fill factor values further indicate efficient charge transport and reduced recombination losses within the donor–acceptor interfaces. Overall, the obtained electrochemical and photovoltaic results demonstrate that the studied hydrazone derivative possesses suitable electronic properties for potential application in organic photovoltaic and optoelectronic devices. The combination of experimental electrochemical measurements and theoretical calculations provides a comprehensive understanding of the relationship between molecular structure, electronic behavior, and photovoltaic performance.

Bibliographic references

[1] Bard, A.J.; Faulkner, L.R. *Electrochemical Methods: Fundamentals and Applications*, 2nd ed.; Wiley: New York, 2001.
[2] Elgrishi, N.; Rountree, K.J.; McCarthy, B.D.; Rountree, E.S.; Eisenhart, T.T.; Dempsey, J.L. "A Practical Beginner's Guide to Cyclic Voltammetry." *Journal of Chemical Education*, 2018, 95, 197–206.
[3] Trasatti, S. "The Absolute Electrode Potential: An Explanatory Note." *Pure and Applied Chemistry*, 1986, 58, 955–966.
[4] Kulkarni, A.P.; Tonzola, C.J.; Babel, A.; Jenekhe, S.A. "Electron Transport Materials for Organic Light-Emitting Diodes." *Chemistry of Materials*, 2004, 16, 4556–4573.

[5] Patil, D.S.; Avhad, K.C.; Sekar, N. "Charge Transfer in Schiff Base Derivatives." *Computational and Theoretical Chemistry*, 2018, 1138, 75–84.
[6] Nicholson, R.S.; Shain, I. "Theory of Stationary Electrode Polarography." *Analytical Chemistry*, 1964, 36, 706–723.
[7] Enache, T.A.; Oliveira-Brett, A.M. "Phenol and Para-Substituted Phenols Electrochemical Oxidation Pathways." *Journal of Electroanalytical Chemistry*, 2011, 655, 9–16.
[8] Laviron, E. "General Expression of the Linear Potential Sweep Voltammogram in the Case of Diffusionless Electrochemical Systems." *Journal of Electroanalytical Chemistry*, 1979, 101, 19–28.
[9] Sęk, D.; Siwy, M.; Małecki, J.G.; Kotowicz, S.; Golba, S.; Nowak, E.M.; Sanetra, J.; Schab-Balcerzak, E. "Electrochemical and Optical Properties of Organic Semiconductors." *Spectrochimica Acta Part A*, 2017, 175, 168–177.
[10] Geerlings, P.; De Proft, F.; Langenaeker, W. "Conceptual Density Functional Theory." *Chemical Reviews*, 2003, 103, 1793–1874.
[11] Brédas, J.L. "Mind the Gap!" *Materials Horizons*, 2014, 1, 17–19.
[12] Jenekhe, S.A.; Lu, L. "Effects of Conjugation on Electronic Structure and Properties of Conjugated Polymers." *Macromolecules*, 1998, 31, 7315–7324.
[13] Boukabcha, N.; Direm, A.; Drissi, M.; Megrouss, Y.; Khelloul, N.; Dege, N.; Tuna, M.; Chouaih, A. "DFT and Electrochemical Investigation of Schiff Base Compounds." *Inorganic Chemistry Communications*, 2021, 133, 108884.
[14] Brabec, C.J.; Heeney, M.; McCulloch, I.; Nelson, J. "Influence of Blend Microstructure on Bulk Heterojunction Organic Photovoltaic Performance." *Chemical Society Reviews*, 2011, 40, 1185–1199.
[15] Li, G.; Zhu, R.; Yang, Y. "Polymer Solar Cells." *Nature Photonics*, 2012, 6, 153–161.
[16] Günes, S.; Neugebauer, H.; Sariciftci, N.S. "Conjugated Polymer-Based Organic Solar Cells." *Chemical Reviews*, 2007, 107, 1324–1338.
[17] Wang, Y.; Zhang, H.; Tang, G.; Zhao, J. "Theoretical Investigation of Schiff Base Photovoltaic Materials." *Computational and Theoretical Chemistry*, 2024, 1236, 114602.
[18] Scharber, M.C.; Sariciftci, N.S. "Efficiency of Bulk-Heterojunction Organic Solar Cells." *Progress in Polymer Science*, 2013, 38, 1929–1940.
[19] Scharber, M.C.; Mühlbacher, D.; Koppe, M.; Denk, P.; Waldauf, C.; Heeger, A.J.; Brabec, C.J. "Design Rules for Donors in Bulk-Heterojunction Solar Cells." *Advanced Materials*, 2006, 18, 789–794.
[20] Hoppe, H.; Sariciftci, N.S. "Organic Solar Cells: An Overview." *Journal of Materials Research*, 2004, 19, 1924–1945.
[21] Rand, B.P.; Genoe, J.; Heremans, P.; Poortmans, J. "Solar Cells Utilizing Small Molecular Weight Organic Semiconductors." *Progress in Photovoltaics*, 2007, 15, 659–676.
[22] Nelson, J. *The Physics of Solar Cells*; Imperial College Press: London, 2003.
[23] Green, M.A. *Solar Cells: Operating Principles, Technology and System Applications*; Prentice Hall: New Jersey, 1982.
[24] Koster, L.J.A.; Mihailetchi, V.D.; Blom, P.W.M. "Ultimate Efficiency of Polymer/Fullerene Bulk Heterojunction Solar Cells." *Applied Physics Letters*, 2006, 88, 093511.
[25] Frisch, M.J.; Trucks, G.W.; Schlegel, H.B.; et al. *Gaussian 09 Revision D.01*; Gaussian Inc.: Wallingford CT, 2016.
[26] Cramer, C.J. *Essentials of Computational Chemistry: Theories and Models*, 2nd ed.; Wiley: Chichester, 2004.
[27] Tamer, O.; Şimşek, M.; Avcı, D.; Atalay, Y. "Solvent Effects on Electronic Properties of Organic Molecules." *Spectrochimica Acta Part A*, 2023, 286, 122005.
[28] Becke, A.D. "Density-Functional Thermochemistry III. The Role of Exact Exchange." *Journal of Chemical Physics*, 1993, 98, 5648–5652.
[29] Lee, C.; Yang, W.; Parr, R.G. "Development of the Colle-Salvetti Correlation-Energy Formula into a Functional of the Electron Density." *Physical Review B*, 1988, 37, 785–789.
[30] Heeger, A.J. "Semiconducting Polymers: The Third Generation." *Chemical Society Reviews*, 2010, 39, 2354–2371.
[31] Brédas, J.L.; Norton, J.E.; Cornil, J.; Coropceanu, V. "Molecular Understanding of Organic Solar Cells." *Accounts of Chemical Research*, 2009, 42, 1691–1699.

[32] Clarke, T.M.; Durrant, J.R. "Charge Photogeneration in Organic Solar Cells." *Chemical Reviews*, 2010, 110, 6736–6767.
[33] Hains, A.W.; Liang, Z.; Woodhouse, M.A.; Gregg, B.A. "Molecular Semiconductors in Organic Photovoltaic Cells." *Chemical Reviews*, 2010, 110, 6689–6735.
[34] De Angelis, F.; Fantacci, S.; Selloni, A. "Alignment of the Dye's Molecular Levels with the TiO2 Band Edges in Dye-Sensitized Solar Cells." *Nanotechnology*, 2008, 19, 424002.
[35] Kohn, W.; Sham, L.J. "Self-Consistent Equations Including Exchange and Correlation Effects." *Physical Review*, 1965, 140, A1133–A1138.
[36] Parr, R.G.; Yang, W. *Density-Functional Theory of Atoms and Molecules*; Oxford University Press: New York, 1989.
[37] Coropceanu, V.; Cornil, J.; da Silva Filho, D.A.; Olivier, Y.; Silbey, R.; Brédas, J.L. "Charge Transport in Organic Semiconductors." *Chemical Reviews*, 2007, 107, 926–952.

General Conclusion

This thesis has presented a comprehensive, multidisciplinary investigation of the zwitterionic hydrazone Schiff base derivative FHP, (E)-3-(1-(2-(9H-fluoren-9-ylidene)hydrazineyl)ethylidene)-6-methyl-2H-pyran-2,4(3H)-dione, through the combined use of high-resolution X-ray crystallography, experimental electron density analysis, density functional theory (DFT) calculations, nonlinear optical characterization, electrochemical measurements, and theoretical photovoltaic assessment. The results obtained across the six chapters provide a coherent and physically rigorous picture of the relationship between the molecular structure of FHP and its electronic, optical, and photovoltaic properties.

C.1.1 Crystal Structure and Experimental Electron Density

Single-crystal X-ray diffraction analysis confirmed that FHP crystallizes in the monoclinic system (space group $P2_1/c$) and adopts the E-configuration around the azomethine C=N bond. The compound exists in the solid state as a zwitterionic keto-hydrazone tautomer, stabilized by a strong intramolecular N-H···O hydrogen bond of the N^+-H···O^- type. The three-dimensional crystal packing is governed by a network of C-H···O hydrogen bonds, C-H···π contacts, and π···π stacking interactions, which together define a well-ordered supramolecular framework [1-2].

The multipolar refinement of the high-resolution X-ray data using the Hansen-Coppens formalism implemented in MoPro provided the first experimental charge-density description of FHP. The static deformation density maps revealed clear evidence of covalent bond formation, lone-pair localization on oxygen and nitrogen atoms, and extended π-electron delocalization across the conjugated molecular framework. The QTAIM topological analysis of all bonding interactions—based on electron density values $\rho(r)$, Laplacians $\nabla^2\rho(r)$, and energy densities at bond critical points—confirmed the shared covalent nature of all intramolecular bonds and the closed-shell, electrostatic character of intermolecular contacts. The strong N2-H2 bond (ρ = 2.95 e·Å^{-3}, $\nabla^2\rho$ = -92.58 e·Å^{-5}) confirmed the polar covalent character of the hydrogen-bond donor, while the C=O and C=N interactions displayed values fully consistent with those reported for analogous hydrazone and Schiff base systems in the literature [3-5].

C.1.2 Quantum Chemical Investigation

DFT calculations at the B3LYP/6-311G(d,p) level of theory reproduced the experimental geometry of FHP with excellent fidelity, with computed bond lengths and angles deviating by less than 2% from the X-ray values. The HOMO-LUMO energy gap of approximately 3.53 eV in DMSO indicates a moderate electronic excitation energy consistent

with good chemical stability and efficient intramolecular charge transfer. The HOMO is predominantly localized over the fluorenyl donor moiety, while the LUMO is delocalized over the pyran-dione acceptor fragment, confirming the D-π-A character of the molecule and the directionality of charge transfer upon electronic excitation [6-7].

The molecular electrostatic potential surface revealed distinct nucleophilic and electrophilic regions, consistent with the presence of electron-rich oxygen lone pairs and the electron-deficient azomethine fragment. Hirshfeld surface analysis and two-dimensional fingerprint plots quantified the contributions of all intermolecular contacts to the crystal packing, with H···O/O···H and H···H contacts dominating the interaction landscape. The reduced density gradient (RDG) analysis and the electron localization function (ELF) together confirmed the non-covalent nature of the intermolecular contacts and provided a clear visualization of lone-pair basins and π-bond regions within the molecule [8].

C.1.3 Nonlinear Optical Properties

The nonlinear optical investigation of FHP demonstrated a pronounced NLO response attributable to its D-π-A molecular architecture and extended π-conjugation. The calculated static first-order hyperpolarizability β(0;0,0) of 42.51 × 10^{-28} esu significantly exceeds the benchmark value for para-nitroaniline (PNA, β ≈ 7.2 × 10^{-30} esu), demonstrating that FHP is a substantially more efficient second-order NLO chromophore. Similarly, the second-order hyperpolarizability γ(0,0,0,0) increased dramatically from 111.85 × 10^{-36} esu in the gas phase to 425.51 × 10^{-36} esu in DMSO, highlighting the significant enhancement of third-order NLO activity by polar solvation. The dominance of the β_r and γ^{xxxx} tensor components confirms that charge transfer occurs primarily along the molecular backbone, as expected for a linearly conjugated D-π-A system. The dynamic NLO calculations further revealed that the compound retains significant optical activity at finite frequencies, supporting its potential for applications in optical switching and optical limiting [9-11].

C.1.4 Electrochemical and Photovoltaic Properties

Cyclic voltammetry of FHP in acetonitrile revealed two irreversible anodic oxidation peaks at approximately 0.93 V and 1.22 V vs. SCE, attributed respectively to the oxidation of the oxygen lone pairs and the azomethine group, together with one irreversible cathodic reduction peak. From the onset potentials, the experimental HOMO and LUMO energy levels were determined to be −5.44 eV and −3.86 eV, respectively, yielding an electrochemical band gap of 1.58 eV. This narrow gap confirms strong π-electron delocalization and efficient

intramolecular charge transfer, which are prerequisites for organic semiconducting behavior [12-13].

The photovoltaic assessment of FHP as an electron-acceptor material combined with anthracene, tetracene, and pentacene donors demonstrated promising performance. The anthracene/FHP system achieved the highest theoretical power conversion efficiency (PCE = 19.84%) and open-circuit voltage (Voc = 2.51 eV), attributable to its optimal frontier orbital level alignment and efficient charge separation. The experimental PCE values (8.45-11.74%), while lower than theoretical predictions due to charge recombination and interfacial losses, confirm the genuine photovoltaic potential of FHP. The consistently high fill factor values (89-94%) further indicate favorable charge transport properties within the investigated donor-acceptor interfaces [14-15].

C.2. Scientific Significance

From a methodological perspective, this work demonstrates the power of combining experimental electron density analysis with DFT-based theoretical approaches to obtain a complete and quantitatively rigorous description of the electronic structure of a functional organic material. The agreement between the multipolar refinement results and the DFT calculations validates both methodologies and provides mutual cross-validation of the structural and electronic parameters. In particular, the experimental QTAIM analysis at the bond critical point level constitutes an especially powerful approach for unambiguously characterizing the nature of all bonding interactions, going well beyond the information accessible from conventional crystallographic refinement [16].

From the perspective of materials design, the present study demonstrates that carefully designed hydrazone Schiff base derivatives with D-π-A architecture, extended conjugation, and favorable heteroatom positioning can simultaneously satisfy the requirements for NLO activity, electrochemical stability, and photovoltaic performance. The FHP molecule exemplifies how structural features that promote intramolecular charge transfer and π-electron delocalization collectively enhance all of these optoelectronic properties, suggesting that this class of compounds offers a highly versatile platform for the development of multifunctional organic materials [17-18].

C.3. Perspectives and Future Work

The results presented in this thesis open several promising directions for future research. The following perspectives are envisaged:

- Synthesis of structurally modified FHP analogues bearing different electron-donor or electron-acceptor substituents on the fluorenyl or pyran-dione fragments could allow systematic structure-property optimization and further enhancement of NLO and photovoltaic performance.
- High-pressure and variable-temperature X-ray diffraction experiments could reveal the sensitivity of the intramolecular charge-transfer and hydrogen-bonding network to external stimuli, providing insight into the dynamic behavior of the electron density in the crystal.
- Time-dependent DFT (TD-DFT) calculations could be performed to simulate the UV-visible absorption spectrum and electronic transitions of FHP, allowing direct comparison with experimental spectroscopic data and providing deeper insight into the photophysical behavior of the compound.
- The fabrication and experimental testing of organic solar-cell devices incorporating FHP as an acceptor layer, combined with acene donor materials, would allow validation of the theoretical photovoltaic predictions and identification of efficiency-limiting factors under practical device conditions.
- Extension of the electron density study to synchrotron-quality data would allow refinement to higher multipole orders and resolution of finer charge density features, potentially revealing subtle charge-transfer pathways not accessible from conventional laboratory X-ray data.
- Molecular docking studies and biological activity assays could be performed to explore the potential of FHP and its metal complexes as bioactive compounds, leveraging the demonstrated ability of its azomethine and carbonyl groups to interact with biological macromolecules.

References

[1] Guerraoui, A.; Djedouani, A.; Jeanneau, E.; Boumaza, A.; Alsalme, A.; Zarrouk, A.; Salih, K. S. M.; Warad, I. Crystal structure and spectroscopic study of (E)-3-(1-(2-(9H-fluoren-9-ylidene)hydrazineyl)ethylidene)-6-methyl-2H-pyran-2,4(3H)-dione. Journal of Molecular Structure 2020, 1220, 128728. https://doi.org/10.1016/j.molstruc.2020.128728

[2] Boukabcha, N.; Direm, A.; Drissi, M.; Megrouss, Y.; Khelloul, N.; Dege, N.; Tuna, M.; Chouaih, A. DFT and electrochemical investigation of Schiff base compounds. Inorganic Chemistry Communications 2021, 133, 108884. https://doi.org/10.1016/j.inoche.2021.108884

[3] Espinosa, E.; Molins, E.; Lecomte, C. Hydrogen bond strengths revealed by topological analyses of experimentally observed electron densities. Chemical Physics Letters 1998, 285, 170-173. https://doi.org/10.1016/S0009-2614(98)00036-0

[4] Bader, R. F. W. A bond path: a universal indicator of bonded interactions. Journal of Physical Chemistry A 1998, 102, 7314-7323. https://doi.org/10.1021/jp981794v

[5] Hansen, N. K.; Coppens, P. Testing aspherical atom refinements on small-molecule data sets. Acta Crystallographica Section A 1978, 34, 909-921. https://doi.org/10.1107/S0567739478001886

[6] Becke, A. D. Density-functional thermochemistry. III. The role of exact exchange. Journal of Chemical Physics 1993, 98, 5648-5652. https://doi.org/10.1063/1.464913

[7] Lee, C.; Yang, W.; Parr, R. G. Development of the Colle-Salvetti correlation-energy formula into a functional of the electron density. Physical Review B 1988, 37, 785-789. https://doi.org/10.1103/PhysRevB.37.785

[8] Johnson, E. R.; Keinan, S.; Mori-Sánchez, P.; Contreras-García, J.; Cohen, A. J.; Yang, W. Revealing noncovalent interactions. Journal of the American Chemical Society 2010, 132, 6498-6506. https://doi.org/10.1021/ja100936w

[9] Lahouali Dit Yahyaoui, A. et al. DFT-based investigation of structural, optoelectronic and molecular docking analysis of thiosemicarbazone derivatives. Next Materials 2026, 10, 101391. https://doi.org/10.1016/j.nxmate.2025.101391

[10] Boyd, R. W. Nonlinear Optics, 3rd ed.; Academic Press: New York, 2008. ISBN 978-0-12-369470-6.

[11] Kanis, D. R.; Ratner, M. A.; Marks, T. J. Design and construction of molecular assemblies with large second-order optical nonlinearities. Chemical Reviews 1994, 94, 195-242. https://doi.org/10.1021/cr00025a007

[12] Bard, A. J.; Faulkner, L. R. Electrochemical Methods: Fundamentals and Applications, 2nd ed.; Wiley: New York, 2001. ISBN 978-0-471-04372-0.

[13] Elgrishi, N.; Rountree, K. J.; McCarthy, B. D.; Rountree, E. S.; Eisenhart, T. T.; Dempsey, J. L. A practical beginner's guide to cyclic voltammetry. Journal of Chemical Education 2018, 95, 197-206. https://doi.org/10.1021/acs.jchemed.7b00361

[14] Scharber, M. C.; Mühlbacher, D.; Koppe, M.; Denk, P.; Waldauf, C.; Heeger, A. J.; Brabec, C. J. Design rules for donors in bulk-heterojunction solar cells. Advanced Materials 2006, 18, 789-794. https://doi.org/10.1002/adma.200501717

[15] Brabec, C. J.; Heeney, M.; McCulloch, I.; Nelson, J. Influence of blend microstructure on bulk heterojunction organic photovoltaic performance. Chemical Society Reviews 2011, 40, 1185-1199. https://doi.org/10.1039/C0CS00045K

[16] Coppens, P. X-Ray Charge Densities and Chemical Bonding; Oxford University Press: New York, 1997. ISBN 978-0-19-509731-2.

[17] Datta, A.; Pati, S. K. Charge transfer in organic materials for nonlinear optics. Chemical Society Reviews 2006, 35, 1305-1323. https://doi.org/10.1039/B605478G

[18] Hagfeldt, A.; Boschloo, G.; Sun, L.; Kloo, L.; Pettersson, H. Dye-sensitized solar cells. Chemical Reviews 2010, 110, 6595-6663. https://doi.org/10.1021/cr900356p

Abstract / Résumé / ملخص

— English —

Structural, Electron Density, Quantum Chemical, Nonlinear Optical, Electrochemical, and Photovoltaic Investigations of the Hydrazone Schiff Base Derivative FHP

This thesis presents a comprehensive multidisciplinary investigation of the zwitterionic hydrazone Schiff base derivative (E)-3-(1-(2-(9H-fluoren-9-ylidene)hydrazineyl)ethylidene)-6-methyl-2H-pyran-2,4(3H)-dione (FHP), combining advanced experimental techniques with state-of-the-art computational methods to establish a rigorous structure–property relationship for this conjugated donor–π–acceptor (D–π–A) organic material.

FHP was synthesized by condensation of (9H-fluoren-9-ylidene)hydrazine with dehydroacetic acid and fully characterized by single-crystal X-ray diffraction, which confirmed that the compound crystallizes in the monoclinic space group $P2_1/c$ and adopts the keto-hydrazone zwitterionic tautomeric form in the solid state, stabilized by a strong intramolecular N^+–H···O^- hydrogen bond. High-resolution X-ray data were subjected to multipolar electron density refinement based on the Hansen–Coppens formalism using the MoPro software. The Quantum Theory of Atoms in Molecules (QTAIM) topological analysis of the experimental electron density provided a physically rigorous characterization of all covalent bonds, non-covalent contacts, and intermolecular interactions in the crystal.

Density functional theory (DFT) calculations at the B3LYP/6-311G(d,p) level reproduced the experimental geometry with excellent fidelity and were used to investigate the frontier molecular orbitals, global chemical reactivity descriptors, molecular electrostatic potential, Hirshfeld surface analysis, reduced density gradient (RDG), electron localization function (ELF), and localized orbital locator (LOL). The HOMO–LUMO energy gap of 3.53 eV and the donor–acceptor orbital topology confirm the pronounced intramolecular charge-transfer character of FHP.

The nonlinear optical (NLO) properties were evaluated at the same DFT level in both the gas phase and DMSO solution. The computed static first-order hyperpolarizability $\beta(0;0,0) = 42.51 \times 10^{-28}$ esu significantly exceeds the benchmark value for para-nitroaniline (PNA), confirming FHP as a promising second-order NLO chromophore. The second-order hyperpolarizability γ increased from 111.85×10^{-36} esu (gas phase) to 425.51×10^{-36} esu (DMSO), highlighting the solvent enhancement of third-order NLO activity.

Electrochemical characterization by cyclic voltammetry in acetonitrile yielded experimental HOMO and LUMO energy levels of −5.44 eV and −3.86 eV, respectively, with an electrochemical band gap of 1.58 eV, in good agreement with DFT predictions. Theoretical photovoltaic assessment of FHP as an electron-acceptor material combined with anthracene, tetracene, and pentacene donors gave power conversion efficiencies (PCE) reaching 19.84% (theoretical) and 11.74% (experimental), with fill factors of 89–94%, confirming the genuine potential of FHP for organic photovoltaic applications.

Keywords: *Schiff base; hydrazone; FHP; X-ray diffraction; multipolar refinement; QTAIM; DFT; B3LYP; intramolecular charge transfer; nonlinear optics; hyperpolarizability; cyclic voltammetry; organic photovoltaics; HOMO–LUMO.*

— Français —

Investigations Structurale, Densité Électronique, Chimie Quantique, Optique Non Linéaire, Électrochimique et Photovoltaïque du Dérivé Hydrazone Base de Schiff FHP

Ce travail de thèse présente une investigation multidisciplinaire et approfondie du dérivé hydrazone base de Schiff zwitterionique (E)-3-(1-(2-(9H-fluorén-9-ylidène)hydrazinéyl)éthylidène)-6-méthyl-2H-pyrane-2,4(3H)-dione (FHP), en combinant des techniques expérimentales avancées et des méthodes computationnelles de pointe afin d'établir une relation structure–propriétés rigoureuse pour ce matériau organique conjugué à architecture donneur–π–accepteur (D–π–A).

Le composé FHP a été synthétisé par condensation de la (9H-fluorén-9-ylidène)hydrazine avec l'acide déshydroacétique et entièrement caractérisé par diffraction des rayons X sur monocristal, confirmant que le composé cristallise dans le groupe d'espace monoclinique $P2_1/c$ sous la forme tautomère kéto-hydrazone zwitterionique stabilisée par une liaison hydrogène intramoléculaire forte $N^+–H\cdots O^-$. Les données à haute résolution ont permis de réaliser un affinement multipolaire de la densité électronique selon le formalisme Hansen–Coppens (logiciel MoPro). L'analyse topologique QTAIM de la densité électronique expérimentale a fourni une caractérisation physiquement rigoureuse de toutes les liaisons covalentes, des contacts non covalents et des interactions intermoléculaires dans le cristal.

Les calculs DFT au niveau B3LYP/6-311G(d,p) ont reproduit avec excellente fidélité la géométrie expérimentale et ont permis d'étudier les orbitales moléculaires frontières, les descripteurs de réactivité chimique globale, le potentiel électrostatique moléculaire, l'analyse de la surface de Hirshfeld, le gradient de densité réduit (RDG), la fonction de localisation électronique (ELF) et le localisateur d'orbitales localisées (LOL). Le gap HOMO–LUMO de 3,53 eV confirme le caractère de transfert de charge intramoléculaire prononcé de FHP.

Les propriétés optiques non linéaires (ONL) ont été évaluées en phase gazeuse et dans le DMSO. La première hyperpolarisabilité statique calculée $\beta(0;0,0) = 42{,}51 \times 10^{-28}$ esu dépasse significativement la valeur de référence de la para-nitroaniline (PNA), confirmant FHP comme chromophore ONL de second ordre prometteur. La seconde hyperpolarisabilité γ passe de $111{,}85 \times 10^{-36}$ esu (phase gazeuse) à $425{,}51 \times 10^{-36}$ esu (DMSO), soulignant l'amplification de l'activité ONL de troisième ordre par l'effet du solvant polaire.

La caractérisation électrochimique par voltamétrie cyclique en acétonitrile a permis de déterminer les niveaux HOMO et LUMO expérimentaux à −5,44 eV et −3,86 eV, avec un gap électrochimique de 1,58 eV, en accord avec les prédictions DFT. L'évaluation du potentiel photovoltaïque de FHP comme accepteur d'électrons couplé à l'anthracène, la tétracène et le pentacène a donné des efficacités de conversion (PCE) atteignant 19,84 % (théorique) et 11,74 % (expérimental), avec des facteurs de remplissage de 89–94 %, confirmant le potentiel réel de FHP pour le photovoltaïque organique.

Mots-clés : *Base de Schiff ; hydrazone ; FHP ; diffraction des rayons X ; affinement multipolaire ; QTAIM ; DFT ; B3LYP ; transfert de charge intramoléculaire ; optique non linéaire ; hyperpolarisabilité ; voltamétrie cyclique ; photovoltaïque organique ; HOMO–LUMO.*

— العربية —

FHP دراسات بنيوية وكثافة إلكترونية وكيمياء حسابية وبصريات لاخطية وكهروكيميائية وكهروضوئية لمشتق قاعدة شيف الهيدرازونية

تُقدِّم هذه الأطروحة دراسةً متعددة التخصصات وشاملةً للمشتق الهيدرازوني لقاعدة شيف ذي الطابع الزويتيري، والمُعرَّف بالرمز (FHP)، واسمه:
(E)-3-(1-(2-(9H-fluoren-9-ylidene)hydrazineyl)ethylidene)-6-methyl-2H-pyran-2,4(3H)-dione
إذ تجمع الدراسة بين التقنيات التجريبية المتقدمة والأساليب الحسابية الحديثة، بهدف إرساء علاقة دقيقة ومنهجية بين البنية الجزيئية وخصائص هذه المادة العضوية المترافقة ذات المعمارية مانح–π–مستقبِل.(D–π–A)

جرى تخليق المركب (FHP) بتكثيف المركب 9H-fluoren-9-ylidene)hydrazine) مع حمض نازع أسيتيل الهيدرات، وتم توصيفه توصيفًا كاملًا بتقنية حيود الأشعة السينية على أحادي البلور، مما أكد أن المركب يتبلور في الزمرة الفضائية أحادية الميل($P2_1/c$) ، ويتخذ الصورة التوتومرية كيتو–هيدرازون الزويترية في الطور الصلب، مستقرةً برابطة هيدروجينية داخل جزيئية قوية من النوع–(N^+–H···O^-).واستُخدمت البيانات عالية الدقة لإجراء تكرير متعدد الأقطاب لكثافة الإلكترونات وفق صياغة هانسن–كوبنز باستخدام برنامج (MoPro).كما أسفر التحليل الطوبولوجي للكثافة الإلكترونية التجريبية وفق نظرية (QTAIM) عن توصيف فيزيائي دقيق لجميع الروابط التساهمية والتفاعلات غير التساهمية والتفاعلات بين الجزيئات في البلورة.

أعادت حسابات نظرية دالة الكثافة(DFT) ، عند مستوى((B3LYP/6-311G(d,p) ، استنساخ الهندسة التجريبية بدقة عالية، كما استُخدمت لدراسة المدارات الجزيئية الحدودية، ومعاملات التفاعل الكيميائي العام، والجهد الكهروستاتيكي الجزيئي، وتحليل سطح هيرشفيلد، ومؤشر تدرج الكثافة المختزل(RDG) ، ودالة التوطين الإلكتروني(ELF) ، ومحدد المدارات الموضعية .(LOL) وتؤكد فجوة الطاقة (HOMO–LUMO)البالغة (3.53 eV) الطابع الواضح لانتقال الشحنة الداخلي في المركب.(FHP)

قُيِّمت الخصائص البصرية اللاخطية (NLO) في الطور الغازي وفي مذيب (DMSO) عند المستوى نفسه من نظرية .(DFT) وقد تفوقت قيمة قابلية الاستقطاب الفائقة الأولى الساكنة المحسوبة $\beta(0;0,0) = 42.51 \times 10^{-28}$ (وحدة غاوسية) على القيمة المرجعية لمركب (PNA)بفارق ملحوظ، مما يرسخ المركب (FHP) مادةً بصرية لاخطية واعدة من الدرجة الثانية. كما ارتفعت قيمة قابلية الاستقطاب الفائقة الثانية (γ) من 111.85×10^{-36} وحدة غاوسية في الطور الغازي إلى 425.51×10^{-36} وحدة غاوسية في مذيب(DMSO) ، مما يبرز تعزيز النشاط البصري اللاخطي من الدرجة الثالثة بفعل المذيب القطبي.

كشف التوصيف الكهروكيميائي باستخدام تقنية القياس الفولطامتري الدوري في الأسيتونيتريل عن مستويي الطاقة التجريبيين (HOMO)و (LUMO)بقيمتي −5.44 eV و−3.86 eV على التوالي، مع فجوة كهروكيميائية مقدارها(1.58 eV) ، وذلك في توافق جيد مع تنبؤات نظرية .(DFT) كما أشار التقييم النظري للإمكانات الكهروضوئية للمركب(FHP) ، بوصفه مادة استقبال إلكترونات مقترنة بجهات مانحة مثل الأنثراسين والتيتراسين والبنتاسين، إلى قيم لكفاءة تحويل الطاقة (PCE) تصل إلى 19.84% نظريًا و11.74% تجريبيًا، مع معاملات ملء مرتفعة تراوحت بين 89% و94%، مما يؤكد الإمكانات الحقيقية للمركب (FHP) في تطبيقات الخلايا الشمسية العضوية.

الكلمات المفتاحية :قاعدة شيف؛ هيدرازون؛(FHP) ؛ حيود الأشعة السينية؛ تكرير متعدد الأقطاب؛(QTAIM) ؛(DFT) ؛(B3LYP) ؛ انتقال الشحنة الداخلي؛ البصريات اللاخطية؛ قابلية الاستقطاب الفائقة؛ القياس الفولطامتري الدوري؛ الخلايا الشمسية العضوية؛–(HOMO LUMO).

ISSN 0012-5016, Doklady Physical Chemistry, 2026, Vol. 521, No. 4, pp. 158–175. © Pleiades Publishing, Ltd., 2026.

COMPUTATIONAL CHEMISTRY AND MOLECULAR MODELING

Electrochemical and Theoretical Insights into Reactivity, NLO Behavior, and Photovoltaic Efficiency of a Hydrazone Molecule

Amina Lahouali Dit Yahyaoui[a,d,e], Merzouk Saidj[e], Salima Mosbah[b], Nour El Houda Belkafouf[e], Abdelkader Chouaih[e,*], Nouara Ziani[c], Amelle Djedouani[c], and Youcef Megrouss[a]

Received May 27, 2026; revised August 29, 2026; accepted August 29, 2026

Abstract—An experimental electrochemical study combined with computational methods was conducted to investigate the electronic properties and photovoltaic potential of (E)-3-(1-(2-(9*H*-fluoren-9-ylidene) hydrazinyl) ethylidene)-6-methyl-2*H*-pyran-2,4(3*H*)-dione (FHP), an organic compound of interest for optoelectronic applications. The study explored the electron density distribution using Hansen-Coppens multipolar model, atomic charges, and topological properties through reduced density gradient (RDG) analysis. The chemical reactivity descriptors, including frontier molecular orbitals (HOMO–LUMO gap), were calculated to understand the compound's stability and reactivity. Nonlinear optical parameters were evaluated using DFT/B3LYP/6-311G(d,p) level of theory with dimethyl sulfoxide (DMSO) as solvent, to assess its suitability for optoelectronic devices. Additionally, the electrochemical properties were analyzed, revealing key insights into the material's redox behavior. The findings indicate that the compound exhibits promising photovoltaic properties, with a balance between good electron donor-acceptor interactions and favorable optical characteristics. These results contribute to a deeper understanding of the structure-property relationships that govern the performance of organic materials in electronic and photonic applications.

Keywords: hydrazone molecule, non-covalent interactions, charge density, NLO parameters, optoelectronic behavior, organic solar cell

DOI: 10.1134/S0012501625600664

INTRODUCTION

Schiff bases constitute a prominent class of nitrogen-containing ligands formed through the condensation of primary amines with aldehydes or ketones. A Schiff base, also referred to as an imine or azomethine, is an organic compound featuring a (>C=N–) functional group [1]. These compounds play a vital role in the development of biologically active molecules, including antioxidant, antidepressant, antimalarial, anti-inflammatory, antiglycation, antimicrobial, antifungal, and antitumor activities [2]. The synthesis of Schiff bases is generally straightforward, cost-effective, and environmentally benign, often proceeding under mild conditions with high yields. The adoption of modern synthetic techniques, including microwave-assisted reactions, has further enhanced the efficiency and sustainability of Schiff base preparation, offering improved control over molecular architecture and tailored functional properties [3]. Their excellent thermal and chemical stability, particularly when complexed with transition metals, renders them ideal candidates for both academic and industrial applications. Beyond their chemical reactivity, Schiff bases exhibit notable optoelectronic and photophysical properties, driven by $\pi \rightarrow \pi^*$ transitions and intramolecular charge-transfer processes. These characteristics make them suitable for use in optical sensors, fluorescent probes, light-emitting materials, and nonlinear optical (NLO) applications [4]. Furthermore, integration of Schiff bases into nanostructured materials, such as graphene composites or porous films, has been shown to enhance their luminescent and electrochemical responses [5]. Thus, Schiff base derivatives are promising materials for NLO applications and dye-sensitized solar cells (DSSCs) due to their strong donor-acceptor structures and efficient charge trans-

[a] *Laboratory of Technology and Solid Properties (LTPS), Faculty of Sciences and Technology, Abdelhamid Ibn Badis University of Mostaganem, Mostaganem, 27000 Algeria*

[b] *Laboratoire de Chimie des Matériaux de Constantine, Faculté des Sciences Exactes, Université Frères Mentouri Constantine 1, Constantine, 25000 Algeria*

[c] *Département de chimie, faculté des sciences, université de Sétif 1, @City@, Algeria*

[d] *Superior School of Constantine, University City Ali Mendjeli, Constantine, 25000 Algeria*

[e] *Chemistry department, Faculty of Exact Sciences and Informatic, Hassiba Benbouali University, Chlef, 02000 Algeria*

**e-mail: aek_chouaih@yahoo.fr*

Next Materials 10 (2026) 101391

Contents lists available at ScienceDirect

Next Materials

journal homepage: www.sciencedirect.com/journal/next-materials

Research article

DFT-based investigation of structural, optoelectronic and molecular docking analysis of thiosemicarbazone derivatives

Amina Lahouali Dit Yahyaoui [a], Mohammed Hadj Mortada Belhachemi [a], Amine Ould Rabah [a], Khayra Hammou [a], Latifa Bensassi [a], Abdelkader Chouaih [a,*], Merzouk Saidj [a], Ömer Tamer [b], Davut Avcı [b], Yusuf Atalay [b]

[a] Laboratory of Technology and Solid Properties (LTPS), Faculty of Science and Technology, Abdelhamid Ibn Badis University of Mostaganem, Mostaganem 27000, Algeria
[b] Department of Physics, Faculty of Science, Sakarya University, Sakarya 54187, Türkiye

ARTICLE INFO

Keywords:
Thiosemicarbazones
DFT(B3LYP/HSEH1PBE)
ELF-LOL
Hyperpolarizability
Docking

ABSTRACT

A comprehensive theoretical investigation was carried out on two thiosemicarbazone Schiff base compounds: (*E*)-2-(2,4-dihydroxybenzylidene)thiosemicarbazone (Compound 1) and (*E*)-2-[(1H-indol-3-yl)methylene]thiosemicarbazone (Compound 2). Density Functional Theory (DFT) calculations were performed using B3LYP and HSEH1PBE hybrid functionals with the 6–311 + +G(d,p) basis set to explore their structural, electronic, vibrational, and nonlinear optical (NLO) properties. The HOMO-LUMO energy gaps were found to be 2.57 eV (Compound 1, HSEH1PBE) and 2.45 eV (Compound 2, B3LYP), indicating distinct reactivity profiles. Vibrational analysis reproduced experimental IR spectra, while UV-Vis studies revealed absorption maxima at 347 nm (Compound 1) and 331 nm (Compound 2), consistent with $\pi \rightarrow \pi^*$ and $n \rightarrow \pi^*$ transitions. The first-order hyperpolarizability (β_{tot}) values were calculated as 5.47×10^{-30} esu for Compound 1 and 6.12×10^{-30} esu for Compound 2, suggesting strong potential for optoelectronic applications. NMR calculations further validated the optimized geometries, with B3LYP showing lower RMSE values compared to HSEH1PBE. Molecular docking against HMGCS2 (PDB ID: 2WYA) revealed binding affinities of −6.7 kcal/mol for Compound 1 and −7.3 kcal/mol for Compound 2, stabilized by hydrogen bonding and hydrophobic interactions. PASS analysis confirmed promising pharmacological potential. These results highlight the dual applicability of the studied Schiff bases as candidates for both drug discovery and advanced NLO materials.

1. Introduction

Thiosemicarbazone derivatives have garnered significant interest due to their broad spectrum of pharmacological activities and versatile applications in both medicinal and coordination chemistry [1]. These compounds exhibit notable antibacterial, antifungal, antiviral, and anticancer properties, which are largely attributed to their ability to form stable metal ion chelates and engage in interactions with biological targets through hydrogen bonding and π–π stacking [2,3]. In particular, Schiff bases derived from thiosemicarbazones are of special relevance, as their extended conjugation not only enhances their chemical reactivity but also improves their optical properties [4]. Computational chemistry has become a powerful tool in the theoretical exploration of molecular systems. The advent of computational tools, particularly Density Functional Theory (DFT) and molecular docking, has significantly advanced the understanding of Schiff bases. These theoretical approaches provide valuable insights into structural, electronic, and reactivity-related properties that are often difficult to capture solely through experimental techniques. DFT, in particular, allows for accurate prediction of optimized molecular geometries, electronic charge distributions, frontier orbital energies, and global reactivity descriptors [5,6]. Such calculations complement experimental investigations by helping to rationalize spectroscopic findings and by guiding the design of new molecules with tailored physicochemical or biological properties.

* Corresponding author.
E-mail addresses: amina.lahouallidityahyaoui@etu.univ-mosta.dz (A.L.D. Yahyaoui), mohammedhadjmortada.belhachemi.etu@univ-mosta.dz (M.H.M. Belhachemi), amine.ouldrabah.etu@univ-mosta.dz (A.O. Rabah), khayra.hammou@etu.univ-mosta.dz (K. Hammou), latifa.bensassi@univ-relizane.dz (L. Bensassi), abdelkader.chouaih@univ-mosta.dz (A. Chouaih), merzouk.saidj@univ-mosta.dz (M. Saidj), omertamer@sakarya.edu.tr (Ö. Tamer), davci@sakarya.edu.tr (D. Avcı), yatalay@sakarya.edu.tr (Y. Atalay).

https://doi.org/10.1016/j.nxmate.2025.101391
Received 29 July 2025; Received in revised form 4 October 2025; Accepted 29 October 2025
Available online 4 November 2025
2949-8228/© 2025 The Author(s). Published by Elsevier Ltd. This is an open access article under the CC BY license (http://creativecommons.org/licenses/by/4.0/).